Texture Analysis of Diffraction Enhanced Synchrotron Images of Trabecular Bone at the Wrist

A Thesis Submitted to the
College of Graduate Studies and Research
in Partial Fulfillment of the Requirements
for the degree of Master of Science
in the Department of Computer Science
University of Saskatchewan
Saskatoon

By
K B M Abdullah Chisti

Permission to Use

In presenting this thesis in partial fulfilment of the requirements for a Postgraduate degree from the University of Saskatchewan, I agree that the Libraries of this University may make it freely available for inspection. I further agree that permission for copying of this thesis in any manner, in whole or in part, for scholarly purposes may be granted by the professor or professors who supervised my thesis work or, in their absence, by the Head of the Department or the Dean of the College in which my thesis work was done. It is understood that any copying or publication or use of this thesis or parts thereof for financial gain shall not be allowed without my written permission. It is also understood that due recognition shall be given to me and to the University of Saskatchewan in any scholarly use which may be made of any material in my thesis.

Requests for permission to copy or to make other use of material in this thesis in whole or part should be addressed to:

Head of the Department of Computer Science
176 Thorvaldson Building
110 Science Place
University of Saskatchewan
Saskatoon, Saskatchewan
Canada
S7N 5C9

Abstract

The purpose of this study is to determine the correlation between texture features of Diffraction Enhanced Imaging (DEI) images and trabecular properties of human wrist bone in the assessment of osteoporosis. Osteoporosis is a metabolic bone disorder that is characterized by reduced bone mass and a deterioration of bone structure which results in an increased fracture risk. Since the disease is preventable, diagnostic techniques are of major importance. Bone micro-architecture and Bone mineral density (BMD) are two main factors related to osteoporotic fractures. Trabecular properties like bone volume (BV), trabecular number (Tb.N), trabecular thickness (Tb.Th), bone surface (BS), and other properties of bone, characterizes the bone architecture. Currently, however, BMD is the only measurement carried out to assess osteoporosis. Researchers suggest that bone micro-architecture and texture analysis of bone images along with BMD can provide more accuracy in the assessment.

We have applied texture analysis on DEI images and extracted texture features. In our study, we used fractal analysis, gray level co-occurrence matrix (GLCM), texture feature coding method (TFCM), and local binary patterns (LBP) as texture analysis methods to extract texture features. 3D Micro-CT trabecular properties were extracted using SkyScanTM CTAN software. Then, we determined the correlation between texture features and trabecular properties. GLCM energy feature of DEI images explained more than 39% of variance in bone surface by volume ratio (BS/BV), 38% of variance in percent bone volume (BV/TV), and 37% of variance in trabecular number (Tb.N). TFCM homogeneity feature of DEI images explained more than 42% of variance in bone surface (BS) parameter. LBP operator - LBP 11 of DEI images explained more than 34% of variance in bone surface (BS) and 30% of variance in bone surface density (BS/TV). Fractal dimension parameter of DEI images explained more than 47% of variance in bone surface (BS) and 32% of variance in bone volume (BV). This study will facilitate in the quantification of osteoporosis beyond conventional BMD.

Acknowledgements

I am heartily grateful o my supervisors Dr. Mark Eramian and Dr. David Cooper. It is an honor for me to work on this research with their supervision and support. Besides, I learn from them the attitudes towards work as a good researcher and a great mentor, which will be a priceless treasure for the rest of my life.

I would like to express my sincere gratitude to Dr. David Cooper who provides the bone images in this thesis, without which this research would not have been possible.

Thanks to my friends for helping me during the work.

Thanks to my parents, for everything.

Contents

List of Tables

List of Figures

List of Abbreviations

GLCM	Gray Level Cooccurrance Matrix
TFCM	Texture Feature Coding Method
FD	Fractal Dimension
LBP	Local Binary Patterns
BV	Bone Volume
BS	Bone Surface
BS/BV	Bone Surface by Volume Ratio
BV/TV	Percent Bone Volume
Tb.N	Trabecular Number
LOF	List of Figures
LOT	List of Tables

Chapter 1

Introduction

The purpose of this study is to determine the correlation between texture parameters of DEI (Diffraction Enhanced Imaging) images and trabecular properties of human wrist bones (radii) as a potential tool for the assessment of osteoporosis. Osteoporosis is a bone disorder which is characterized by reduced bone mineral density. It is a state of a deterioration of bone micro architecture. Osteoporosis results in an potential fracture risk of the bone. Since early detection is possible, diagnostic techniques are of major importance. Trabecular bone micro architecture and bone mineral density (BMD) are two main factors related to osteoporotic fractures [56]. Currently, however, micro architecture is not evaluated in diagnostic scans. We have applied and tested texture analysis from DEI images. This study aims to determine how well texture parameters from the analysis of DEI images correlates with 3D trabecular properties. This study will ultimately help the detection, quantification and early prevention of osteoporosis beyond conventional BMD.

1.1 Introduction to Texture Analysis

Texture is an important component in image analysis. It is a source of visual information which refers to the arrangement of the texture elements within the image of an object [36]. Complex visual patterns of an object depict texture of the surface of the object. Thus, it can be regarded as a grouping of similarity components in an image [37]. The properties of the local pattern describe visual properties of the object such as regularity, fineness, uniformity, roughness, coarseness, smoothness, etc, of the texture. Two images of natural texture are shown in Figure 1.1. All surfaces have texture properties. Humans can easily distinguish objects based on the visualization of texture. For computers, texture is analyzed by distinguishing surface features of the object. In fact, humans use texture features as visual information in interpreting color photographs. Texture feature represents the spatial distribution of tonal variation. Numeric descriptions are produced in the process of texture analysis. These numeric descriptions are called texture features [5]. Feature extraction is the process of computing the texture features. Research in this area is extensive. Medical image analysis is one of the main applications of texture analysis. In general, the analysis involves the extraction of features from images which are then used for a variety of tasks, such as distinguishing normal tissue from abnormal tissue [56].

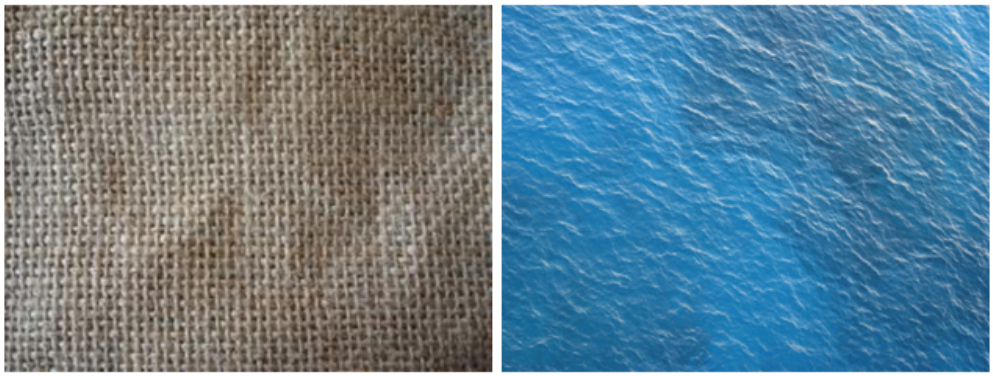

Figure 1.1: Examples of texture images [1]

1.2 Introduction to Bone Imaging

1.2.1 Osteoporosis

Osteoporosis, a systemic skeletal disease, is a disorder which is characterized by reduced bone mineral density and deterioration of bone micro architecture [56]. Osteoporosis results in an potential fracture risk of the bones particularly in proximal femur, spine, and wrist. In the year 2000 in Europe and USA there were 9 million osteoporotic fractures [47]. The mortality rates range from 20% to 24% in the first year after fracture. Greater risk of death may persist for at least 5 years afterwards [47]. The result of an estimation shows that the number of hip fractures could reach to 6.3 million by the year 2050 in the USA [47]. In osteoporosis treatment, the development of tools, which include in vivo study and quantification of bone quality and strength, is a major aim.

Bone mineral density (BMD, g/cm2) is identified as a strong determinant of bone strength [46]. Bone strength is routinely evaluated using BMD which is measured by dual-energy x-ray absorptiometry (DXA). Severity of osteoporosis is classified based on a measurement called the T-score [46].The T-score is an individual's bone density compared with what is normally expected in a healthy young adult of same sex. It's units are standard deviation from normal. Figure 1.2 depicts osteoporosis and its classification. If a BMD T-score is less than 2.5 standard deviations below 0, an individual is considered osteoporotic according to the standard of World Health Organization (WHO). Each SD decrease in BMD associates a 1.5 to 3.0 fold increase in osteoporotic fracture risk [46]. Many women with a BMD value greater than -2.5 SD suffer from osteoporotic fractures without being detected in BMD test [56]. Therefore, other fracture risk factors play a role beyond BMD. The amount and composition of bone tissue, bone geometry and bone micro architecture are the factors that are associated with bone strength.

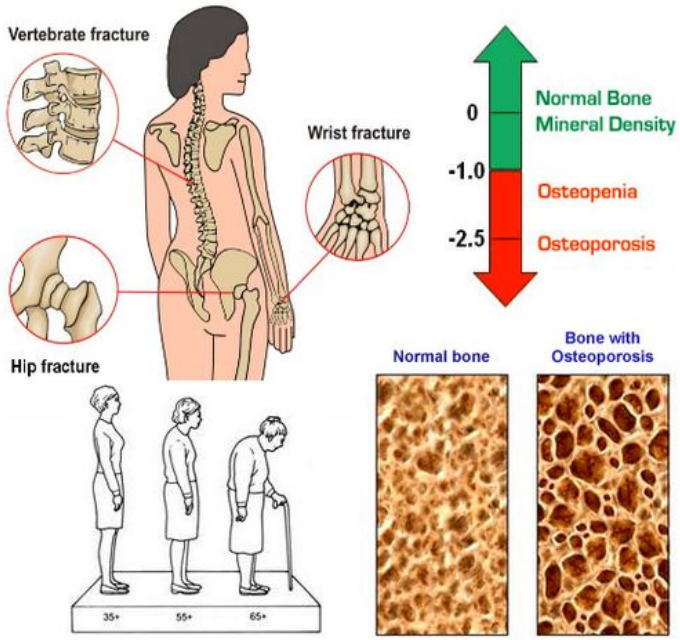

Figure 1.2: Osteoporosis and its classification[2]

1.2.2 Diffraction Enhanced Imaging

Diffraction Enhanced Imaging (DEI), a new x-ray radiography imaging technique, develops contrast through diffraction. DEI uses a synchrotron light source to create electromagnetic radiation. When electromagnetic radiation emitted as charged particles passes through electromagnets, it changes direction. This electromagnetic radiation is called synchrotron radiation. The particles travels around a circular orbit in large accelerators. These accelerators are called synchrotron. From the machine the radiation emits through metal windows, and delivered to experimental stations through large vacuum tubes. These tubes are called beam lines. The radiation are used to define very high intensity beams. The beam used in DEI technology is similar to standard x-ray. It is similar in the way that both beams are beams of radiation [11]. Dense tissue such as bone absorbs the radiation with standard x-ray and the radiation, which is passed through the tissue surrounding the bone, exposes the film. The object can be imaged either by transmitting the x-ray beam through it as in standard radiography, or after diffraction using the crystal analyzer. The deviation of a wave at the edge of an obstacle in its path is called diffraction. Unlike standard radiographs the radiation from DEI gets deflected by features instead of absorbed, and then it passes through crystal analyzer. The crystal analyzer acts as a scatter-rejector. By rocking (changing the angle) the analyzer detects angular variations of the x-ray beam from interactions within the target object. Figure 1.3 shows the equipment setup for DEI technology. Figure 1.4 shows rocking curve of the crystal in DEI. Different reflections: top, +0.5, +0.25, +0.125, -0.5, -0.25, and -0.125 indicate different positions.

As diffracted radiation instead of the absorbed radiation is used by the DEI, higher energy level radiation can be used to create its images. It is because of the use of higher energy radiation that passes through the

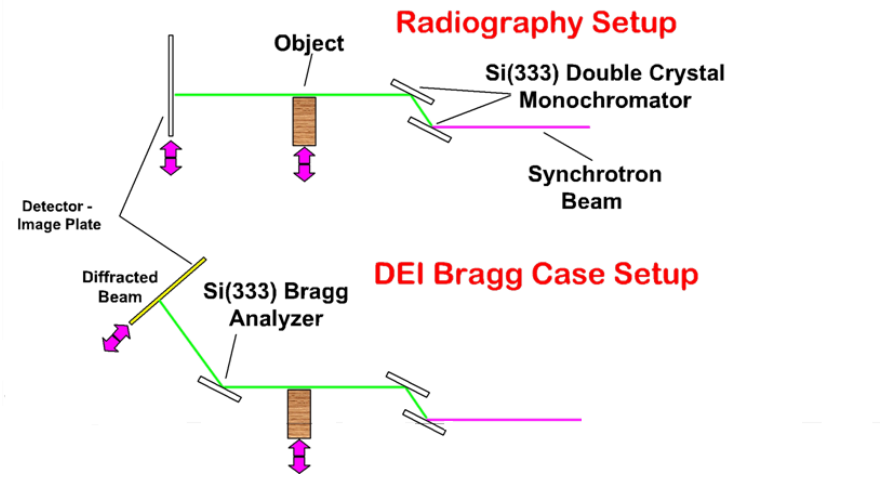

Figure 1.3: Schematic of Diffraction Enhanced Imaging (DEI) set-up redrawn from [59]

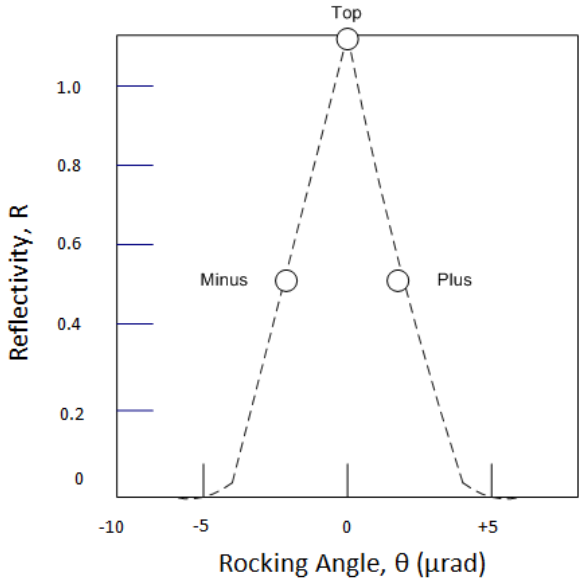

Figure 1.4: Rocking curve of Diffraction Enhanced Imaging (DEI).

Figure 1.5: Composite DEI image of cadaveric wrist. [59]

tissue that it can use a lower overall dose compared to traditional radiographs [78]. The diffraction used in DEI creates a higher quality image as well. Figure 1.5 shows DEI image of a cadaveric wrist from opposite sides of the rocking curve displaying many more details compared to standard radiographs. It is even possible to differentiate soft tissue [59]. Using DEI, we can find the difference between bone, skin, and ligaments [59]. This provides another advantage of DEI over traditional radiographs - with DEI being able to show the differences between many types of tissue while there is no need for contrast media [11].

Beside the advantages of using DEI technology, there are some disadvantages. Most synchrotron light sources are extremely large [78]. Synchrotrons can take up the space of entire buildings. This space is required to be able to bend the particles correctly. DEI imaging is currently impractical for widespread use because of the size of synchrotrons. Besides DEI there are many common imaging modalities which have been able to improve the quality of their images. The advancement of CT and MRI in recent years has proved that these techniques have the ability to produce good contrast images like DEI [11].

1.3 Motivation and Objectives

DXA, the standard for clinical bone assessment, provides only measurement of density and the amount of bone mineral but no micro architectural information. So, there is a need for the development of new efficient methods for the visualization and quantification of bone architecture. Therefore, we propose the exploration of diffraction enhanced imaging (DEI). DEI can be an improved means of assessing trabecular bone architecture with reduced radiation dose. As DEI is able to obtain more information about the object than conventional x-ray absorption imaging, we will be able to obtain more texture information to support our following hypothesis.

We hypothesize that 3D micro-CT trabecular architecture within a bone is reflected by the bone micro architectural information captured within 2D DEI images. Our objective is to test this hypothesis through a study. We will carry out the study focused upon a common fracture site - the wrist. Our hypothesis aims to address that 2D DEI may provide trabecular micro architectural information which is comparable to micro-CT 3D tomographic approaches. The potential of this approach is significant in the assessment of

osteoporosis.

In this thesis, texture analysis methods are used to observe correlations between texture parameters and trabecular properties within the bone [49]. We used texture feature coding method (TFCM), local binary patterns (LBP), fractal dimension (FD), and gray level cooccurrance matrix (GLCM) to capture texture parameters of DEI bone images. This study will inform and facilitate a subsequent study using a larger dataset of images of human distal forearm bone and help to explore more challenging areas of DEI technology.

Chapter 2

Literature Review and Background

2.1 Texture analysis approaches

Texture analysis is a powerful tool in a large range of applications such as object detection and pattern recognition [16]. There are different techniques developed to characterize texture by using mathematical procedures. Two major approaches can be used to categorize the texture: statistical and structural approaches. Statistical texture approaches are the common texture approaches that defines textures based on describing spatial distribution of gray values or pixel values. They can be measured from the first-order and second-order statistics. Detailed analysis of different techniques are given below. Structural approaches are of limited use for this application and thus are not discussed in detail.

2.1.1 Statistical texture description methods

First-order statistics

This is the simplest method which uses a histogram that represents the distribution of all pixels intensities in a given region of interest. It can not describe the texture of a region properly based on the number of bins and the number of pixels in that region of interest. So, a new method has been developed to improve the texture descriptor. Statistical moments of histogram is a widely used approach which is based on the histogram of the intensities. It is defined as following:

$$\mu_n = \sum_{i=0}^{L-1} (z_i - m)^n \, p\,(zi) \tag{2.1}$$

where z_i is the intensity, L is the number of intensity levels of the region of interest, and $p(z_i)$ is the histogram of the intensity levels. We can extract different descriptors using this method. Mean measures the average of the intensities of the texture and variance defines the average contrast of the texture. Although this method is simple and provides several descriptors, it cannot provide a comprehensive description of textural region because the texture features are statistics calculated from the original image values and do not consider pixel relationships. Therefore, it does not give a comprehensive description of the texture region.

Gray Level Co-occurrence Matrix descriptors

Gray level co-occurrence matrix (GLCM) is an example of a second-order statistical method. It is widely used in texture analysis [57]. A co-occurrence matrix is generated using the gray-level histogram of the image. The dimension of the matrix is $L_g \times L_g$, where L_g is the number of possible intensity levels of the image. Pairs of points separated by a distance and angle with pairs of gray levels generate values that are used to generate the probability density matrix. The probability density matrix is the final outcome of GLCM. Second-order features, which consider pixel relationships, are generated from the gray scale histogram of absolute gray values. Therefore, it gives a comprehensive description of the texture region. More details about GLCM descriptors will be discussed in the next chapter.

Texture Feature Coding Method descriptors

In TFCM, a feature image is generated from a gray level image. The feature image is represented by a texture feature number (TFN). A 3×3 texture unit in an image is used to generate the TFN. The texture unit considers the gray-level variations of its eight surrounding pixels. The ideas of gray-level histogram and co-occurrence matrix are used in TFCM. A TFN histogram and a TFN co-occurrence matrix (CM) is generated from the TFN obtained previously. TFCM also uses the maximum entropy criterion that is used to find optimal gray-level variation tolerance [39]. TFN co-occurrence matrix (CM) produces texture features. TFCM derives seven texture feature descriptors. More details about TFCM descriptors will be discussed in the next chapter.

Local Binary Patterns

Ojala et al. [63] introduced the LBP operator, which was based on a 3×3 local neighborhood with a 45° quantization of the angular space provided by the eight neighborhood (interpolation) points. The neighborhood represents the local texture around a central pixel. The value of each pixel of this neighborhood is thresholded using the value of the central pixel [63]. Later in [64], Ojala et al. proposed to use the LBP histogram for rotation invariant texture classification. The study showed impressive classification results on the Brodatz texture database. In other application like face recognition, LBP has also been used [4]. Zhang et al. [34] defined a new operator called local derivative pattern (LDP). LDP is a higher-order directional operator based on LBP which provides more detailed information. More details about LBP will be discussed in the next chapter.

Model-based descriptors

A model of each pixel is generated based on a weighted average of the pixel intensities in the model-based description method. Then the texture parameters are described from the image models. Fractal model is an important model-based descriptor. The analysis of the fractal model is called fractal analysis which describes

fractal dimension and lacunarity in a given region of interest. Fractal analysis is described later in detail.

Methods based on Fourier analysis or fractional Brownian motion require gray-level images [17]. The texture of images obtained by radiography shows the properties of fractals [44]. Some fractal parameters can be evaluated on histological sections, CT images, and MRI scans [27]. More details about fractal dimension will be discussed in the next chapter.

Markov random field based model is another popular model-based descriptor. In this model, descriptors are defined for images as a probabilistic process that provides the probability of the pixel determined by the gray-levels distribution of its neighbouring pixels. The number of entries $G-1$ where G is the number of gray-levels and parameter $\theta(T)$ define the probability, $p(X = k|neighbours)$, which is a binomial. θ is defined as follows:

$$\theta = \frac{exp\,(T)}{1 + exp\,(T)} \tag{2.2}$$

where the parameter T of θ is defined for different orders of the models.

Scale Invariant Feature Transform (SIFT) based descriptors

Scale invariant feature transform (SIFT) was introduced by Lowe [53] in 2004. It combines a scale invariant region detector and a description based on the gradient distribution in the region. The descriptor is defined from a 3D histogram of gradient locations and orientations. The gradient magnitude weights the location and orientation of bins. SIFT has four stages: extrema detection, localization of keypoint, assignment of orientation and the description of keypoint.

$$D(x, y, \sigma) = (G(x, y, k\sigma) - G(x, y, \sigma)) * I(x, y) \tag{2.3}$$

The first stage identifies potential interest points, which are invariant to scale and orientation using difference of gaussian (DOG) function. The edge response is eliminated and low contrast points are rejected in the keypoint localization step. The gradient orientations of sample points within the region forms an orientation histogram to get an orientation assignment. In the experiment of Lowe [53], the best results were obtained with a 4×4 array of histograms with 8 orientation bins each. The SIFT descriptor was used in image matching and indexing in Scovanner et al. [72].

Laws' texture energy measures

Laws texture method is an example of a classical texture description. In the study of Laws [45], he demonstrated that density, uniformity, regularity, roughness, and linearity play important role in describing texture of an given region. This method describes texture properties by using average tray-level, edges, spots, ripples and waves. These parameters are described using three simple vectors: $L_3 = (1, 2, 1)$, $E_3 = (-1, 0, 1)$,

and $S_3 = (-1, 2, -1)$. $L_3 = (1, 2, 1)$ calculates the average gray-levels, $E_3 = (-1, 0, 1)$ measures first difference (edges), and $S_3 = (-1, 2, -1)$ calculates the second difference (spots). Five vectors are produced after convolution of these vector with themselves:

$$\begin{array}{cc} Level & L_5 = [1, 4, 6, 4, 1] \\ Edge & E_5 = [-1, -2, 0, 2, 1] \\ Spots & L_5 = [-1, 0, 2, 0, -1] \\ Ripples & L_5 = [1, -4, 6, -4, 1] \\ Waves & L_5 = [-1, 2, 0, -2, -1] \end{array} \tag{2.4}$$

A major problem using Laws texture method is that the window size of the Laws mask must be equal to the resolution and the scale of the original image. This leads to more cost of time and an increase in computational complexity.

Spin image based descriptor

Johnson and Hebert [43] first introduced the spin image, which is an expressive representation for 3D object recognition in the context of range data. Spin image is represented as a histogram of the relative positions in the neighborhood for a given image point. Recently, spin image descriptor has been adapted to 2D images [43]. The two dimensional histogram represents the distribution of brightness values in an affine-normalized patch. Spin image represents the relationship between the distance and intensities of pixels to the central pixel in a local image patch. The distance from the center of the local patch, d and intensity, i, are the two dimensions of the spin image histogram. A pixel having distance (d) and intensity (i) contributes to the bin indexed by (d_0, i_0). This contribution is proportional to $exp(-(d-d_0)^2/(2\alpha^2) - (i-i_0)/(2\beta)^2)$, where α and β are soft width parameters. The main advantage of spin image is that it can provide richer representation of local appearance than that of one dimensional descriptor. One disadvantage is that the dimension of the descriptor which is used to build the histogram is the product of the number of quantization levels of distance and the number of quantization levels of intensities.

Edge detection based descriptor

Edge detection is used in texture description and feature detection. In a fixed region the number of edge pixels provides some indication of the direction of these edges and the nature of that region. The number of edge pixels is defined as the bi-product of the edge detection process and these edge pixels can provide good indication about the pattern of the texture of a region. The gradient magnitude $M(p)$ and gradient direction $D(p)$ for each pixel p are produced when a gradient-based edge detector is applied to a given region of N pixels. We can then define a texture feature named edginess per unit area for some threshold (T). The equation for edgeness is given below:

$$F_{edgeness} = \frac{p|M(p) \geq T}{N} \tag{2.5}$$

This texture can be extended to measure the busyness and orientation by applying histograms for both gradient magnitude and direction. We can define it as follows:

$$F_{md} = (H_m(R), H_d(R)) \tag{2.6}$$

where $H_m(R)$ is the normalized histogram of gradient magnitudes and $H_d(R)$ is the normalized histogram of gradient directions. These histograms are over a small number of bins. We can also define the density, direction of edge, and the edge frequency to measure the coarseness of the texture. It can be defined as follows:

$$g(d) = |f(i,j) - f(i+d,j)| + |f(i,j) - f(i-d,j)| + |f(i,j) - f(i,j+d)| + |f(i,j) - f(i,j-d)| \tag{2.7}$$

where $g(d)$ is the distance-dependent texture description function and f is the sub image in a neighbourhood N for variable distance d. This texture is measured as average values of gradient in specified distances d. This function is similar to the autocorrelation function, in which the maximum corresponds to the minimum of the autocorrelation and the minimum corresponds to the maximum of the autocorrelation. First-order and second-order statistics of edge distributions can be used to extract some other textures features. These features are described in Tomita and Tsuju [77]. For example, the entropy of the edge magnitude histogram characterizes the randomness of the texture. Edge density represents the coarseness. The finer the texture is, the higher the number of edge pixels present in the texture edge image. They also define the texture periodicity.

This method of texture description can describe homogenous textural region. One of the advantage is that there is no need to assume any prior knowledge about the image. There is also a disadvantage. The edge-detection based descriptor is defined after an edge detection algorithm is applied. If the edge detection algorithm does not provide an accurate result, then the texture descriptors are not going to be accurate either. Therefore, noise may interrupt the result of the edge detection.

Methods based on spatial frequencies

Methods based on spatial frequencies need to assume some prior knowledge that the texture character has direct relation with the spatial frequencies of texture primitives. This prior knowledge includes higher frequencies which represent fine texture and lower frequencies which represent coarse texture. These methods are used in three different approaches: autocorrelation function and Fourier transform. These approaches are described below.

Autocorrelation function is used in this method which is based on spatial frequencies. A single pixel is considered as texture primitive and its gray level is considered as the primitive tone property. One method is to

evaluate the autocorrelation function of a texture. If the texture elements are small, then the autocorrelation function decreases rapidly, while when the texture elements are large, then the autocorrelation function decreases slowly.

$$C_{ff}(p,q) = \frac{MN}{(M-p)(N-q)} \frac{\sum_{i=1}^{M-p} \sum_{j=1}^{N-q} f(i+p, j+q) f(i,j)}{\sum_{i=1}^{M} \sum_{j=1} N f^2(i,j)} \tag{2.8}$$

where (p,q) is the position difference in the (i,j) direction, and (M,N) are the image dimensions.

Fourier transform is also used in method based on spatial frequencies. Average values of frequencies within a ring of Fourier spectrum are used to describe texture features. These features reflect coarseness when energy is high in large radius rings and fineness when energy is high in small radius rings of Fourier spectrum. One main disadvantage of Fourier coefficients is that it can not be adopted in a local approach because Fourier coefficients depend on the entire image and the relationship between pixels are not explicit. Therefore, it becomes inconvenient to understand the the Fourier spectrum as most of the spatial information is lost during the transformation process.

Gabor transform is used to overcome these problems. A group of wavelets are called Gabor filters where each wavelet captures energy at a specific frequency and a specific direction. At each point of an image with different orientations and different scales, Gabor filters are applied, then the energy content at that pixel is obtained using the following equation:

$$E(m,n) = \sum_x \sum_y |G_{m,n}(x,y)| \tag{2.9}$$

where $m = 0, 1, ..., M-1$ represents scale of the wavelet and $n = 0, 1, ..., N-1$ represents orientation of the wavelet. The mean and standard deviation of the magnitude of the transformed coefficients are used to represent the homogeneity of the texture region. Gabor transform is useful in describing texture features in a local approach because of its rotation, scale and translation invariance. There is another method based on spatial frequencies, Angle Measure Technique (AMT), that uses similar theory of Fast Fourier Transform (FFT) and Gabor transform.

2.1.2 Structural texture description methods

Different structural descriptors were proposed in Carlucci et al. [15]. The authors used different shapes of structural elements to define texture features. Structural descriptors are limited in practice because only regular textures are described by them. These textures are the composition of well-defined texture elements which are regularly spaced parallel lines, while real textures are conceived as distorted versions of normal textures. We will not describe more about structural methods because of their limited use in texture analysis.

2.1.3 Discussion

We have discussed various texture analysis methods. We have also described their advantages and disadvantages. Gray-level co-occurrence matrix descriptors and fractal analysis descriptors are widely used methods in texture analysis as in the next section we will discuss some of the studies in which these methods were used with good efficiency and accuracy. That is why we selected gray-level co-occurrence matrix descriptors and fractal analysis descriptors to apply in our bone images to extract texture features. We have also used texture feature coding method and local binary patterns. We will discuss later in this Chapter about why we selected texture feature coding method and local binary patterns in our study.

2.2 Bone Imaging

Bone can be described in four different approaches: bone quantity, bone material, bone structure, and bone turnover. Bone mineral density, bone mineral content, areal bone mineral density and ash weight are the measurements done in bone quantity assessment. Bone structure measures micro-structure, macro-structure, and also nano-structure. Quality of the bone material and mechanical testing are the measurements which fall in the bone material approach. Using different imaging techniques we can derive the condition of bone structure. DXA, high resolution-CT, micro-MRI, micro-CT and even nano-CT are examples of imaging techniques. But, in clinical practice, DXA has been the standard for the assessment of osteoporosis.

Majumdar et al. [52] reviewed imaging techniques and texture analysis techniques employed in the diagnosis of osteoporosis in 1999. They used images captured using different imaging techniques which included conventional radiography, high-resolution CT (HRCT), and high-resolution MR imaging (HRMRI) [52]. They used fractal dimension using box counting method and co-occurrence matrices to extract texture features. Their result showed that the best result was found using HR-CT images. Their study demonstrated that texture features and bone mineral density predict bone strength and osteoporotic fractures. They advocated more research work in finding the relationship among texture parameters, BMD and trabecular parameters for predicting fracture risk and for the early prevention of osteoporosis.

Advance imaging techniques beyond DXA have many limitations such as longer time to scan samples, radiation dose, high cost of equipment, and their availability. These limitations make these modalities less suitable for clinical practice. Most of these techniques can be therefore used as research purpose only. The use of synchrotron-based imaging technologies in medical image processing has become popular. Cooper et al. [24] in 2011 explored the way of visualizing the bone internal structure of the human distal radius using DEI. They studied 20 human radii which were first radiographed by a Philips Medio (Philips Healthcare, MA). Out of 20 samples, 10 samples with higher reflection of apparent trabecular morphologies were selected for DEI imaging at CLS synchrotron at 41 keV. These imaging results showed that DEI images demonstrated enhanced visualization of trabecular architecture. In the DEI images the growth plate in the bones was located with good evidence. They also showed that in radiographs the porosity was not visible whereas

in DEI longitudinally oriented osteonal canals were evident. They confirmed the potentiality of using DEI in projection images to improve the visualization of trabecular architecture. They suggested that texture analysis of bone images would reveal good relationship with trabecular architecture because DEI images proved to have more trabecular architecture details than radiographs.

Micro-CT imaging studies have been conducted on humans and rats as a popular tool for clinical diagnosis of osteoporosis. Extensive researches have been done to understand and monitor the bone architectural changes or trabecular changes in the bone tissues in humans and animals by analyzing image attributes. Trabecular properties like bone volume/total volume (BV/TV) (percent), bone surface/total volume (BS/TV) ($\mu m^2/\mu m^3$), trabecular thickness (Tb.Th) (μm), trabecular separation (Tb.Sp) (μm), and trabecular number (Tb.N) (number/μm) characterizes the bone architecture. These trabecular properties are explained in detail in the next Chapter. The researches on bone image analysis belong to this category.

2.3 Motivation for assessing bone structure

We need to assess the bone structure in order to improve the overall knowledge of bone and to improve clinical decisions (ex: osteoporosis, orthopaedic surgery, and also in dental field). Several studies showed [62, 69] that bone quantity is strongly connected to bone strength. Johnell O et al. [62] examined the relationship between BMD and fracture risk using 39,000 samples. They showed that low hip BMD was an important predictor of fracture risk which is also dependent on age and BMD z score. However, extensive evidence in the literature suggests that bone mechanical strength is not solely dependent on its mineral density (BMD) [38].

Hordon et al. [38] investigated how well the differences in trabecular properties may predict the fracture risk independent of bone mass. Fracture (22 women and 11 men) and non-fracture (31 women and 16 men) groups in vertebral fracture where matched by age, gender, and BMD were collected. Their result showed that there is no significant difference in either gender between fracture and non-fracture groups in BV/TV, Tb.Th, Tb.N, and Tb.Sp. The lumber BMD was measured using Hologic 2000 densitometer. BMD measurements were similar in women with or without fracture and also for men with or without fracture.

Compston et al. [22] reported that bone quantity may not be sufficient to determine bone strength. 28 women and 17 men of fracture and 19 women and 14 men of non-fracture groups in femur fracture were investigated. Those subjects were also categorized into osteopenic and osteoporotic subjects. It was reported that no significant difference were found between fracture and non-fracture groups when BMD was counted. It could not strongly differentiate between osteopenic and osteoporotic subjects. Thus it was stated that bone micro architecture investigation may be needed to determine the bone strength.

On the basis of these findings, they concluded that trabecular properties were not significantly different between fracture and non-fracture subjects when BMD is counted. It has been shown that bone quantity measurement is not sufficient to predict fracture risk [38, 58]. Therefore, there is a need to apply other

methods to analyze the trabecular bone microstructure. Texture analysis methods may come in very handy for this purpose. We will now discuss some studies that described how BMD is correlated with texture features. These studies provided the justification to use these texture methods in the bone architecture analysis independent of BMD.

BMD is significantly correlated with texture features [57]. According to Materka et al. [57], based on statistical analysis of the linear correlation coefficient, one can state that there is a significant correlation between the bone mineral density measured by DXA and texture features extracted from standard radiographs. Although this study focused on the relationship between BMD and texture features, this study suggested that GLCM features can be of great potentiality in the study of bone imaging. In their study, a number of histogram-derived ROI features like image mean, standard deviation, GLCM features like skewness, kurtosis, energy, entropy, and fractal dimension in vertical dimension were investigated. Based on the BMD results, a group of 50 subjects was divided into 3 categories: normal 19 subjects, osteopenia (condition of physiological loss of calcium) 21 subjects, and of abnormal loss of calcium (osteoporosis) 10 subjects. Their study demonstrated a relationship between the BMD and grayscale image mean and standard deviation. Apart from kurtosis and fractal dimension in horizontal direction, all other features showed a significant correlation. They also suggested that selecting optimum texture features from a variety of known approaches can provide stronger relationship. We will later discuss some studies that showed there are association of texture features with 3D bone micro architecture parameters. Similarly, Lin et al. [51] examined the correlation between texture features and biomechanical properties in conjunction with BMD in order to predict bone strength using radiographs of fifty-one human cadaveric femur bones. Quantitative computed tomography (QCT) was used to calculate BMD values. Conventional radiography was performed to image the bones using a clinical X-ray unit (BT-S4, Philips, Netherlands). Fractal dimension was calculated. The biomechanical properties, maximum compressive strength (MCS) and maximum shear stress, were determined with an electromechanical material testing machine (MTM, Germany). Fractal dimension was significantly correlated with MCS and MSS (r^2=0.35, r^2=0.34). MCS and MSS were significantly correlated with BMD (r^2=0.34, r^2=0.50).

Bone fragility results in minimal trauma fractures in bone diseases [22, 62, 68]. Clinical features are pain, fissures, and fractures, which may occur after minimal trauma [38]. Seeman et al. [73] in 2006 reviewed a study in which instead of considering bone fragility as being the result of having low bone mass, they recognized that the bone structure and bone material result in bone fragility. The study of Ito et al. [54] also showed that bone structure plays a key role in determining bone strength. Therefore, in our study we investigated the relationship between trabecular bone properties and bone texture features independent of the bone mineral density.

2.4 Trabecular bone texture analysis

Trabecular bone analysis has many preclinical applications such as micro-architecture evaluation, osteoporosis management, and bio-mechanical properties determination. We will mainly focus on the studies on micro architecture evaluation. Texture analysis of bone radiographs has been applied in determining the relationship with BMD and 3D bone morphometric parameters. Among the texture analysis methods gray-level co-occurrence matrix and fractal analysis have been widely used. We will now discuss some of the studies in which texture analysis of 2D images were investigated to find any relationship with bone micro architecture.

2.4.1 Micro-architecture evaluation: Conventional X-ray

Texture analysis can be a good technique to predict the bone strength [38]. In order to examine the correlation between texture parameters of human femur radiographs and biomechanical strength, Huber et al. [41] studied 14 cadaveric femurs. These samples were radiographed using Siemens Mobilett XP Eco machine. BMD was calculated using QCT. Five ROIs (cancellous region of the head, upper and lower neck, trochantric, and shaft region of the proximal femur) were selected for texture analysis. GLCM and Minkowski fractal dimension were applied on these ROIs. 3D micro-CT was used to obtain bone parameters. Biomechanical strength (torque of breakaway) was assessed by rotating the probe around its longitudinal axis using a calibrated digital torque meter (HD-100, HIOS, Inc, Japan). Bone parameters were highly correlated with texture parameters up to $r^2 = 0.61$(Minkowski FD, GLCM).

In 2005, Chappard et al. [20] investigated the relationship between 2D image texture parameters and 3D bone parameters. They examined 21 human cadaveric tibia. Radiographs were collected using a Faxitron X-ray system. A ROI of 512×512 pixels was trimmed from the centre of the tibia bone image. They extracted fractal dimension and gray level co-occurrence matrix parameters from the images. They used micro-CT $SkyScan^{TM}$ 1072 software to obtain bone parameters. Their results were significant (Tb.Sp/GLN: $r^2 = 0.60$, Tb.N/FD: $r^2 = 0.61$).

Lespessailles et al. [48] in 2006 assessed the texture parameters of radiographs in complement to bone mineral density to improve the prediction of osteoporotic fractures. Thirty human cadavers were used. Images were obtained on human os calcis using a new high-resolution digital X-ray device (BMA^{TM}, D3A Medical Systems). Two texture methods (co-occurrence matrix and fractal analysis) were used on the images. BMD was measured using DXA technique. Fractal parameter was computed from images using fractal analysis. 3D bone parameters were obtained using micro-CT. There was moderate relationship between co-occurrence matrix features and Tb.Sp ($r^2 = 0.39, p < 0.01$). They found a significant relationship between BMD and fractal parameter ($r^2 = 0.43, p < 0.03$).

In 2009 Steines et al. [76] studied radiographic images taken from cadaver femur bones. Radiographs of bone were collected using professional desktop scanner (Umax PowerLook 1100). Then they used fractal analysis on these images. 3D trabecular properties (BV/TV, Tb.N, Tb.Th, and Tb.Sp) were obtained using

micro-CT technique. Significant relationships were found between fractal and bone parameters (FD/Tb.N: $r^2 = 0.40, p < 0.01$, FD/ BV/TV: $r^2 = 0.24, p < 0.01$, FD/Tb.Sp: $r^2 = 0.42, p < 0.01$). No significant relationship was observed between fractal dimension and Tb.Th.

Fouque-Aubert et al. [32] in 2012 conducted a research to assess changes in trabecular bone architecture using bone texture analysis from radiographic images of human hand. In this study, they evaluated the trabecular bone texture of metacarpal heads of rheumatoid arthritis (RA) patients (total 78 patients: 19 early RA and 59 late RA) in comparison with healthy controls (50 subjects). They selected the heads of the second metacarpal (MCP2) and third metacarpal (MCP3) of the right hand using high resolution X-ray device (BMA^{TM}, D3A Medical Systems, France) for radiography. A region of interest of 100×100 was selected with a pixel size $50\mu m$. They used GLCM and fractal parameter to determine the relationship between clinical features of the groups. 3D bone parameters were obtained using HR-pQCT. Their result showed significant correlations of fractal parameter with BV/TV ($r^2 = 0.60$) and Tb.Th ($r^2 = 0.54$) at the MCP2 and also significant correlations were found between fractal parameter and BV/TV ($r^2 = 0.56$) and Tb.Th ($r^2 = 0.51$) at the MCP3.

In the study of Ranjanmennahary et al. [68], 16 cadaveric human femur bones were examined. Radiographic images were obtained with a X-ray device using a digital sensor C-MOS. Two ROIs were positioned on the radiographs located close to great trochanter and femoral head. Bone parameters were obtained using 3D micro-CT $SkyScan^{TM}$ 1072 software. BV/TV, BS/BV, Tb.Th, Tb.N, and Tb.Sp measurements were collected. GLCM was used to extract features like energy, correlation, entropy, and homogeneity. Their results showed that there were significant correlations between parameters (Energy/ BV/TV: $r^2 = 0.59$, Correlation/ BV/TV: $r^2 = 0.35$) for femoral head and (Energy/ BV/TV: $r^2 = 0.54$, Correlation/ BV/TV: $r^2 = 0.25$) for great trochanter.

Pulkkinen et al. [67] evaluated the relationship between texture parameters and bone parameters of human femur bones. Their sample consisted of 62 human femurs. These femur bones were radiographed using a Faxitron X-ray system at 40 to 85 kV. They chose three ROIs: femoral head, femoral neck, and greater trochanter. GLCM and fractal analysis were applied on the ROI images. Homogeneity at the femoral neck area showed moderate relationship with the Tb.Sp ($r^2 = 0.38, p < 0.01$). A significant relationship was also observed between Homogeneity at the trochanter area and the Tb.N ($r^2 = 0.81, p < 0.01$). Fractal parameter at the femoral head and femoral neck showed significant relationships with the Tb.Sp ($r^2 = 0.59$ and $r^2 = 0.63, p < 0.01$) respectively. GLCM features showed moderate relationship with bone parameters.

Similarly, Corroller et al. [25] studied radiographs of proximal end of 21 excised human femur bones using high-resolution digital X-ray device (BMA^{TM}, D3A Medical Systems) to estimate two texture features: GLCM and fractal parameter. They measured BMD values using DXA and 3D bone parameters using micro-CT. Three ROIs of 128×128 were selected in the femoral neck, intertrochantric region, and greater trochanter. Correlation coefficients in the same ROI between fractal parameter and bone surface (BS) were significant ($r^2 = 0.53, p < 0.01$ in the femoral neck, $r^2 = 0.51, p < 0.01$ in the intertrochantric region, and

$r^2 = 0.35, p < 0.01$ in the greater trochanter). Correlation coefficients in the same ROI between bone surface (BS) and GLCM features were significant ($r^2 = 0.33, p < 0.01$ in the femoral neck, $r^2 = 0.62, p < 0.01$ in the intertrochantric region, and $r^2 = 0.37, p < 0.01$ in the greater trochanter).

The study of Elvira et al. [70] used texture analysis methods such as second-order GLCM, Minkowski fractal dimension (MD), and the scaling index method for the prediction of osteoporotic fracture risk. In that study, texture analysis, BMD, and bone measurements were performed on proximal femur. Radiograph images were obtained for 2D texture analysis. Their results showed that for different ROIs in proximal femur: trochanter, intertrochanter, upper neck, and lower neck, different combinations of features showed significant correlation with bone parameters. They also suggested that there is an importance of selecting texture features along with BMD results.

Accordingly, Lespessailles et al. [49] showed that there are significant relationships between fractal parameters and 3D bone parameters. They used 19 human femur bones. Kodak Min R screen film system was used to obtain radiographs. A 265×256 ROI was selected from femoral neck and micro-CT was used to collect bone parameters. The results of their study showed mild correlations between fractal dimension and bone parameters (FD/ BV/TV: $r^2 = 0.20, p < 0.05$, FD/Tb.Th: $r^2 = 0.20, p < 0.05$, FD/Tb.Th: $r^2 = 0.19, p < 0.05$).

In the study of Chappard et al. [19] , 40 excised human femur bones were obtained. DXA was used to measure BMD. Radiographs were obtained using Prestilix 1600X unit (GE Medical Systems, Fairfield). Four ROIs (femoral head, greater trochanter, intertrochantric region, and femoral neck) of 340×340 were selected. They used GLCM to extract texture features. They selected homogeneity and entropy features among other features to correlate with bone properties. Significant correlation were found between entropy and BV/TV ($r^2 = 0.37, p < 0.01$ in the femoral neck, $r^2 = 0.37, p < 0.01$ in the intertrochantric region, and $r^2 = 0.38, p < 0.01$ in the femoral head). Significant correlation were also found between homogeneity and BV/TV ($r^2 = 0.38, p < 0.01$ in the femoral neck, $r^2 = 0.38, p < 0.01$ in the intertrochantric region, and $r^2 = 0.62, p < 0.01$ in the greater trochanter).

In an *in vivo* study, Bacchetta et al. [8] examined the texture parameters of radiographic images with a pixel size 50 μm captured using a new 2D high-resolution digital X-ray device (BMA D3A Medical Systems, France) to observe the relationship with 3D bone parameters obtained using HR-pQCT. They used 77 patients (50 men and 27 women) suffering from chronic kidney disease. The selected three sites: radius, tibia, and calcaneus. They applied fractal analysis to obtain the fractal parameter. They found moderate relationships between Hmean and bone parameters at tibia (Hmean/Tb.N: $r^2 = 0.26, p < 0.01$, Hmean/Tb.Sp: $r^2 = 0.30, p < 0.01$) where as at the radius the relationships showed slightly less correlation (Hmean/Tb.N: $r^2 = 0.24, p < 0.01$, Hmean/Tb.Sp: $r^2 = 0.24, p < 0.01$).

2.4.2 Micro-architecture evaluation: CT

Quantatitative evaluation of bone architecture, which is done by conventional bone histomorphometry, is very tedious and time consuming. Micro-CT has become the standard technique to assess the 3D trabecular bone properties. Using micro-CT, we can evaluate bone parameters such as BV/TV [%], BS/BV [mm^2/mm^3], Tb.N [mm^-1], Tb.Th [mm], and Tb.Sp [mm]. Guggenbuhl et al. [33] conducted a research in 2006, in which they examined 24 cadaveric human iliac bone. 2D projection images from 3D model with pixel size 19.3 μm were obtained. A ROI was selected from a location 2 cm under the crest and 2 cm behind the anterosuperior iliac spine. Texture features from fractal analysis and GLCM were collected. Micro-CT parameters were obtained using $SkyScan^{TM}$ 1072 software. They found significant relationships between parameters (Tb.N/ FD: $r^2 = 0.34$, Tb.Th/ FD: r^2 =35, Tb.N/VGLN: $r^2 = 0.36$).

In 2001, Chappard et al. [21] investigated relationship between fractal dimension and bone trabecular parameters. They applied different fractal analysis methods. They used femur bones collected from 148 male patients. They computed trabecular properties like bone volume (BV/TV), trabecular number (Tb.N), trabecular separation (Tb.Sp), and trabecular thickness (Tb.Th) using micro-CT $SkyScan^{TM}$ 1072 software. They applied the box-counting method to obtain the Kolmogorov dimension and lacunarity, and the sandbox method for the mass-radius dimension on bone radiographs. They observed logarithmic relationships between BV/TV and the fractal dimensions. Their study demonstrated linear relationships between Kolmogorov fractal dimension and BV/TV which appeared highly correlated ($r^2 = 0.80$). Their study identified that mass-radius fractal dimension showed best correlation. There was a significant correlation between BV/TV and mass-radius fractal dimension ($r^2 = 0.84$).

In 1996, Parkinson et al [31] carried out a study to determine the correlation between fractal parameters and trabecular parameters like BV/TV, BS/TV, Tb.Th, Tb.Sp, and Tb.N. They used biopsies from proximal femur of 25 subjects whose average age was 67.7 years. They used box counting method to extract fractal dimension. They found moderate relationships between the fractal dimension and all the histomorphometric parameters. They demonstrated that fractal dimension of trabecular bone describes complex geometry of bone [31]. Their results were moderate (Tb.N/ Fractal Dimension: $r^2 = 0.39$, BV/TV/ Fractal Dimension: $r^2 = 0.34$, Tb.Sp/ Fractal Dimension: $r^2 = 0.41$).

In 2011, Sidorenko et al. [74] evaluated human vertebrae from 111 cadavers with mean age of 80 years to extract bone parameters BV/TV, BS, Tb.N, Tb.Th, and Tb.Sp and to correlate with texture parameters of 3D micro-CT gray-level images. They applied texture measures to the 3D micro-CT images of humans vertebra specimens in vitro. They measured Minkowski fractal dimension and finite element method parameters. Significant correlation were found between parameters (BV/Tv / Minkowski FD: $r^2 = 0.37, p < 0.01$), Tb.N/ Minkowski FD: $r^2 = 0.50, p < 0.01$). Similarly, in 2010, Nogueira et al. [61], conducted the study on different skeletal sites: tibia, fibula, femur, cuboid, and humerus. They compared their results and other research works which used conventional bone histomorphometry. Their results showed that micro-CT results outperformed the results using conventional bone histomorphometry.

Relationship between 2D radiographic texture features and 3D trabecular bone properties was examined for the diagnosis of osteoporosis in the study of Apostol et al. [7]. Thirty-three femoral neck and calcaneus bone samples were evaluated for the study. Bone images were imaged using 3D-synchrotron x-ray micro-CT with a voxel size 15 μm. Two ROIs were extracted from different skeletal sites: femoral neck and calcaneus. These images were used to quantify the 3D trabecular bone properties and to simulate the realistic x-ray radiographs for texture analysis. Texture analysis method such as co-occurrence matrix and fractal dimension were applied on the images. Their result showed that fractal dimension texture parameter can predict unto 93% of the variance of 3D trabecular bone parameters.

Ouyang et al. [65] conducted a study with the aim to measure bone architecture as well as BMD and texture analysis to improve the estimation of bone strength. They used 26 human cadaveric vertebrae which were cut along superior-inferior, medial-lateral, and anterior-posterion orientations. Radiographs of these bone cubes were taken using a laser scanner with a pixel size 50 μm $\times$ 50 μm. Quantitative computed tomography was used to measure trabecular BMD. Parameters such as apparent bone fraction (ABV/TV), number of nodes (N.ND), and mean intercept separation (I.Sp) were measured. Fractal analysis was applied on bone radiographs. Their result showed that texture parameters can explain the trabecular properties with significant relationships ($r^2 = 0.2 - 0.6$).

In the study of Diederichs et al. [29], 30 calcanei in 15 human cadaveric samples were imaged using multi-detector CT (MDCT) to extract texture features. Gray level co-occurrence matrix and Minkowski fractal dimension (MD) were used on the images. They used micro-CT (voxel size: 16 μm) to determine the trabecular properties such as BV/TV, Tb.N, Tb.Th, and Tb.Sp. QCT was used to measure the BMD. Significant correlations were found between bone parameters and texture parameters (BV/TV /Contrast: r^2 = 0.35, Tb.N/Contrast: $r^2 = 0.24$) at $p < 0.05$ significant level. They also demonstrated that the combination of BMD and texture features performed better with 3D bone parameters than each parameters alone.

Winzenrieth et al. [79] in 2012 determined the correlation between 3D trabecular bone architecture parameters and trabecular bone score (TBS), which is a texture parameter that measures the local variations in gray level and is correlated with the number of trabeculae. TBS was directly evaluated from 2D projection images obtained from 3D micro-CT reconstruction. MicroView (GE Healthcare, MI) was used to obtain 3D trabecular bone parameters. Significant correlations were found between TBS and 3D bone parameters (Connectivity: $r^2 = 0.75$, Tb.N: $r^2 = 0.65$, Tb.Sp: $r^2 = 0.49$). They also showed that the degradation of image resolution and the presence of noise affected the correlations between texture features and 3D bone parameters.

2.4.3 Micro-architecture evaluation: DXA

Hans D. et al. in 2011 [35] examined 30 dry human vertebrae (lumber and thoracic) to investigate the association of TBS and BMD with 3D HR-CT micro architecture parameters. DXA was used to measure the BMD and TBS. HR-CT (isotropic 93 μm voxel size) measured the 3D parameters (BV/TV, Tb.Th, Tb.N,

and Tb.Sp). Significant correlations were found between TBS and 3D parameters (TBS/ BV/TV: $r^2 = 0.28$, TBS/Tb.Th: $r^2 = 0.31$, TBS/Tb.N: $r^2 = 0.54$, TBS/Tb.Sp: $r^2 = 0.40$). BMD was also correlated with 3D parameters. But the combination of BMD and TBS performed better than each parameter alone and explained 65% of the variance in BV/TV, 51% of the variance in Tb.Th, 63% of the variance in Tb.Sp, and 82% of the variance in Tb.N.

In 2012 Roux et al. [71] investigated an *ex vivo* study to observe the relationship between TBS and bone micro architecture and mechanical behaviour of human vertebrae. They used lumber vertebrae from 16 donors (7 men and 9 women). TBS was extracted from DXA images and micro-CT device ($SkyScan^{TM}1076, Belgium$) was used to collect trabecular bone properties. BV/TV, Tb.Th, and structure model index (SMI) were measured. They found significant correlation between TBS and other parameters (Tb.Th: $r^2 = 0.35$, SMI: $r^2 = 0.38$, stiffness: $r^2 = 0.40$). They showed that the combination of Tb.Th, TBS and SMI performed better than each parameter alone and explained 79% of the variance in stiffness.

Silva et al. [75] in 2013 conducted a study to assess TBS from spine DXA images with high-resolution peripheral quantitative computed tomography (HRpQCT) bone parameters. TBS is a novel gray-level texture feature from DXA images. They used 22 postmenopausal women. The subjects were scanned for DXA measurement and TBS was computed from DXA images and HR-pQCT measurements were done at the distal radius and tibia. TBS was highly correlated with all HRpQCT bone parameters except trabecular thickness at the radius. At the tibia, TBS was correlated with volumetric density, trabecular bone volume, and whole bone stiffness. TBS was not correlated with trabecular thickness at the tibia.

2.4.4 Micro-architecture evaluation: MRI

Magnetic resonance imaging (MRI) has been a suitable imaging technique to observe the changes in trabecular bone architecture. Pothuaud et al. [66] in 2000 conducted a research to determine the correlation between fractal properties and trabecular bone properties of the fracture site - the hip. Trabecular bone images were obtained by MRI. They extracted the Minkowski fractal dimension parameter from MRI images. They founda statistically significant relationship between fractal dimension and porosity in the 3D architecture. A significant relation was observed between fractal dimension and trabecular number ($r^2 = 0.74$). There was also a significant relationship between porosity and trabecular number ($r^2 = 0.67$).

In the study of Cortet et al. [26], they examined 24 cadaveric specimen to determine the relationship between 2D MRI images and 3D micro-CT bone parameters. The study reported significant relationships between 2D and 3D parameters. Fractal dimension was significantly correlated with Tb.Th, Tb.N, BV/TV, and Tb.Sp. Similarly, Mueller et al. [60] in 2005 investigated the relation between 3D-based scaling index method (SIM) and 2D bone histomorphometric parameters. MRI images of forty postmenopausal women with and without osteoporotic spine fracture were obtained using 1.5 T MR scanner (ACS-NT, Philips, Netherlands). Oval ROIs placed at the proximal section of the radius were selected. The SIM method was applied on MRI images and histomorphometric parameters were collected from the MRI images with

a pixel size $10\mu m$. Significant relationships were found between the 2D parameters and histomorphometric measurements.

Accordingly, Zhang et al. [80] examined sixty subjects to obtain MRI images using 3-T Signa systems (General Electric, USA). Structural parameters such as ABV/TV, Tb.Sp, Tb.N, Tb.Sp, and Tb.Th were obtained. Moderate correlation were observed between the parameters. Several other studies that reported the association between 2D texture parameters and 3D bone parameters [55, 10, 9] in the trabecular bone micro architecture analysis. All of these studies provide a good opportunity to compare the performance of texture analysis of DEI images in our study with the results of these studies.

2.5 Motivation for applying texture feature coding method and local binary patterns

Texture feature coding method and local binary patterns are widely used methods in texture recognition and classification as we have previously discussed in Section 2.1. We have applied texture feature coding method and local binary patterns in our study to investigate how these texture features perform in terms of correlating with bone parameters. Although these methods have not been used in bone images to the best of our knowledge, the descriptors from both methods have been used in ultrasound images in several studies described in the next section. This will be a great opportunity for us to use these descriptors and examine their relationship with bone parameters.

2.5.1 Texture feature coding method

In 2001, Horng et al. [39] introduced a new texture analysis method called texture feature coding method for classification of medical images. They also used four other conventional texture analysis methods: GLCM, texture spectrum, statistical feature matrix, and fractal dimension. They compared texture features generated using these methods. They used 30 cases of normal liver, hepatitis and cirrhosis, identified by liver biopsy. They trained a maximum likelihood (ML) classifier for each texture analysis method using those 30 ultrasound images and then tested them on 90 other samples. Their experimental results showed that TFCM outperformed all the other methods with a correct classification rate as high as 86.7. They suggested that although TFCM performed better than other texture features as an independent texture feature, the integration of texture features obtained by different methods may result in even better classification.

Horng et al. in 2008 [50] proposed a study to apply the texture analysis method to classify the different disease groups that are normal, tendon inflammation, calcific tendonitis and rotator cuff tear. The supraspinatus tendon is usually involved among above-mentioned diseases progression. Four texture analysis methods that texture feature coding method, gray-level co-occurrence matrix, fractal dimension and texture spectrum are used to extract features of tissue characteristic of supraspinatus tendon. The mutual information method is independently used to select powerful feature among four texture analysis method, further,

the radial basis function network to classify the ones into the four disease group. Experimental results tested on 85 images reveal that the proposed system can achieve a 84% accuracy rate.

2.5.2 Local binary patterns

Dimitris et al. [42] developed a texture descriptor called fuzzy local binary pattern (FLBP). They incorporated fuzzy logic in LBP methodology. Based on fuzzy rules, LBP pixel values were transformed to multiple fuzzy variables and a FLBP histogram was generated. Ultrasound images were used to evaluate the FLBP performance. Their study showed a 86% accuracy for classifying nodular vs normal thyroid tissues. This study demonstrated that FLBP performed better than other features like GLCM. This study showed that the use of texture analysis based on LBP is promising for medical image texture analysis.

Local binary patterns (LBP) have been used in face recognition. Dynamic texture is also an area where LBP is used. Zhao et al. [51] in 2007 examined two DT databases (MIT and DynTex databases). An extension of local binary pattern, volume local binary pattern (VLBP), was used. Texture was modelled with VLBP by combining motion and appearance. They implemented block-based method to deal with facial expressions in which local information and spatial locations were considered. They showed that classification rates were 100 percent and 95.7 percent using LBP and 100 percent and 97.1 percent using VLBP for the MIT and DynTex databases.

2.6 Discussion

Extensive studies of trabecular bone texture analysis have given an improved way to understand the bone architecture. Various texture methods demonstrated that these methods have great potentiality for bone micro architecture assessment. It has been shown that texture features from 2D radiographs can correlate with 3D bone micro architecture and able to predict osteoporotic fracture. We can find some of the limitations in these studies: soft tissue can greatly affect the bone texture on radiographs and the number of subjects used in these studies are low. However, trabecular properties and fractal analysis of images are important for understanding bone architecture. Texture feature coding method and local binary patterns may improve the assessment of bone micro-architecture. Based upon these findings, we aim to determine the correlation between texture features of 2D images and 3D bone properties. Texture features were extracted from DEI images using GLCM, TFCM, LBP and fractal dimension methods. 3D trabecular bone properties were obtained using micro-CT.

Chapter 3

Materials and Methods

3.1 Image Dataset

Images of human distal wrist bones (radii) were taken from 15 bones. These 15 bones were collected from the University of Saskatchewan anatomical teaching collection. Imaging was conducted at the Canadian Light Source synchrotron on the Biomedical Imaging and Therapy (BMIT) beam lines. The bending magnet beam line was used at 40 KeV with protocols [23]. Images at seven different points (top, 0.5, 0.25, 0.125, -0.5, -0.25, and -0.125) on the rocking curve for horizontal and vertical orientations of each bone were captured. These images are 4008 $\times$ 2671-pixel 16-bit float grayscale images with a pixel size of 20μm. Figure 3.1 shows images for horizontal and vertical orientations. These images were preprocessed. Image pre-processing steps are explained with results in detail below.

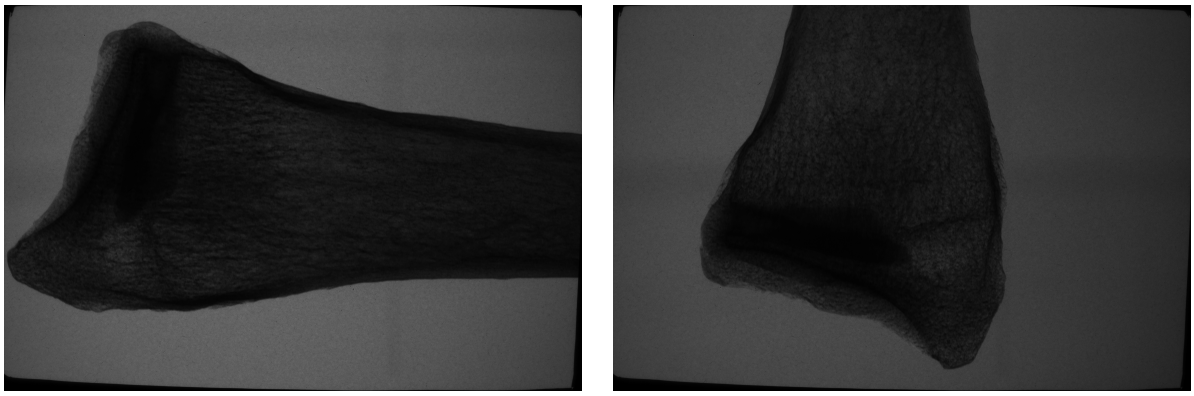

Figure 3.1: Images of horizontal and vertical orientations

3.2 Image Preprocessing

3.2.1 Background

Some x-ray synchrotron images are subject to digitization errors. The reference grayscale in such images is not always monotonic due to extrema within individual steps resulting from noise. Filtering is the way to deal with noise. A non-local means filter, which averages all observed pixels to recover a single pixel, was

employed. A blockwise implementation of NL-means was used which outperformed all the other filters in a research conducted by Coupe et al. [28]. That is why we chose to use this blockwise NL-means algorithm to denoise our image dataset. We have also used bilinear interpolation to reduce gradients in the images caused by the slight misalignment of the crystal analyzer used in DEI technology. NL-means filter and bilinear interpolation are described below.

Non Local Means Filter

In 2006, Buades et al. [13] introduced the first non-local means (NL-means) algorithm. In our study we used the blockwise implementation of the NL-means algorithm described in [28]. This algorithm makes assumptions about the image in that the image contains self-similarity. It does not comply with other method such as Gaussian filtering. Self-similarity for texture synthesis was developed by Efros and Leung [30]. Figure 3.2 below shows an example of self-similarity. In this Figure 3.2, we observe three pixels p, q_1, and q_2 and their neighborhoods. Pixels p and q_1 have similar neighborhoods but pixels p and q_2 have neighborhoods which are not similar. Similar neighborhoods are observed in adjacent pixels [13].

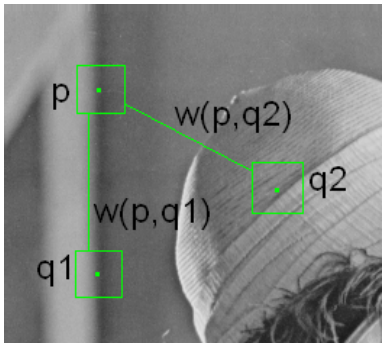

Figure 3.2: Image pixels and its neighbourhood similarity [30]

We can use the assumption about self-similarity to denoise an image. So, we can denoise a pixel from its neighbourhood pixels where the neighbourhood is similar to the reference pixel's neighborhood. The formula to denoise an image using non-local means filter will be [13]:

$$NL\left(V\right)\left(p\right)=\sum_{q\epsilon V}W\left(p,q\right)V\left(q\right) \tag{3.1}$$

In the Equation, above, V is the noisy image, and $w(p,q)$ is the weight for pixel q when averaging to find the filtered intensity of p. Each pixel's output intensity is a weighted average of all the pixels in the image [13, 30]. In Figure 3.2, above, the weight $w(p,q_1)$ is much greater than $w(p,q_2)$ because pixels p and q_1 have similar neighborhoods. We use the following formula to compute the similarity of two neighborhoods [13]:

$$d\left(p,q\right)=\left\|V\left(N_p\right)-V\left(N_q\right)\right\|_{2,F}^2 \tag{3.2}$$

In the Equation, above, let N_i be the square neighbourhood. We calculate the sum of the square difference between two neighborhoods. The neighborhood filter, denoted as F, is applied to the squared difference of the neighborhoods. We compute the weights using the following formula [13]:

$$W\left(p,q\right)=\frac{1}{K\left(p\right)}e^{\frac{-d(p,q)}{h}} \tag{3.3}$$

where $K(p)$ is the constant used for normalization and h is the smoothing parameter. If we want a filter independent of the neighbourhood size, then we have to take the smoothing parameter, h into account because it depends on the standard deviation of the noise, σ. So, the relationship $h^2=f\left(\sigma^2,\left|p\right|,\beta\right)$ determines the automatic tuning of the smoothing parameter, where β is a constant. In order to reduce the computational time, the classical Euclidean distance is used. Then, the Eq. 3.3 becomes:

$$W\left(p,q\right)=\frac{1}{K\left(p\right)}e^{\frac{-d(p,q)}{2\sigma^2|p|}} \tag{3.4}$$

In order to reduce the computational time, a search window method was used to preselect a subset of the most relevant pixels to avoid repetitive weight computations. To avoid the expensive computation of W(p,q), as in eq 3.4, we use the following formula in which some fast heuristic tests involving the mean and variance are done.

$$W\left(p,q\right)=\begin{cases}\frac{1}{K(p)}e^{\frac{-d(p,q)}{2\sigma^2|p|}}, & if\mu_1<\frac{\mu(N_p)}{\mu(N_q)}<\frac{1}{\mu_1}and\ \sigma_1^2<\frac{\sigma(N_p)}{\sigma(N_q)}<\frac{1}{\sigma_1^2}\\ 0 & otherwise.\end{cases} \tag{3.5}$$

where N_p and N_q are local neighbourhoods of p and q pixels respectively, $\mu(N_p)$ and $\sigma(N_p)$ represent the mean and variance of the local neighborhood of pixel p and $\mu(N_q)$ and $\sigma(N_q)$ represent the mean and variance of the local neighborhood of pixel q.

A blockwise implementation of non-local means is developed. Using this approach we can reduce the complexity of the algorithm. This algorithm consists of three steps: partitioning the search window in blocks with overlapping supports, restoration of these blocks, and restoring the pixels values of the blocks. So, according to this algorithm, a block size of $(2M+1)^2$, denoted as B_p, is selected from the search window, where $M\in S_p$ and S_p is the search window. The restoration of the blocks is performed using the following formula:

$$NL(B_p)=\sum_{B_q\epsilon S_p}w(B_p,B_q)q \tag{3.6}$$

Finally, the restored intensity of voxel is then defined as follows:

$$NL(p)=\frac{1}{|A_p|}\sum_{x\epsilon A_p}A_p(x)) \tag{3.7}$$

where A_p is a vector of the final restored intensity of pixel p.

Bilinear Interpolation

Bilinear interpolation is used to reconstruct the background intensity of images [39]. Each pixel intensity is adjusted based on the scale constant. Bilinear interpolation used four pixels in the image matrix to find the value of the reference pixel. Bilinear interpolation used distance-weighted averages to find the new value of the reference pixel [39]. All the pixels in the image matrix will go through the same process. In the

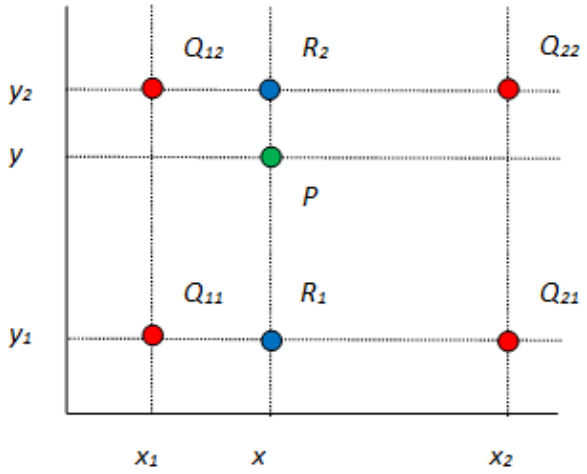

Figure 3.3: Bilinear Interpolation (Redrawn)[39].

Figure 3.3, the green dot (P) is the interpolation point, the four red dots (Q_{11}, Q_{12}, Q_{21}, and Q_{22}) are the data points, and R_1 and R_2 are points on the line. In order to get the value of the function f at the point $P = (x, y)$ we do linear interpolation in the x-direction which yields [39]:

$$f(R_1) = \frac{x_2 - x}{x_2 - x_1} f(Q_{11}) + \frac{x - x_1}{x_2 - x_1} f(Q_{21}) \tag{3.8}$$

where $R_1 = (x, y_1)$, and

$$f(R_2) = \frac{x_2 - x}{x_2 - x_1} f(Q_{12}) + \frac{x - x_1}{x_2 - x_1} f(Q_{22}) \tag{3.9}$$

where $R_2 = (x, y_2)$. Then we proceed by interpolating in the y-direction[39]:

$$f(P) = \frac{y_2 - y}{y_2 - y_1} f(R_1) + \frac{y - y_1}{y_2 - y_1} f(R_2) \tag{3.10}$$

This gives us the result of $f(x, y)$. An example of using bilinear interpolation on our image dataset is given later in this chapter.

3.2.2 The Preprocessing Pipeline

Image Correction

In the image aquisition process, images get incorporated with background noise and gets slight variation in exposure or detector response. So we needed to correct the images. This correction is needed for all CCD/electronic images. We have the following equation to correct the images.

$$I_{corr} = \frac{I_{raw} - Dark}{Flat - Dark} \tag{3.11}$$

where I_{corr} is the corrected image, I_{raw} is the image, the dark image is taken when detector is on but the beam is off, so, we get an image consisting mostly of detector noise, and the flat image is taken when the detector and beam are on but the object is not there. Dark correction removes background noise and flat correction removes variation in exposure or detector response. Figure 3.4 shows horizontal corrected image and its filtered image.

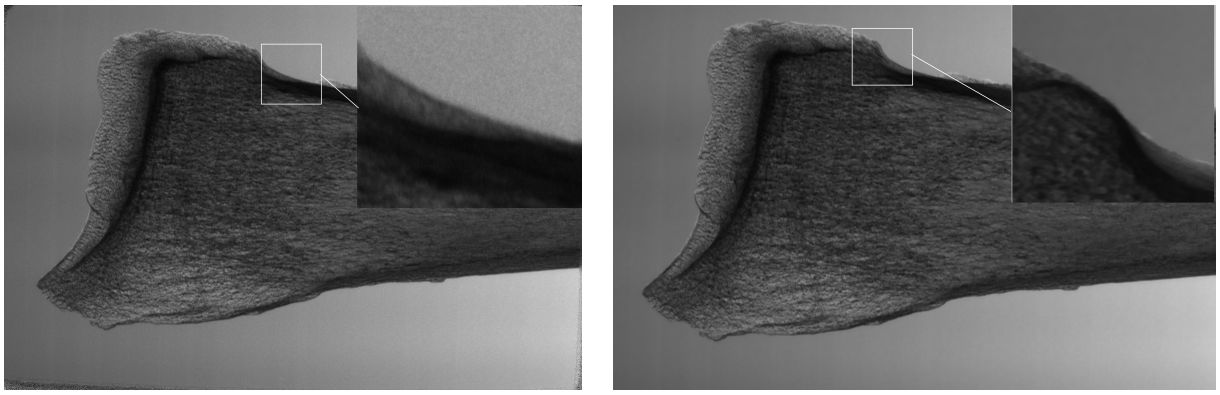

Figure 3.4: Corrected image with noise and filtered image for horizontal orientation.

Image Filtering

The images were then filtered using non-local means filter method. As non-local means filter has some parameters described in the previous section, we used radius of the filter block window = 3 (7×7), radius of the search window block = 10 (21×21), block step size = 2, and threshold 0.75. The filtered image is denoted as I_F. Figure 3.5 shows some filtered images. If we take a closer look at the insets in the images in Figure 3.4 and in Figure 3.5, we can observe that the images were greatly denoised.

Image Normalization

During image acquisition there were errors because of the misalignment of the crystal analyzer. As a result, there is an observable gradient in the background of the images. So, we have to go through a normalization process which includes bilinear interpolation. We selected four data points ($Q_{11}, Q_{12}, Q_{21}, and\ Q_{22}$) in the

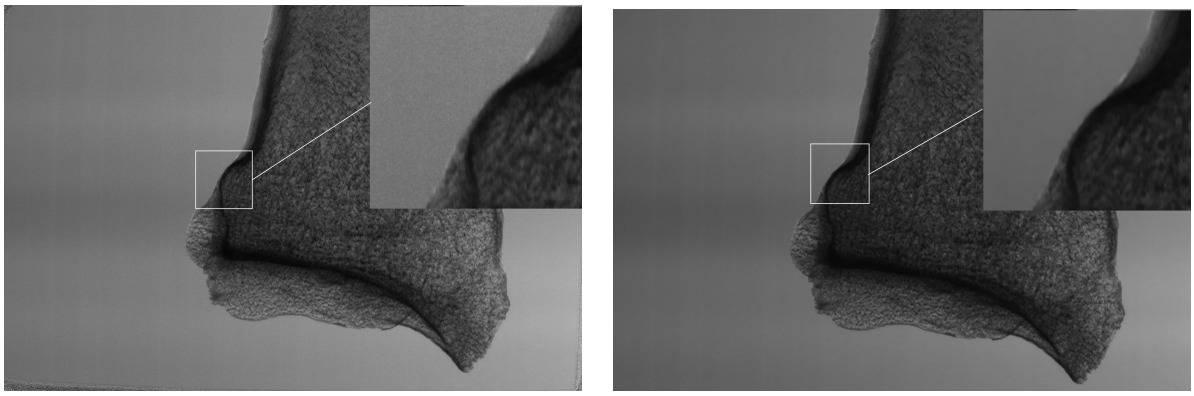

Figure 3.5: Corrected image with noise and filtered image for vertical orientation.

images to find the value of $p(x, y)$ by applying bilinear interpolation to remove the gradient. We have already mentioned that the size of images are 4008 $\times$ 2671-pixels. We selected the coordinates for our data points which are (256, 256), (256, 2415), (3752, 256), and (3752, 2415). These points were chosen because they are always outside the bone area and therefore sample the background gradient, which allows for the interpolation of the gradient at all points in between. Figure 3.6 shows bilinear interpolation being applied on image dataset. The formula for normalzation is given below.

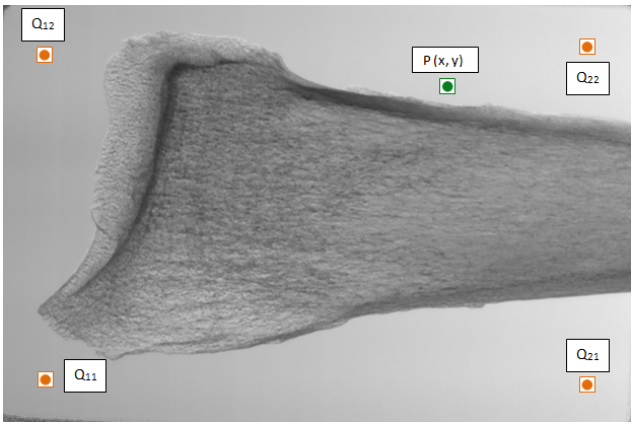

Figure 3.6: Bilinear interpolation on an image.

$$I = \frac{I_F}{\gamma / \gamma_r \left(x_r, y_r\right)} \tag{3.12}$$

where I is the final processed image, I_F is the filtered image, γ is the gradient field with bilinear interpolation, and $\gamma_r \left(x_r, y_r\right)$ is the reference point. Figure 3.7 shows final processed images.

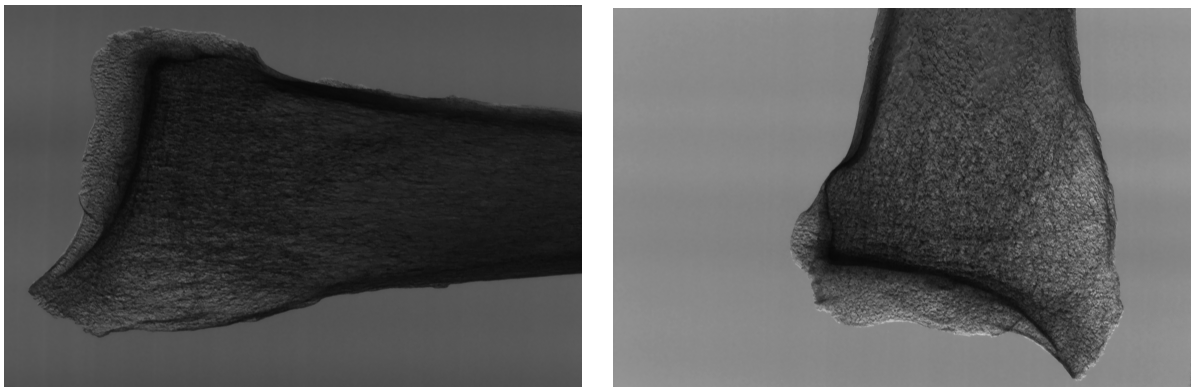

Figure 3.7: Processed images after normalization.

3.2.3 DEI Image Generation

For every point on the rocking curve, we have two images from the high and low angle sides. Using these images we generated DEI images as mentioned in [18]. The following two equations represent the intensities of the low-angle side (θ_L) and high-angle side (θ_H) images.

$$I_L = I_R \left(R\left(\theta_L\right) + \frac{dR}{d\theta}\left(\theta_L\right) \Delta\theta_Z \right) \tag{3.13}$$

$$I_H = I_R \left(R\left(\theta_H\right) + \frac{dR}{d\theta}\left(\theta_H\right) \Delta\theta_Z \right) \tag{3.14}$$

where R is the analyzer reflectivity, $\Delta\theta_Z$ is the refraction angle, and I_R is the refraction angle image. This process was applied on a pixel-by-pixel basis to the diffracted images from the low-angle and high-angle sides of the rocking curve. Finally we find the DEI images using the following formula.

$$DEI = \frac{I_L - I_H}{I_L + I_H} \tag{3.15}$$

3.3 Texture Feature Methods

3.3.1 Texture Feature Coding Method

Texture Feature Coding Method (TFCM) was introduced by Horng et al. [39]. In TFCM, a feature image is generated from a gray level image. The feature image is represented by a texture feature number (TFN). A 3×3 texture unit in an image is used to generate the TFN. The texture unit -
considers the gray-level variations of its eight surrounding pixels. The ideas of gray-level histogram and co-occurrence matrix are used in TFCM. A TFN histogram and a TFN co-occurrence matrix (CM) is generated from the TFN obtained previously. TFCM also uses maximum entropy criterion that is used to find optimal gray-level variation tolerance [39].

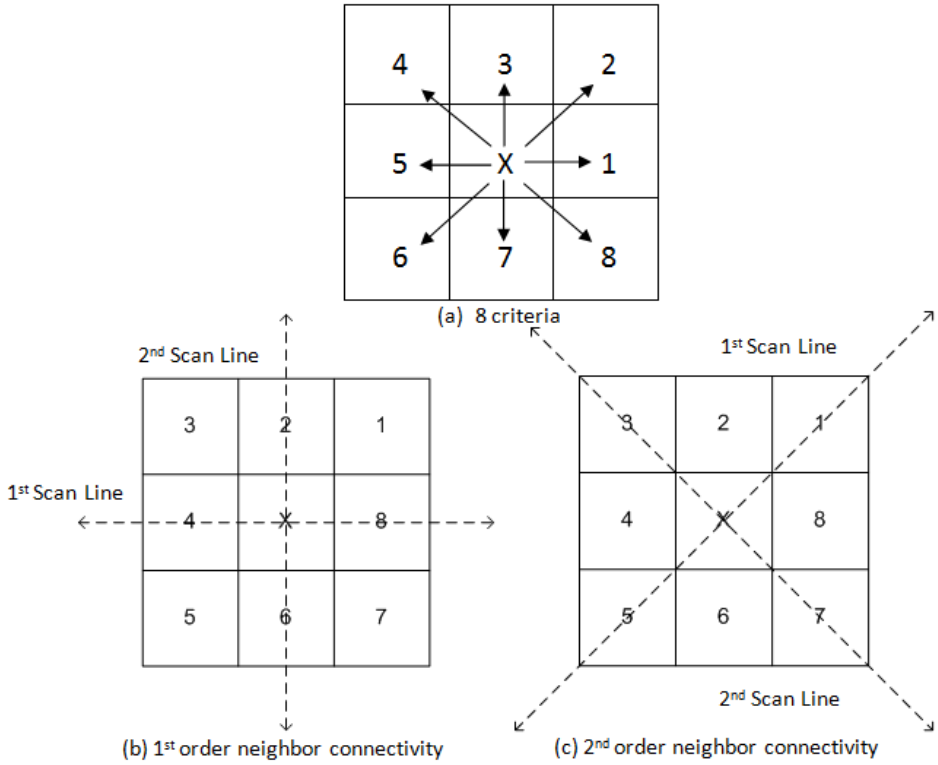

Figure 3.8: First-order and second-order 4-eighbor connectivity [1] .

Figure 3.8(a) shows a 8-neighbor connectivity of a pixel X. Pixels labeled as 2, 4, 6, and 8 are referred as first-order neighboring pixels shown in Figure 3.8(b). The other four pixels labeled as 1, 3, 5, and 7 are referred as second-order neighboring pixels as shown in Figure 3.8(c). Let a, b, c be three spatial coordinates with gray levels $G(a), G(b)$ *and* $G(c)$ respectively. Equation 3.16 shows four types of gradient changes.

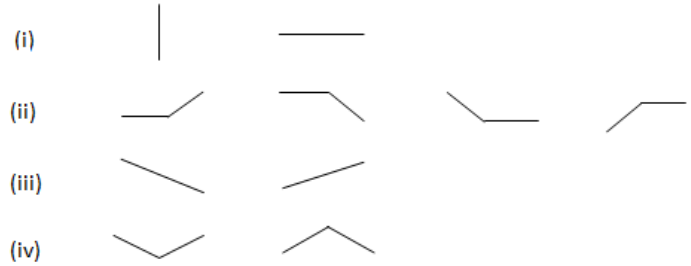

Figure 3.9: Types of gray-level variations [39].

$$(i)\ if\ \ (|G_a - G_b| \leq \Delta) \cap (|G_b - G_c| \leq \Delta)\,,$$

$$(ii)\ if\ \ [(|G_a - G_b| \leq \Delta) \cap (|G_b - G_c| \geq \Delta)] \cup [(|G_a - G_b| \geq \Delta) \cap (|G_b - G_c| \leq \Delta)]\,,$$

$(iii)\ if\ \ [(|G_a - G_b| > \Delta) \cap (|G_b - G_c| > \Delta)] \cup [(|G_b - G_a| > \Delta) \cap (|G_c - G_b| > \Delta)]\,,$

$$(iv)\ if\ \ [(|G_a - G_b| > \Delta) \cap (|G_c - G_b| > \Delta)] \cup [(|G_b - G_a| > \Delta) \cap (|G_b - G_c| > \Delta)] \tag{3.16}$$

In the Eq. above, Δ is the desired gray level tolerance. The gray-level variations of first-order and the second-order connectivity can be represented by a pair of integers (s, t) as shown in Table 3.1.

Table 3.1: Combination coding of gray-level variation [50].

		1st Scan Line			
		(i)	(ii)	(iii)	(iv)
2nd Scan Line	(i)	1	2	3	4
	(ii)	2	5	6	7
	(iii)	3	6	8	9
	(iv)	4	7	9	10

Finally, we can define a TFN histogram by the following Equation:

$$p_{\Delta}\left(n\right) = \frac{N_{\Delta}\left(n\right)}{N}, \quad n\,\epsilon\,\{1, 2, 3, ...41\} \tag{3.17}$$

The TFN (x, y) of a pair of integers (S, T) of any images can be computed as follows:

$$TFN(x, y) = \alpha\left(x, y\right) \times \beta\left(x, y\right) \tag{3.18}$$

where $\alpha(x, y)$ and $\beta(x, y)$ are the values obtained from Table 3.1. TFCM uses the maximum entropy criterion to determine the best tolerence Δ [39]. The optimal gray value variation tolerance, Δ, is computed by finding the value of Δ that maximizes the following Equation:

$$H_{TFN}(\Delta) = -\sum_{x}\sum_{y} p_{\Delta}\left(TFN\left(x, y\right)\right) log p_{\Delta}\left(TFN\left(x, y\right)\right), \tag{3.19}$$

where (x, y) is taken over all pixels in 15 sample images used in our study. TFCM uses a co-occurrence matrix (CM) on TFNs of the feature images, which is obtained by using following Equation [39]. This co-occurrence matrix (CM) matrix defines the TFCM texture features.

$$p_{\Delta}\left(i, j|d, \theta\right) = \frac{N_{\Delta,d,\theta}\left(i, j\right)}{N_t}, \qquad i, j\,\epsilon\,\{0, 1, 2, ...41\} \tag{3.20}$$

where i and j are two gray-levels and $N_{\Delta,d,\theta}(i,j)$ denotes the number of transitions between two pixels whose gray-levels are i and j with d-pixels apart and orientation θ. In the above Eq. 3.20, normalizing denotes the probability of gray-level transitions where N is the number of total gray-level transitions in the CM.

TFCM Texture features

According to Horng et al. [39], seven texture features were defined. The features are defined as follows -

Coarseness (Coarse):

$$Coarse = \sum x \sum y p_{\Delta^*}(41) \tag{3.21}$$

A pixel corresponding to TFN 41 represents a drastic change in its 8-connectivity neighbourhood and it also provides a good indication of coarseness.

Homogeneity (Hom):

$$Hom = \sum x \sum y p_{\Delta^*}(0) \tag{3.22}$$

A pixel corresponding to TFN 0 represents no significant change in its 8-connectivity neighbourhood and it also provides a good indication of homogeneity.

Mean convergence (MC):

$$MC = \sum_{n=0}^{41} \frac{|n \cdot p_{\Delta^*}(n) - \mu_{\Delta^*}|}{\sigma_{\Delta^*}} \tag{3.23}$$

This MC feature descriptor indicates how closely the texture approximates the mean of the TFNs.

Variance (Var):

$$Var = \sum_{n=0}^{41} (n - \mu_{\Delta^*})^2 \cdot p_{\Delta^*}(n) \tag{3.24}$$

The variance measures deviation of TFNs from the mean.

Code entropy (CE):

$$CE = -\sum_{i=0}^{41}\sum_{j=0}^{41} p_{\Delta^*}(i,j|d,\theta) log\ p_{\Delta^*}(i,j|d,\theta) \tag{3.25}$$

Code similarity (CS):

$$CS = \sum_{t=1}^{41} p^2{}_{\Delta^*}(i,j|d,\theta) \tag{3.26}$$

This feature descriptor is used to calculate the density of same TFNs in its 8-connectivity neighborhood.

Resolution similarity (RS):

$$RS = \sum_x \sum_y \frac{p(i,j;x,y)}{1+(i-j)^2} \tag{3.27}$$

This feature descriptor provides information about the joint probability $p(i, j|d, \theta)$ of a pixel at $(x,\ y)$ whose TFN is i at $\Delta = 0$ and TFN is j at Δ^*. The higher the RS, the lesser is the change in TFNs of the same pixel, thus, the higher RS feature implies the texture is more rough.

3.3.2 Local Binary Patterns

Ojala et al. [63] introduced the LBP operator, which was based on a 3×3 local neighborhood with a 45° quantization of the angular space provided by the eight neighborhood (interpolation) points. The neighborhood represents the local texture around a central pixel. The value of each pixel of this neighborhood is thresholded using the value of the central pixel [63].

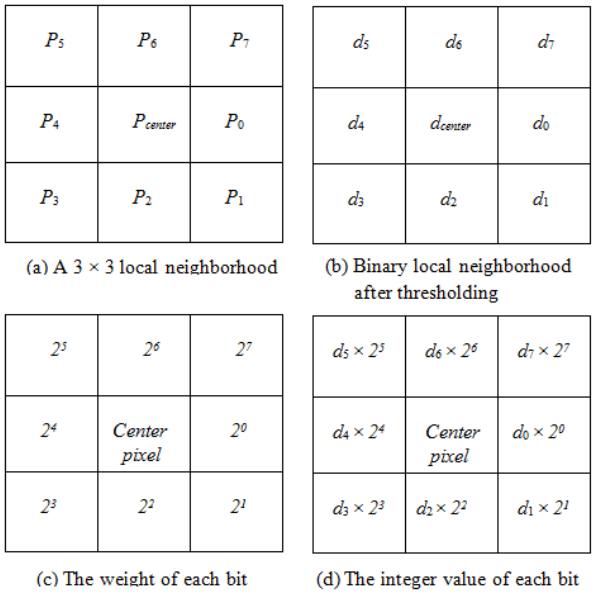

Figure 3.10: LBP computation scheme

Figure 3.10(a) depicts a 3×3 neighborhood, where p_i $(0 \leq i \leq 7)$ corresponds to the pixel locations and pcenter is the central pixel. The gray value of each pixel p_i is denoted as g_i, and g_{center} is the central pixel. According to Equation 2.1, the 3×3 neighborhood can be characterized by a set of binary values d_i $(0 \leq i \leq 7)$, which is shown in figure 3.10 (b) after thresholding each pixel by the central pixel gray value. Therefore, based on the binary values in figure 3.10(b) and the corresponding weights for each bit in figure 3.10(c), the LBP code can be computed using Eq: 3.28, which is the sum of the value of each bit shown in figure 3.10(d). Thus, the local texture information is represented by an 8-bit binary number with an integer value. The possible number of LBP codes is 256, ranges from 0 to 255. A circular layout is used in many studies since the distance between the central pixel and diagonal pixels is not the same as the distance from the central pixel and the horizontal or vertical pixels.

$$d_i = \begin{cases} 1, & g_i \geq g_{center} \\ 0, & g_i < g_{center} \end{cases} \tag{3.28}$$

where

$$LBP_8 = \sum_{i=0}^{7} d_i * 2^i \tag{3.29}$$

256 different binary patterns result from thresholding the eight interpolated intensities within the 3×3 local neighborhood. Interpolation positions p_i move along the perimeter of the circle around the central pixel when an image is rotated as shown in Figure 3.10(a). So, rotation of a particular pattern will result in a different LBP value. In the case of rotation by an increment of 90^o, the result is a circular permutation of the bit pattern for the unrotated neighborhood. 000000000 and 11111111 are the two patterns remain the same against any rotation. In order to overcome this deficiency, rotationally invariant 8-bit local binary patterns have been defined [64]:

$$LBP_8^{ri} = min\left\{ROR\left(LBP_8, i\right)|i = 0, 1, ...7\right\}, \tag{3.30}$$

where ROR(x, i) performs a circular bitwise right shifts on the 8-bit number x. So, we can get 36 different values referred as 36 unique rotation invariant local binary patterns. Figure 3.11 depicts the computation.

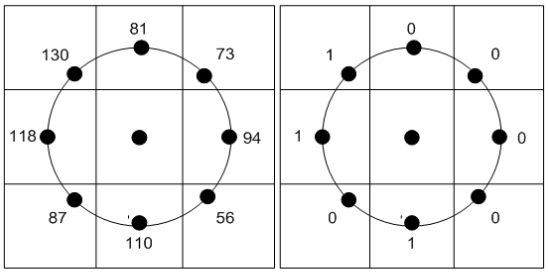

(a) A 3 × 3 circular local neighborhood with pixel values (b) The binary value for each bit

Figure 3.11: Computing rotation invariant in a 3 × 3 neighborhood

The performance of the 36 LBP_8^{ri} patterns varies greatly in discrimination of rotated textures: some patterns sustain rotation quite well while others do not and only confuse the analysis [63]. So, using all 36 patterns leads to suboptimal result and to overcome this, a uniformity measure U is defined. The uniformity measure U corresponds to the number of transitions (bitwise 0/1 changes) in the bit pattern when read from right to left. For example, U (00010000) = 2. The smaller the uniformity value of a pattern is, the better the pattern will sustain rotation. The patterns having U value at most 2 are designated as "uniform patterns". The rotation invariant LBP uniform patterns, LBP_8^{riu2} is defined as follows:

$$LBP_8^{riu2} = \begin{cases} \sum_{i=1}^{8} d_i & U\left(LBP_8\right) \leq 2, \\ 9 & otherwise \end{cases} \tag{3.31}$$

The nonuniform patterns are all represented by the same value of 9, so the possible values of LBP_8^{riu2} are integers in the interval [0, 9]. All 8-bit rotation invariant uniform patterns are shown in figure 3.12.

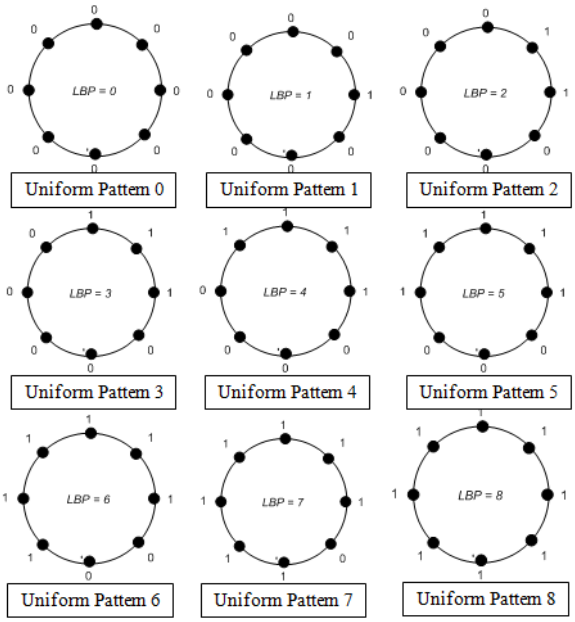

Figure 3.12: The 8-bit rotation invariant uniform patterns

In order to get better classification accuracy, a more precise resolution of 22.5° is used to quantize the angular space. To obtain this, a 5×5 neighborhood is used because newly added eight interpolation points will not provide too much new information if they are inserted in a 3×3 neighborhood. So, we have 16-bit local binary patterns. Like the 3×3 neighborhood, the 5×5 neighborhood is thresholded by the central pixel into a 16-bit binary pattern. Figure 3.13 illustrates a circular layout of a 5×5 local neighborhood.
The binary LBP code is computed similar to the 8-bit binary LBP codes and has the following Equation:

$$d_i = \begin{cases} 1, & g_i \geq g_{center} \\ 0, & g_i < g_{center} \end{cases} \tag{3.32}$$

$$LBP_{16} = \sum_{i=0}^{15} d_i * 2^i \tag{3.33}$$

Again, the definitions of rotation invariant 16-bit LBP_{16}^{ri} and uniform patterns LBP_{16}^{riu2} are as follows:

$$LBP_{16}^{riu2} = min\left\{ROR\left(LBP_{16}, i\right) | i = 0, 1, ...15\right\}, \tag{3.34}$$

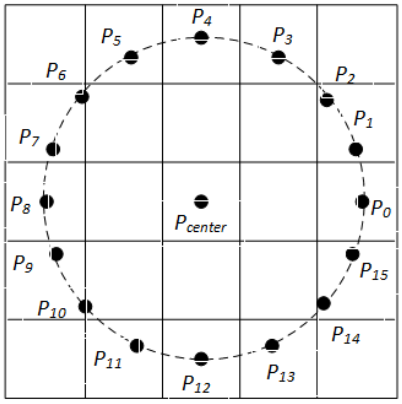

Figure 3.13: a 5×5 neighborhood

$$LBP_{16}^{riu2} = \begin{cases} \sum_{i=1}^{16} d_i & \bigcup(LBP_{16}) \leq 2, \\ 17 & otherwise \end{cases} \tag{3.35}$$

LBP_8^{riu2} has 18 output values: 0 to 16 refers to 17 uniform patterns, and value 17 refers to nonuniform patterns. In this experiment we used histograms of 16-bit LBP_8^{riu2} patterns to encode local texture descriptions.

3.3.3 Fractal Dimension and Lacunarity

Fractal analysis is a statistical method for texture analysis [27]. Fractal dimension is the operator calculated from fractal analysis. Fractal dimension describes the complexity and roughness of bone texture [47]. The fractal dimension increases with the degree of roughness. There are several methods used in fractal analysis. Among the fractal analysis methods, the fractal signature method [44], box-counting method [27], Fourier method [44], and maximum likelihood based on fractional Brownian motion [47] are widely used. Some of these methods can be used only with binary images. Box counting method uses binary images. In our study we used box counting method. Methods based on Fourier analysis or fractional Brownian motion require gray-level images [17]. The texture of images obtained by radiography shows the properties of fractals [44]. Some fractal parameters can be evaluated on histological sections, CT images, and MRI scans [27]. Fractal dimension describes how the pattern of an image changes when an spatial scale is changed over the image to measure the roughness of the image. Fractal dimension, D_f, is computed using the following formula [3]:

$$D_f = logN/log\varepsilon \tag{3.36}$$

The box counting method is calculated in both 2D and 3D. Box counting also counts a feature called lacunarity. Lacunarity is also defined as gappiness and heterogeneity. It is denoted as λ. The following equation defines lacunarity [3].

$$\lambda_{\varepsilon,g} = CV_{\varepsilon,g^2} = (\sigma_{\varepsilon,g}/\mu_{\varepsilon,g})^2 \tag{3.37}$$

3.3.4 Gray Level Co-occurrance Matrix

The Gray Level Co-occurrence Matrix (GLCM) texture measurements were proposed by Haralick in the 1970s [36]. The GLCM describes how often pixel values (grey levels) occur in an image. The GLCM described here is used for a series of "second order" texture calculations. Second order measures consider the relationship between groups of two (usually neighboring) pixels in the original image [36]. Figure 3.14 is an illustration of a test image and its associated values.

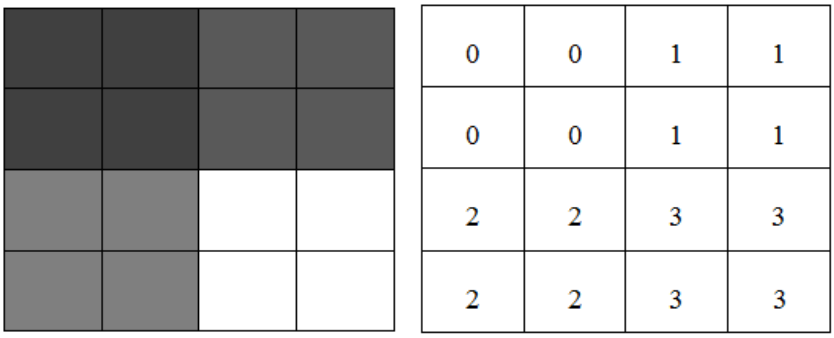

0	0	1	1
0	0	1	1
2	2	3	3
2	2	3	3

Figure 3.14: A test image and its associated values

A reference pixel and a neighbour pixel are defined to consider the relationship as mentioned earlier that second-order statistics considers pixel's relationship. For this example, the neighbour pixel is chosen to be the one to the right of each reference pixel. This relationship can be expressed as (1, 0), which states that 1 pixel in x direction, 0 pixel in the y direction. Every pixel in the image matrix becomes the reference pixel. Using this count, we generate a framework matrix. In the framework matrix, the first entry (top left cell) will the count of number of times the combination 0, 0 occurs.

We generate a transpose matrix of the framework matrix. Then a symmetrical matrix is generated. A symmetrical matrix means that same values occur in cells on opposite sides of the diagonal. For example, the value in cell (1, 3) would be same as the value in cell (3, 1). Table: 3.2 shows the calculation for symmetrical matrix.

Table 3.2: Calculation of symmetrical GLCM

Count matrix				+	Transpose				=	Symmetrical			
2	0	2	0		2	0	0	0		4	0	2	0
0	2	0	2		0	2	0	0		0	4	0	2
0	0	2	0		2	0	1	0		2	0	3	0
0	0	0	2		0	2	0	2		0	2	0	4

Using the symmetrical matrix, we finally generate a normalized symmetrical matrix which will be used

to calculate texture features. The matrix has values in a form of a probability. Probability values mean the number of times this outcome occurs divided by the total number of possible outcomes. The combination (0, 0) occurs 4 times out of 24, for a probability of 1/6 or 0.16. The probability of (0, 2) is 2/24 or .08. The symmetrical matrix can be normalized by using the equation given in Eq. 3.38. Table: 3.3 is an example of normalized symmetrical matrix.

$$P_{i,j} = \frac{V_{i,j}}{\sum_{i,j=0}^{N-1} V_{i,j}} \tag{3.38}$$

Table 3.3: Normalized Symmetrical GLCM

0.16	0.00	0.08	0.00
0.00	0.16	0.00	0.12
0.12	0.00	0.16	0.00
0.00	0.12	0.00	0.16

GLCM Texture features

Haralick et al. [36] suggested a set of 14 textural features which can be extracted from each of the gray level co-occurrence matrices. In the texture feature definitions we use the mean and variance of intensities. These measurements are given below:

Mean:

$$\mu_i = \sum_{i,j=0}^{N-1} i\left(P_{i,j}\right), \mu_j = \sum_{i,j=0}^{N-1} j\left(P_{i,j}\right) \tag{3.39}$$

Mean based on the reference pixel and neighbour pixels are defined by the equations respectively.

Variance:

$$\sigma_i^2 = \sum_{i,j=0}^{N-1} P_{i,j}\left(i-\mu_i\right)^2, \sigma_j^2 = \sum_{i,j=0}^{N-1} P_{i,j}\left(i-\mu_j\right)^2 \tag{3.40}$$

The following equations define the features.

Correlation:

$$\sum_{i,j=0}^{N-1} P_{i,j}\left[\frac{\left(i-\mu_i\right)\left(i-\mu_j\right)}{\sqrt{\left(\sigma_i\right)^2\left(\sigma_j\right)^2}}\right] \tag{3.41}$$

Contrast:

$$\sum_{i,j=0}^{N-1} P_{i,j}\left(i-j\right)^2 \tag{3.42}$$

when i and j are 0, the values represent pixels similar to neighbour. If i and j differ by 1, then there is a small contrast. If they differ by 2, then contrast is higher.

Dissimilarity:

$$\sum_{i,j=0}^{N-1} P_{i,j} \left|i-j\right| \tag{3.43}$$

In dissimilarity, weights increase linearly as one moves from diagonal.

Homogeneity:

$$\sum_{i,j=0}^{N-1} \frac{P_{i,j}}{1+(i-j)^2} \tag{3.44}$$

Homogeneity weights values by the universe of the contrast weight.

Angular Second Moment(ASM):

$$\sum_{i,j=0}^{N-1} {P_{i,j}}^2 \tag{3.45}$$

ASM and energy use each P value as weight. When the window is very orderly, high values of ASM and energy occur.

Energy:

$$Energy = \sqrt{ASM} \tag{3.46}$$

Entropy:

$$\sum_{i,j=0}^{N-1} P_{i,j} \left(-lnP_{i,j}\right) \tag{3.47}$$

We used these features in our study because these features showed some correlation with other features in researches [21, 57].

3.4 Micro-CT Imaging Protocol

3.4.1 Imaging Settings

We had 15 samples. A SkyScan 1172 (Kontich, Belgium) x-ray microtomograph was used to scan these samples. The voxel size was 26 μm. As described in Britz et al. 2010 [12], the samples were rotated through 180° at rotation steps of 0.35°. The x-ray settings were standardized to 100 kV and 100 μA. The setting had an exposure time of 65 ms per frame. In order to minimize the beam-hardening artifacts, a aluminum-copper filter and a beam-hardening correction algorithm were applied. The number of connected scans were 4. So, the scan time for each sample was approximately 1h 30 m (22 m 30 s for each scan). A 3D median filter with a 3×3×3 cubic kernel was applied in the images in order to reduce image noise. CT Analyzer 1.9.1.0 (SkyScan, Kontich, Belgium) was used to analyze the images. Figure 3.15 shows three-dimensional volume rendering of a sample with orthogonal and oblique projection and a cutaway. Figure 3.16 shows three dimensional rendering of slices from orthogonal and oblique sections.

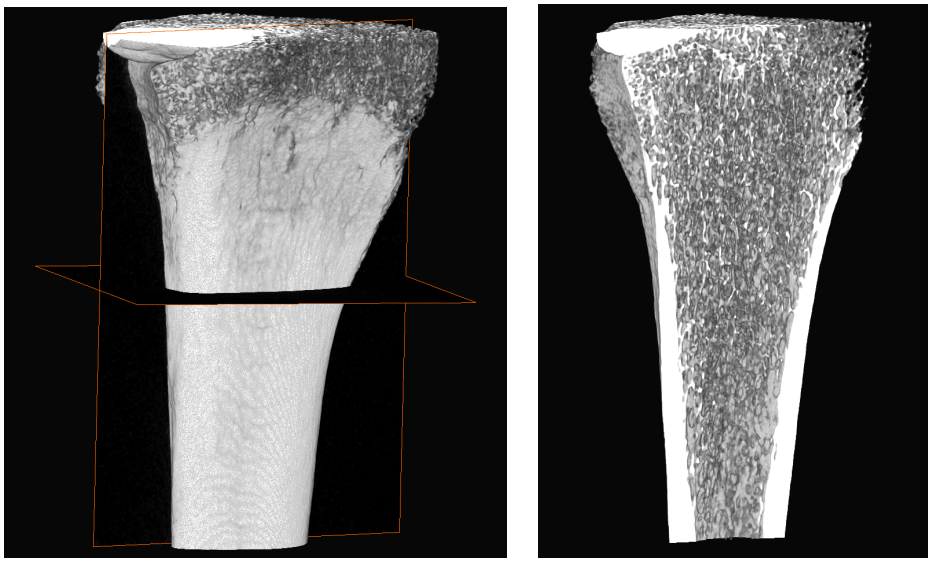

(a) Three-dimensional volume rendering **(b)** Oblique cutaway

Figure 3.15: Three-dimensional volume rendering of a sample and a oblique cutaway.

3.4.2 Trabecular Analysis

Three volumes of interest (VOI) were selected. These VOIs were denoised with gaussian smoothing with radius, $r = 1$. We used standard user defined threshold for the binarization of the VOIs (8-bit to 1-bit). As these VOIs have cortical bone, a segmentation process was carried out to extract the trabecular bone region. An interactive manual segmentation was used to segment trabecular bone region from cortical bone region. Figure 3.17 shows selection of three volumes of interest. Figure 3.18 shows segmentation of trabecular bone region from cortical bone region. These VOIs were then used to extract the trabecular properties.

3.4.3 Morphological trabecular properties

In the assessment of osteoporosis, bone mineral density (BMD) and trabecular properties are the two main factors to be measured. Trabecular properties characterizes the structure of bone. It is used to measure the bone strength. So, these properties can provide more accuracy in the assessment as researches showed. Previous researches mentioned in the second chapter showed that texture features of bone images have correlation with BMD and trabecular properties of bone. In this thesis, we determined the correlation between texture features and trabecular properties. Micro-CT trabecular parameters were calculated by $SkyScan^{TM}$ CT-Analyzer software [40]. Using both 2D and 3D, some parameters are measured. Details of these parameters are given below. All the measurement is done as μm units.

Bone Volume (BV): The 3D volume measurement is the number of voxels of binarised bone in the volume of interest (VOI) times the voxel volume [40] based on the hexahedral volume model. It is given in μm^3

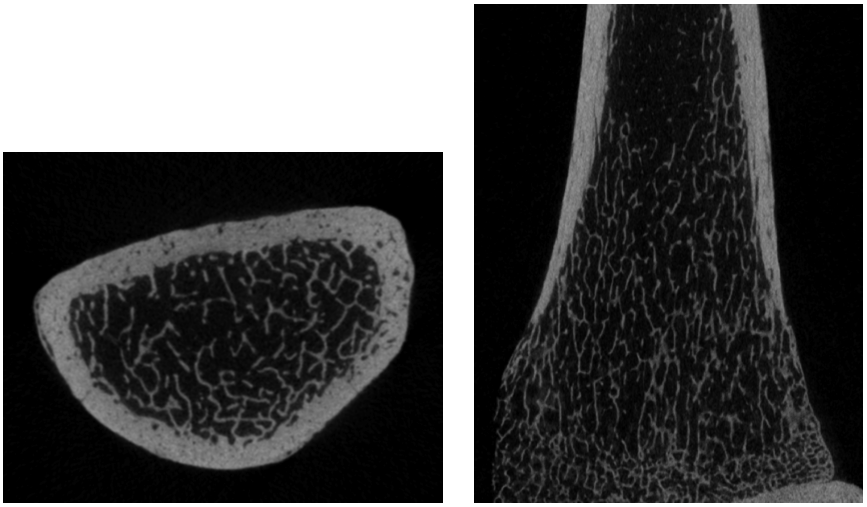

(a) Orthogonal slice **(b)** Oblique slice

Figure 3.16: Three-dimesional rendering of slices from orthogonal and oblique sections.

units.

Tissue Volume (TV): The 3D volume measurement is the number of voxels of binarised bone in the volume of interest (VOI) times the voxel volume [40] based on the hexahedral volume model. It is given in μm^3 units.

Percent bone volume (BV/TV): In order to measure trabecular bone only, this parameter is used. The proportion of the VOI occupied by binarised trabecular bone. In our study it excludes any cortical bone region. It is given in %.

Bone Surface (BS): In 3D measurement, BS is based on a simple cubic voxel. It uses the faceted surface to measure the feature. It is given in μm^2 units.

Bone surface density (BS/TV): In 3D measurement, BS/TV calculates the ratio of surface area to total volume measured within the VOI. It is given in μm^{-1} units.

Trabecular Thickness (Tb.Th): 3D micro-CT applies a model-independent analysis which calculates the average of the local thickness at each voxel representing bone. It is given in μm units.

Trabecular Seperation (Tb.Sp): Using the same method used to measure trabecular thickness, $SkyScan^{TM}$ CT-Analyzer software can calculate trabecular seperation model-independently in 3D from micro-CT images. It is given in μm units.

Trabecular Number (Tb.N): Trabecular number describes the number of traversals in per unit length in the trabecular bone region using a direct 3D thickness measurement. It is given in μm^{-1} unit.

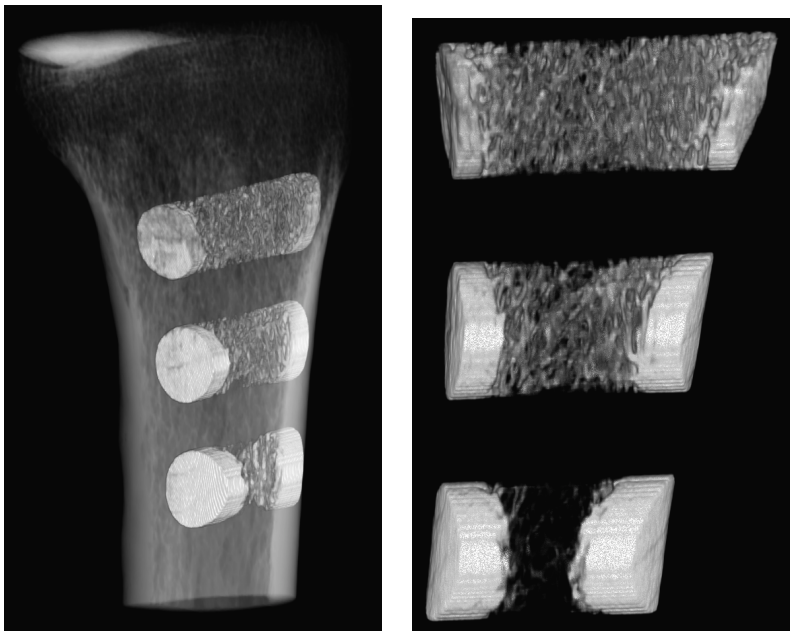

Figure 3.17: Selection of volumes of interest (VOIs).

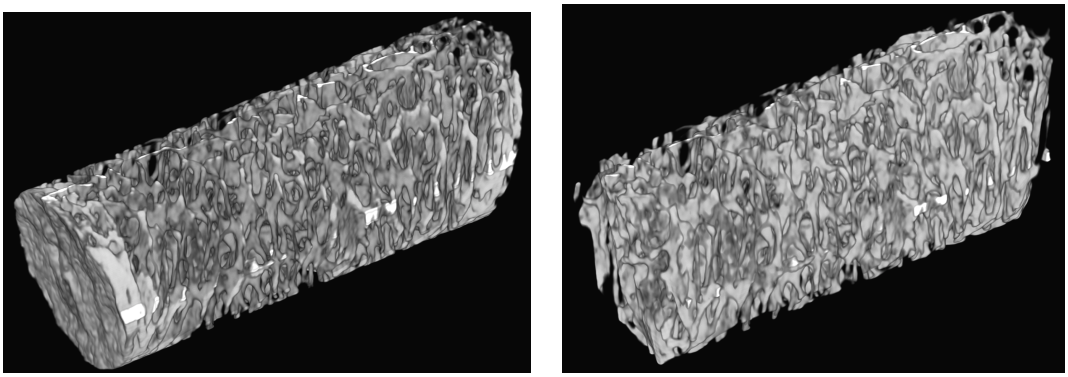

(a) VOI with cortical bone region **(b)** VOI without cortical bone region

Figure 3.18: Segmentation of trabecular bone region from cortical bone region.

Chapter 4

Experiments

4.1 Experiment on Images at 0.5 Point On the Rocking Curve

4.1.1 Experiment Settings

We discussed the materials for this experiment in the previous chapter. Among the different sets of images, we selected images at 0.5 on the rocking curve for horizontal and vertical orientations. Images were down sampled to 50% of their original size (40 μ m pixel size), although different down sampled images were tested (Data shown in Appendices A, B ,C, and D). Images down sampled to 50% of their original size have performed better.

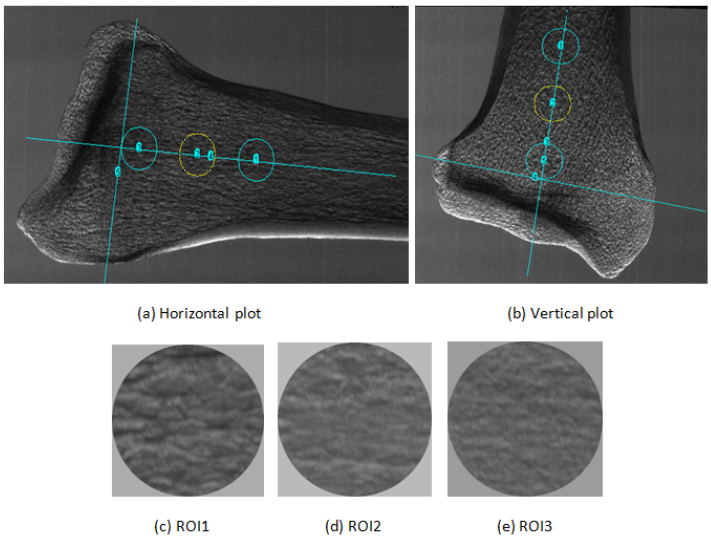

Figure 4.1: Selection of ROIs from vertical oriented images.

We placed a line in the horizontal images along the long axis and a line perpendicular to it along the edges of growth plate of the distal bone. The same procedure was done for the vertical images. The first 120-pixel radius ROI was centered on the long axis and placed just against the perpendicular line. The remaining ROIs were spaced centered along the long axis with centers 330-pixels apart. Finally, three regions of interests - distal (d) denoted as ROI1, medial (m) denoted as ROI2, and proximal (p) denoted as ROI3 within the bone

images were extracted. Figure 4.1 shows the selection of ROIs in the images. These ROI images are 241 × 241-pixels grayscale images. Texture methods were applied on these images. The bones are potentially of different length and thus the ROIs might not be selecting exactly comparable regions within each sample, but the bones were of similar enough length that any confounding effects from this should not be too great. In order to avoid any confounding effects, we selected the ROIs for a fixed distance and in this way this process will help us selecting comparable ROIs within samples and this fixed-distance measurement will be able to adjust the ROIs within images in both horizontal and vertical orientations.

4.1.2 Why 0.5 on the rocking curve

We tested the collected images at all the points on the rocking curve. We tested high angle images (+0.5, +0.25, +0.125 points on the rocking curve), low angle images (-0.5, -0.25, -0.125 points on the rocking curve), and images at top point on the rocking curve. We presented only results of images at 0.5 on the rocking curve and their DEI images as they have showed stronger correlations with 3D bone parameters than images at other points on the rocking curve. Therefore, our results, discussion, and conclusion chapters may have selection bias. However, we have included the results of images at other points on the rocking curve in Appendices A, B, C, and D.

We determined the correlation of texture features between high and low angle images at 0.5 on the rocking curve. Table 4.1, 4.2, and 4.3 show the correlation of features between high and low angle images for GLCM, TFCM, and FD methods respectively. Figure 4.2 shows the correlation between the high and low angle images graphically. We found that they are highly correlated. That is why we only selected images of high angle and DEI images to show the results in detail. The results are described in the following section. We used both individual ROI and pooled results (r^2) of all the three ROIs in the graphs throughout this chapter. We discussed the individual ROI results in the next chapter.

Table 4.1: Correlation (r^2) between GLCM parameters for high and low angle images. r^2 values are pooled values.

High Angle	Low Angle			
	Contrast	Correlation	Energy	Homogeneity
Contrast	0.94	0.77	0.89	0.76
Correlation	0.73	0.93	0.82	0.75
Energy	0.80	0.81	0.95	0.78
Homogeneity	0.84	0.82	0.74	0.91

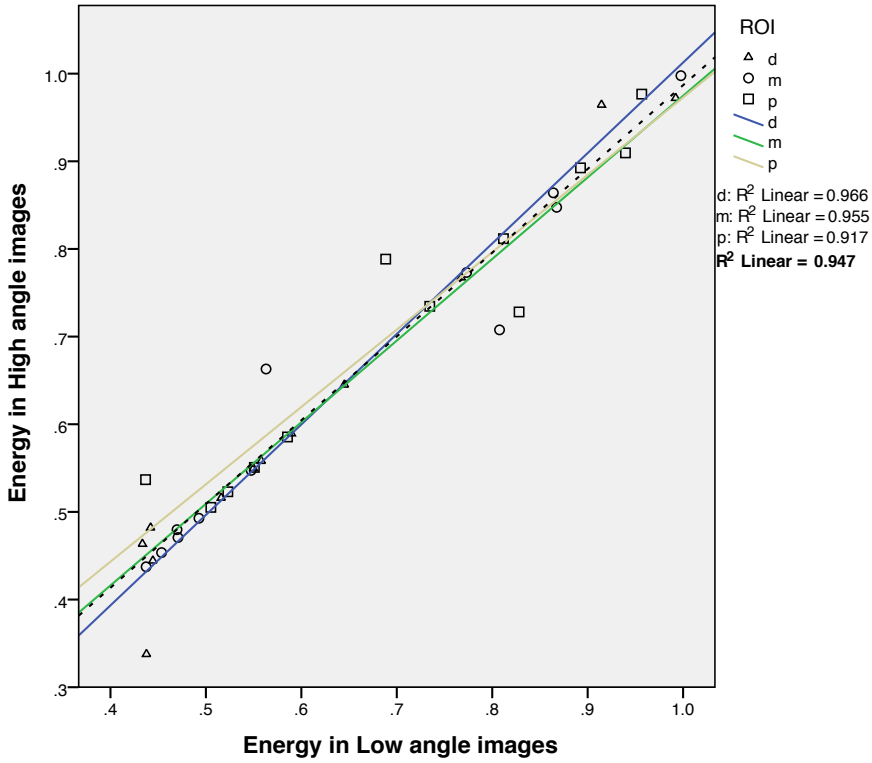

(a) Graph for energy feature of images at 0.5 for high and low angles

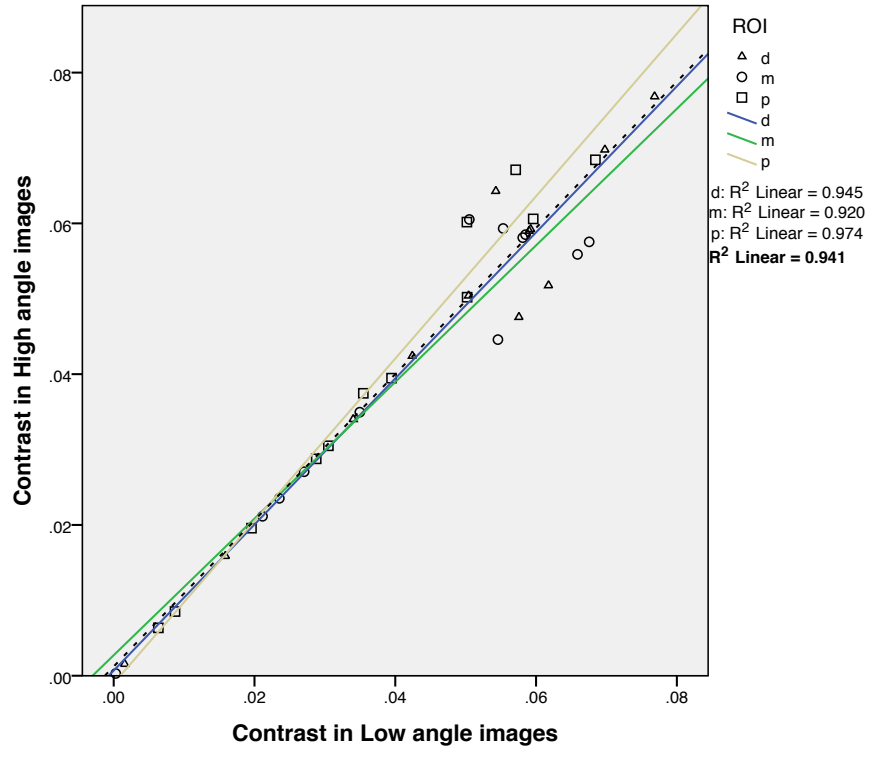

(b) Graph for contrast feature of images at 0.5 for high and low angles

Figure 4.2: Correlations between high and low angle images. ROIs: distal (d), medial (m), and proximal (p). Bolded r^2 for pooled results.

Table 4.2: Correlation (r^2) between TFCM parameters for high and low angle images. r^2 values are pooled values.

High Angle	Low Angle				
	Coarseness	Homogeneity	Mean Convergence	Variance	Code Entropy
Coarseness	0.91	0.78	0.88	0.79	0.81
Homogeneity	0.73	0.93	0.82	0.79	0.76
Mean Convergence	0.78	0.84	0.90	0.87	0.79
Variance	0.84	0.81	0.81	0.89	0.79
Code Entropy	0.86	0.81	0.86	0.89	0.94

Table 4.3: Correlation (r^2) between fractal parameters for high and low angle images. r^2 values are pooled values.

High Angle	Low Angle	
	Fractal Dimension (FD)	Lacunarity
Fractal Dimension (FD)	0.93	0.89
Lacunarity	0.87	0.92

4.2 GLCM Results

4.2.1 Horizontal Orientation

Table E.16 illustrates the best fitting coefficients (pooled ROI results) of correlation between GLCM features and the morphological parameters for images of high angle side on the rocking curve. A linear correlation was found with several morphological parameters (Energy/Tb.N: $r^2 = 0.36, p < 0.01$, Energy/ BS/BV: $r^2 = 0.35, p < 0.01$, Energy/ BV/TV: $r^2 = 0.36, p < 0.01$). The coefficient of correlation was highest between energy and BV/TV for all sets of images. Figure 4.3(a) shows the linear relationships between energy and BS/BV. Figure 4.4(a) shows the linear relationships between energy and BV/TV. Figure 4.5(a) shows the linear relationships between energy and Tb.N.

Table 4.5 shows the best fitting coefficients (pooled ROI results) of correlation between GLCM features and the morphological parameters for DEI images at point 0.5 of the rocking curve. Linear correlations were observed with several morphological parameters (Energy/Tb.N: $r^2 = 0.37, p < 0.01$, Energy/ BS/BV: $r^2 = 0.36, p < 0.01$, Energy/ BV/TV: $r^2 = 0.37, p < 0.01$). The results for this set of images were stronger than the images at high angle. Figure 4.3(c) shows the linear relationships between energy and BS/BV. Figure 4.4(b) shows the linear relationships between energy and BV/TV. The coefficient of correlations of

Table 4.4: Correlation between GLCM and architectural parameters for horizontal images of high angle on the rocking curve. r^2 values are pooled values.

	r^2	Best Fit Model	Best Feature	p
Bone Volume (BV)	0.28	Linear	Contrast	< 0.01
Percent Bone Volume (BV/TV)	0.36	Linear	Energy	< 0.01
Bone Surface by Volume Ratio (BS/BV)	0.35	Linear	Energy	< 0.01
Bone Surface (BS)	0.26	Linear	Energy	< 0.01
Trabecular Number (Tb.N)	0.36	Linear	Energy	< 0.01

Table 4.5: Correlation between GLCM and architectural parameters for horizontal DEI images. r^2 values are pooled values.

	r^2	Best Fit Model	Best Feature	p
Bone Volume (BV)	0.29	Linear	Contrast	< 0.01
Percent Bone Volume (BV/TV)	0.37	Linear	Energy	< 0.01
Bone Surface by Volume Ratio (BS/BV)	0.36	Linear	Energy	< 0.01
Bone Surface (BS)	0.25	Linear	Energy	< 0.01
Trabecular Number (Tb.N)	0.37	Linear	Energy	< 0.01

DEI images showed stronger results than high angle images. Figure 4.5(b) shows the linear relationships between energy and Tb.N.

4.2.2 Vertical Orientation

Table 4.6 illustrates the best fitting coefficients (pooled ROI results) of correlation between GLCM features and the morphological parameters for images of high angle side on the rocking curve. A linear correlation was found with several morphological parameters (Energy/Tb.N: $r^2 = 0.37, p < 0.01$, Energy/ BS/BV: $r^2 = 0.39, p < 0.01$, Energy/ BV/TV: $r^2 = 0.37, p < 0.01$). The coefficient of correlation was highest between energy and BV/TV for all sets of images. Figure 4.6(a) shows the linear relationships between energy and BS/BV. Figure 4.7(a) shows the linear relationships between energy and BV/TV. Figure 4.8(a) shows the linear relationships between energy and Tb.N.

Table 4.7 shows the best fitting coefficients (pooled ROI results) of correlation between GLCM features and the morphological parameters for DEI images at point 0.5 of the rocking curve. Linear correlations were observed with several morphological parameters (Energy/Tb.N: $r^2 = 0.37, p < 0.01$, Energy/ BS/BV: $r^2 = 0.39, p < 0.01$, Energy/ BV/TV: $r^2 = 0.38, p < 0.01$). The results for this set of images were stronger

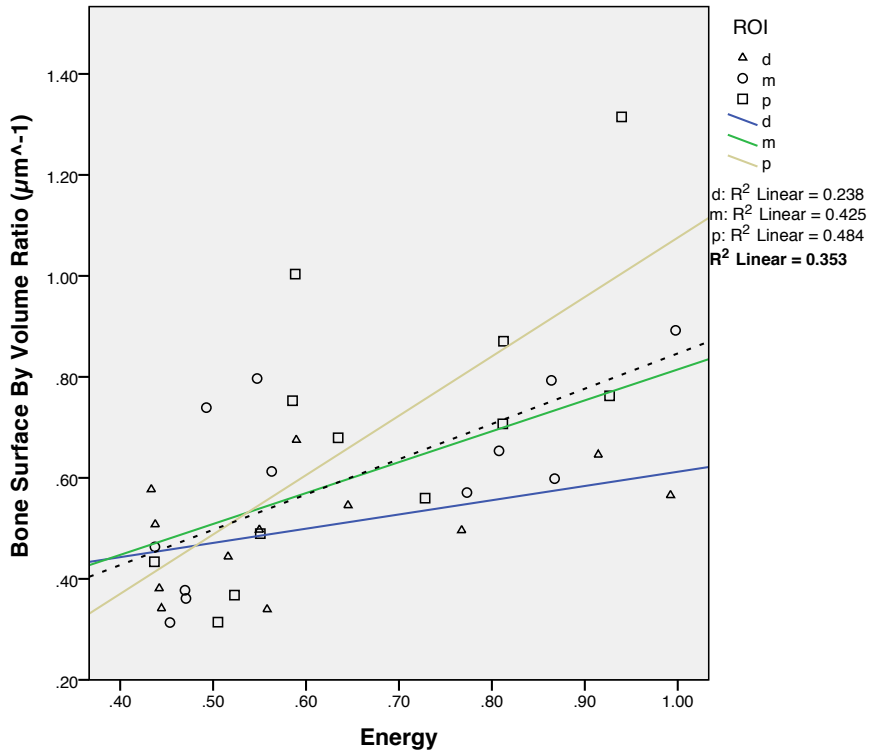

(a) Graph for high angle images

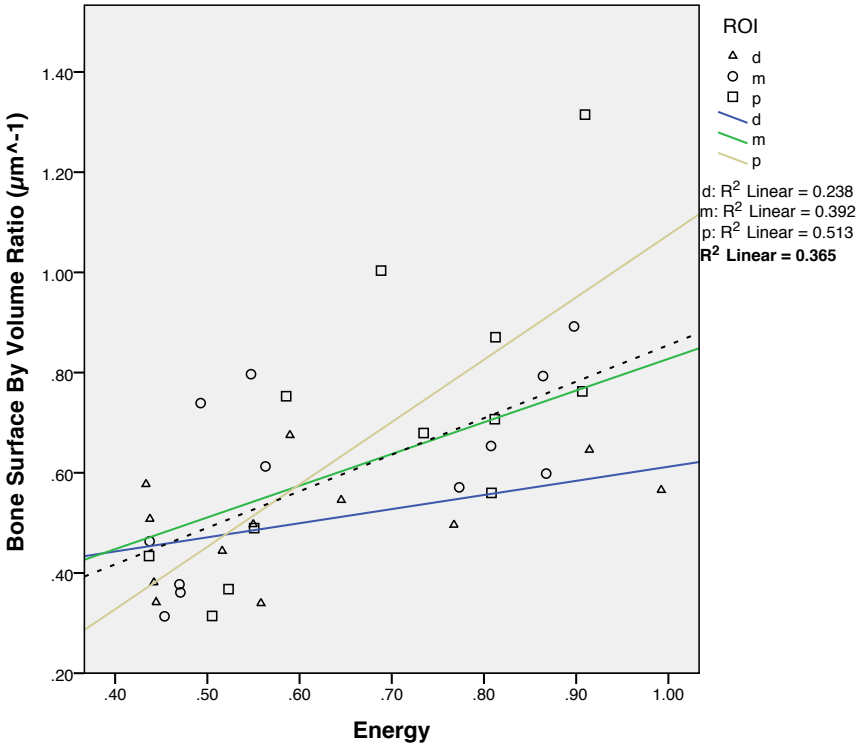

(b) Graph for DEI images

Figure 4.3: Linear relationships between energy and bone surface by volume ratio for horizontal images. ROIs: distal (d), medial (m), and proximal (p). Bolded r^2 for pooled results.

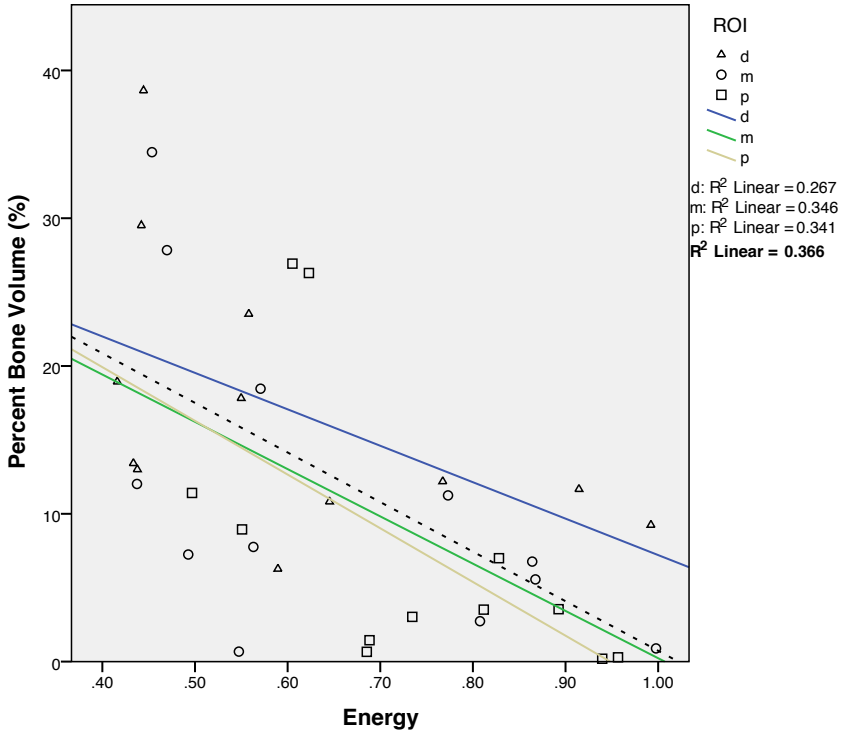

(a) Graph for high angle images

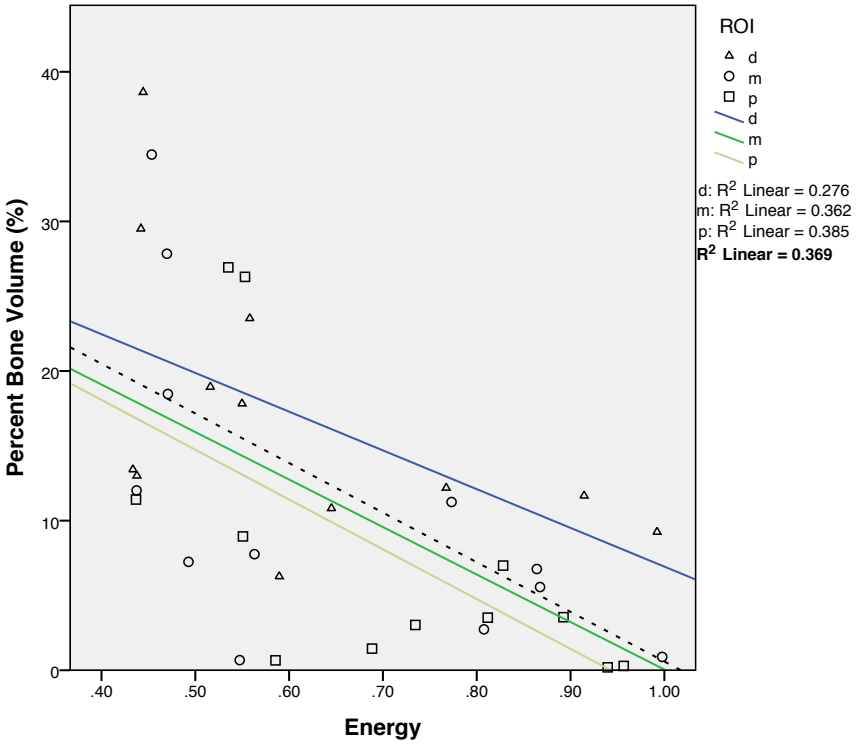

(b) Graph for DEI images

Figure 4.4: Linear relationships between energy and percent bone volume for horizontal images. ROIs: distal (d), medial (m), and proximal (p). Bolded r^2 for pooled results.

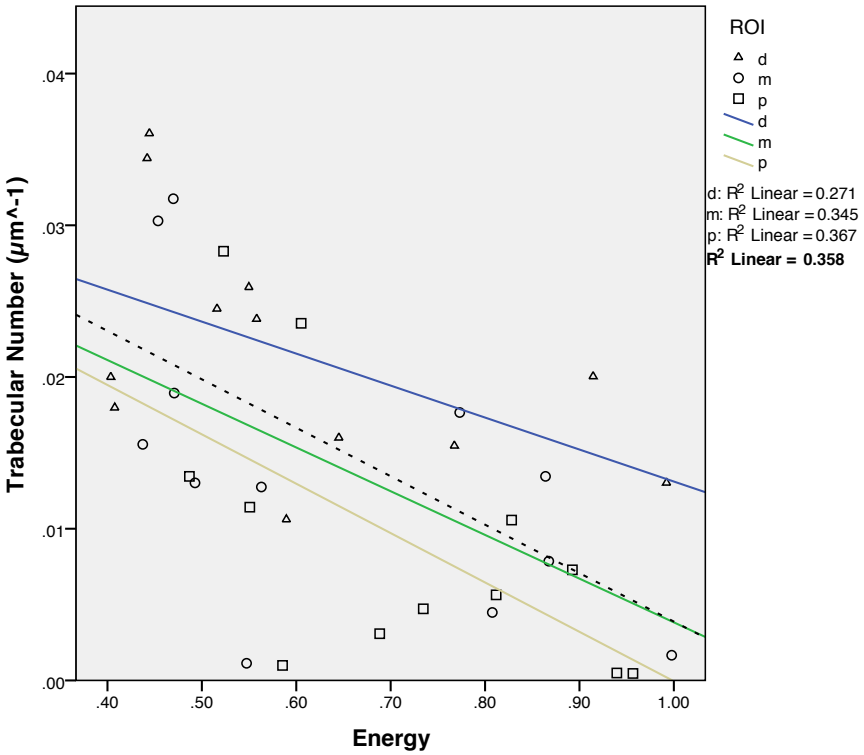

(a) Graph for high angle images

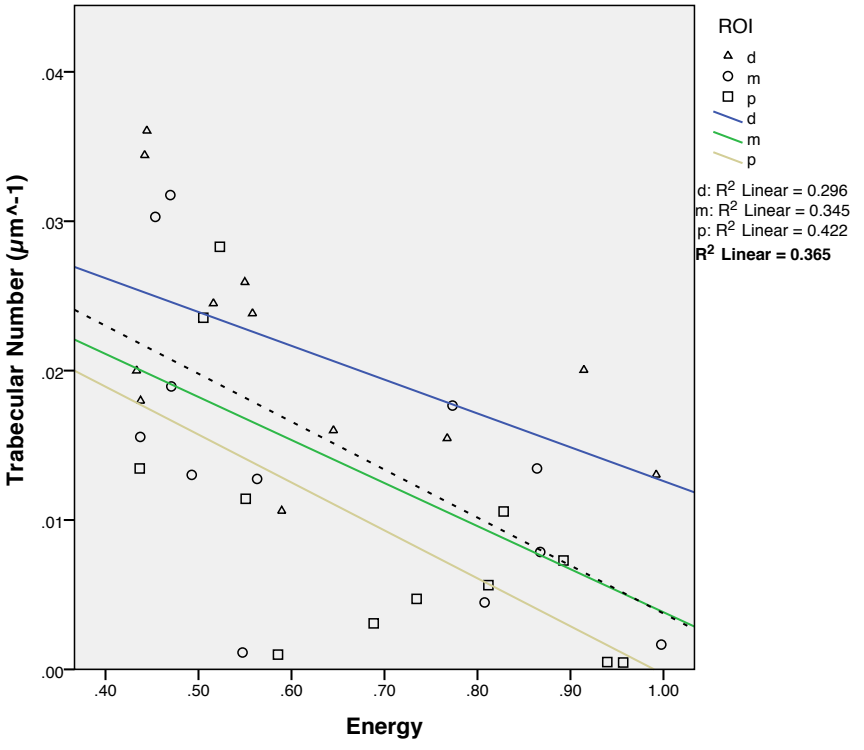

(b) Graph for DEI images

Figure 4.5: Linear relationships between energy and trabecular number for horizontal images. ROIs: distal (d), medial (m), and proximal (p). Bolded r^2 for pooled results.

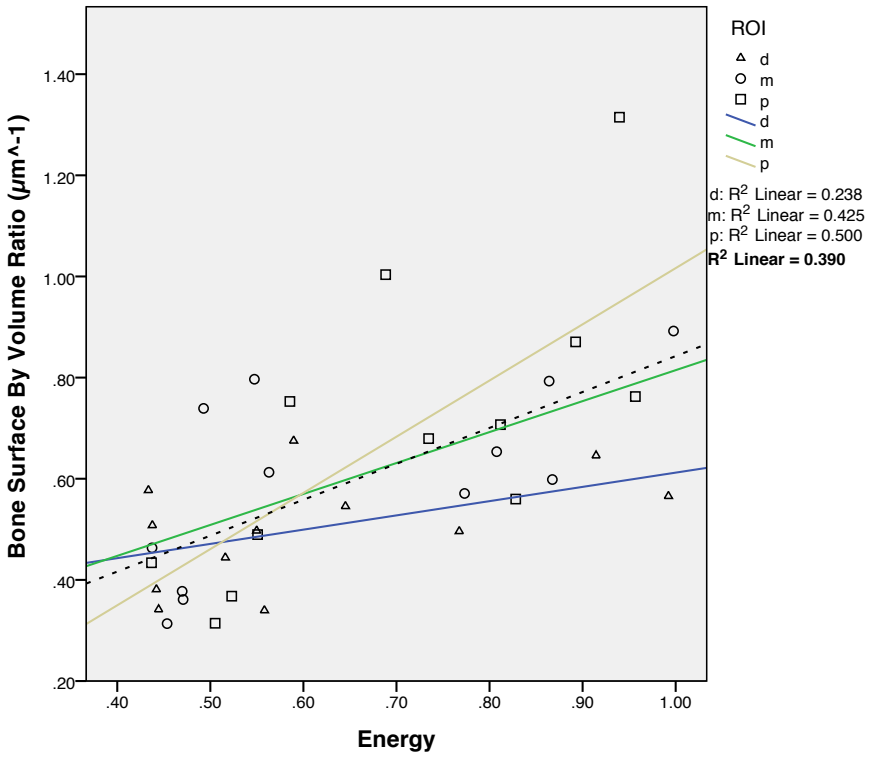

(a) Graph for high angle images

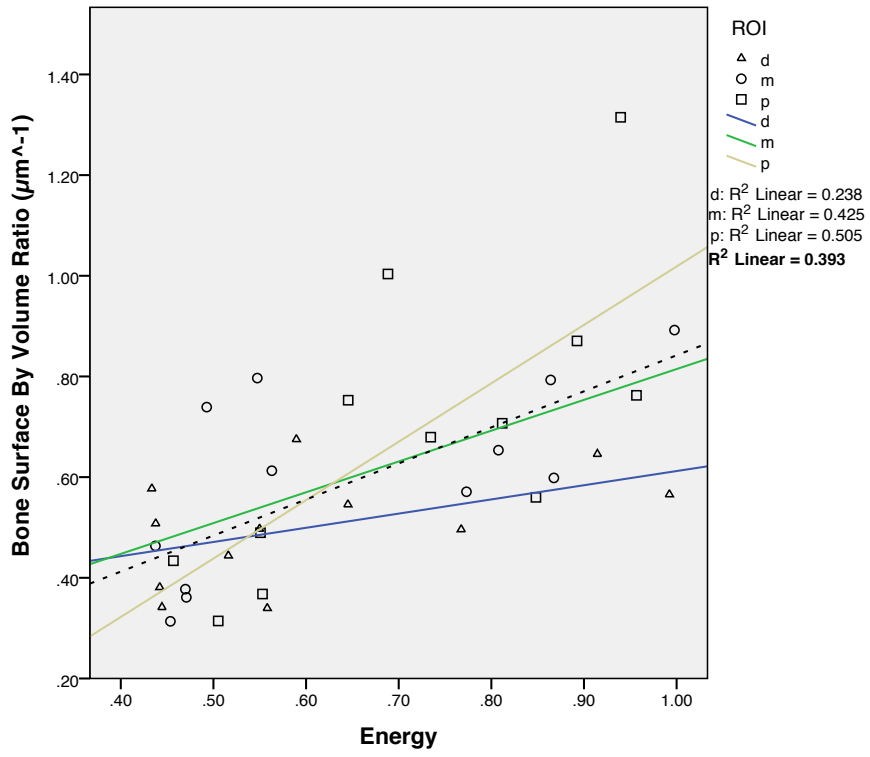

(b) Graph for DEI images

Figure 4.6: Linear relationships between energy and bone surface by volume ratio for vertical images. ROIs: distal (d), medial (m), and proximal (p). Bolded r^2 for pooled results.

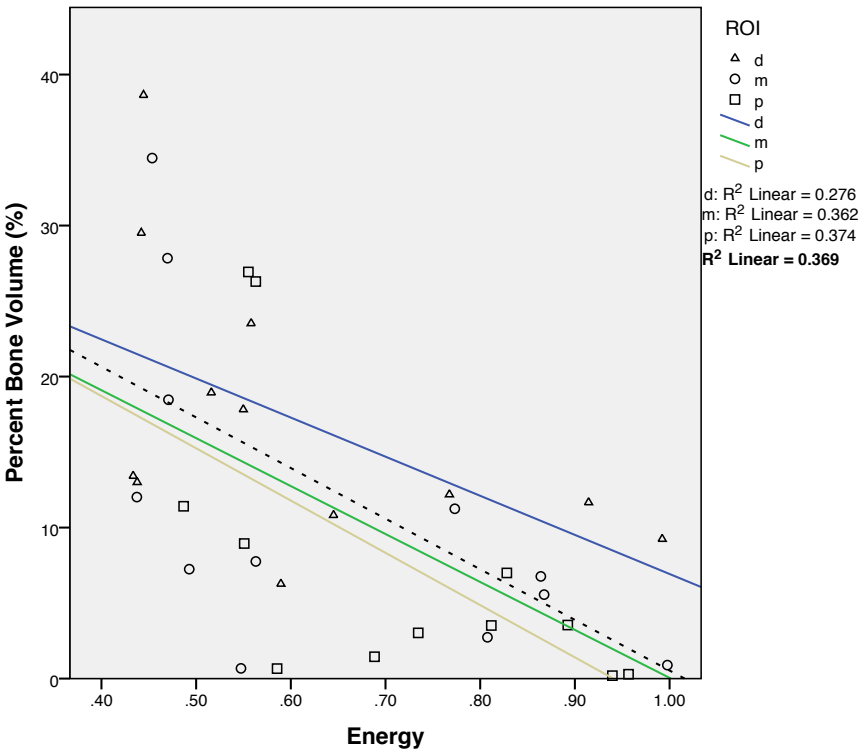

(a) Graph for high angle images

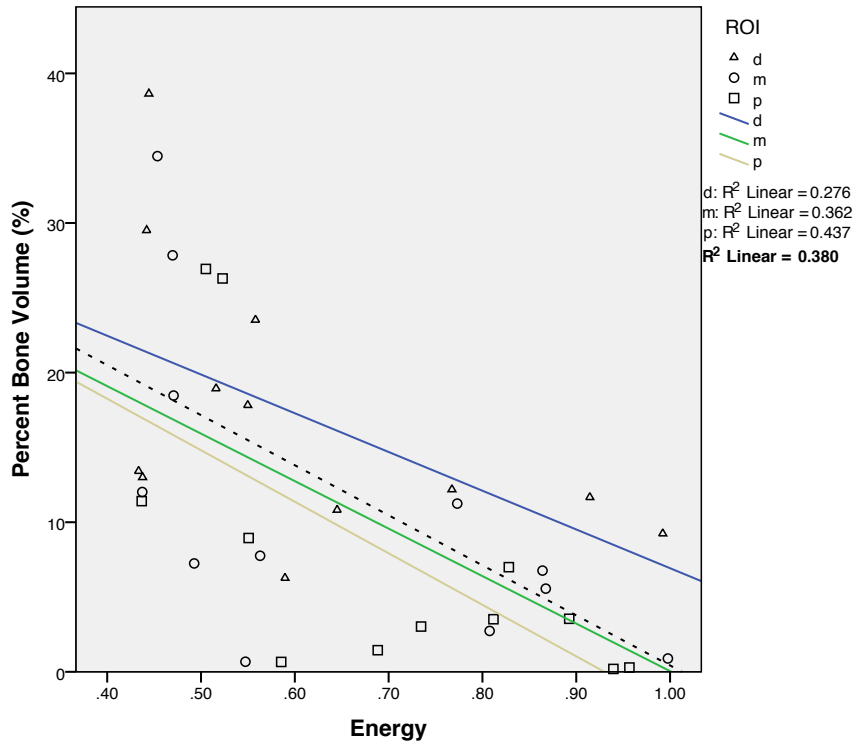

(b) Graph for DEI images

Figure 4.7: Linear relationships between energy and percent bone volume for vertical images. ROIs: distal (d), medial (m), and proximal (p). Bolded r^2 for pooled results.

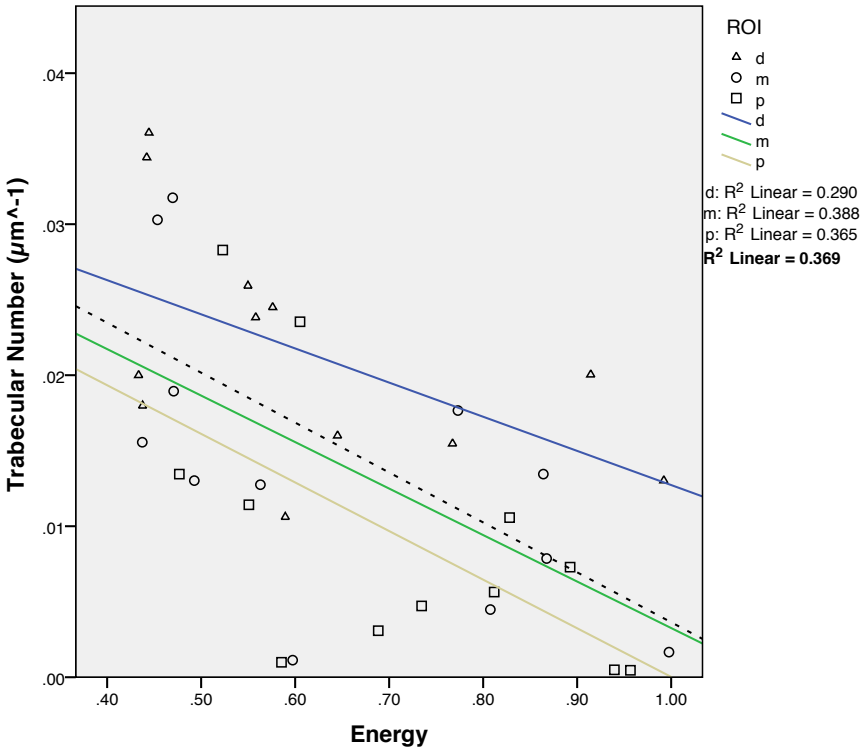

(a) Graph for high angle images

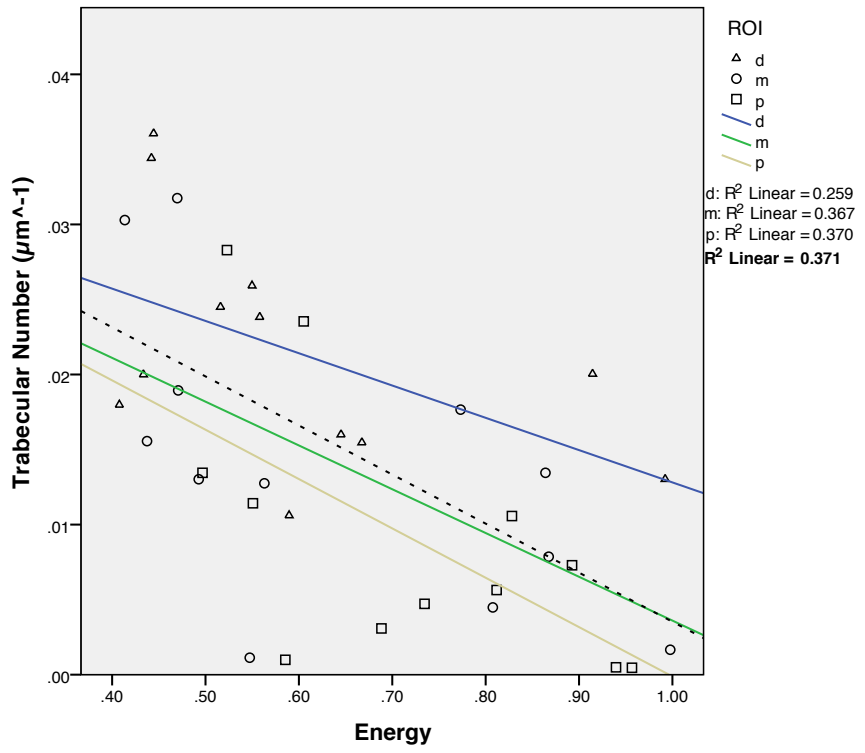

(b) Graph for DEI images

Figure 4.8: Linear relationships between energy and trabecular number for vertical images. ROIs: distal (d), medial (m), and proximal (p). Bolded r^2 for pooled results.

Table 4.6: Correlation between GLCM and architectural parameters for vertical images of high angle on the rocking curve. r^2 values are pooled values.

	r^2	Best Fit Model	Best Feature	p
Bone Volume (BV)	0.31	Linear	Contrast	< 0.01
Percent Bone Volume (BV/TV)	0.37	Linear	Energy	< 0.01
Bone Surface by Volume Ratio (BS/BV)	0.39	Linear	Energy	< 0.01
Bone Surface (BS)	0.29	Linear	Energy	< 0.01
Trabecular Number (Tb.N)	0.37	Linear	Energy	< 0.01

Table 4.7: Correlation between GLCM and architectural parameters for vertical DEI images. r^2 values are pooled values.

	r^2	Best Fit Model	Best Feature	p
Bone Volume (BV)	0.29	Linear	Contrast	< 0.01
Percent Bone Volume (BV/TV)	0.38	Linear	Energy	< 0.01
Bone Surface by Volume Ratio (BS/BV)	0.39	Linear	Energy	< 0.01
Bone Surface (BS)	0.30	Linear	Energy	< 0.01
Trabecular Number (Tb.N)	0.37	Linear	Energy	< 0.01

than the images at high angle. Figure 4.6(c) shows the linear relationships between energy and BS/BV. Figure 4.7(b) shows the linear relationships between energy and BV/TV. The coefficient of correlations of DEI images showed the best results. Figure 4.8(b) shows the linear relationships between energy and Tb.N.

Linear relationships were found between energy and architectural parameters. For all the sets of images, energy has displayed stronger linear relationships with architectural parameters than other features. We can observe there is a linear change throughout the three regions of interests. DEI images have shown stronger results than high angle images for both horizontal and vertical orientations.

4.3 TFCM Results

4.3.1 Horizontal Orientation

Table 4.8 illustrates the best fitting coefficients (pooled ROI results) of correlation between TFCM features and the morphological parameters for images of high angle side on the rocking curve. A linear correlation was found with several morphological parameters (Homogeneity/BS: $r^2 = 0.35, p < 0.01$, Mean convergence/BS: $r^2 = 0.16, p < 0.01$). Figure 4.9(a) shows the linear relationships between homogeneity and BS. The coefficient

of correlation was highest between homogeneity and BS for this sets of images. Figure 4.10(a) shows the linear relationships between mean convergence and BS.

Table 4.8: Correlation between TFCM and architectural parameters for horizontal images of high angle on the rocking curve. r^2 values are pooled values.

	r^2	Best Fit Model	Best Feature	p
Bone Volume (BV)	0.25	Linear	Homogeneity	< 0.01
Percent Bone Volume (BV/TV)	0.23	Linear	Mean convergence	< 0.01
Bone Surface (BS)	0.35	Linear	Homogeneity	< 0.01
Trabecular Number (Tb.N)	0.27	Linear	Homogeneity	< 0.01

Table 4.9 shows the best fitting coefficients (pooled ROI results) of correlation between TFCM features and the morphological parameters for DEI images at point 0.5 of the rocking curve. Linear correlations were observed with several morphological parameters (Homogeneity /BS: $r^2 = 0.39, p < 0.01$, Mean convergence/BS: $r^2 = 0.17, p < 0.01$). The results for this set of images were stronger than the images at high angle. Figure 4.9(b) shows the linear relationships between homogeneity and BS. Figure 4.10(b) shows the linear relationships between mean convergence and BS. The coefficient of correlations of DEI images showed the best results.

4.3.2 Vertical Orientation

Table 4.10 illustrates the best fitting coefficients (pooled ROI results) of correlation between TFCM features and the morphological parameters for images of high angle side on the rocking curve. A linear correlation was found with several morphological parameters (Homogeneity/BS: $r^2 = 0.36, p < 0.01$, Mean convergence/BS: $r^2 = 0.17, p < 0.01$). Figure 4.11(a) shows the linear relationships between homogeneity and BS. The coefficient of correlation was highest between homogeneity and BS for this set of images. Figure 4.12(a) shows the linear relationships between mean convergence and BS.

Table 4.9: Correlation between TFCM and architectural parameters for horizontal DEI images. r^2 values are pooled values.

	r^2	Best Fit Model	Best Feature	p
Bone Volume (BV)	0.26	Linear	Homogeneity	< 0.01
Percent Bone Volume (BV/TV)	0.24	Linear	Mean convergence	< 0.01
Bone Surface (BS)	0.39	Linear	Homogeneity	< 0.01
Trabecular Number (Tb.N)	0.28	Linear	Homogeneity	< 0.01

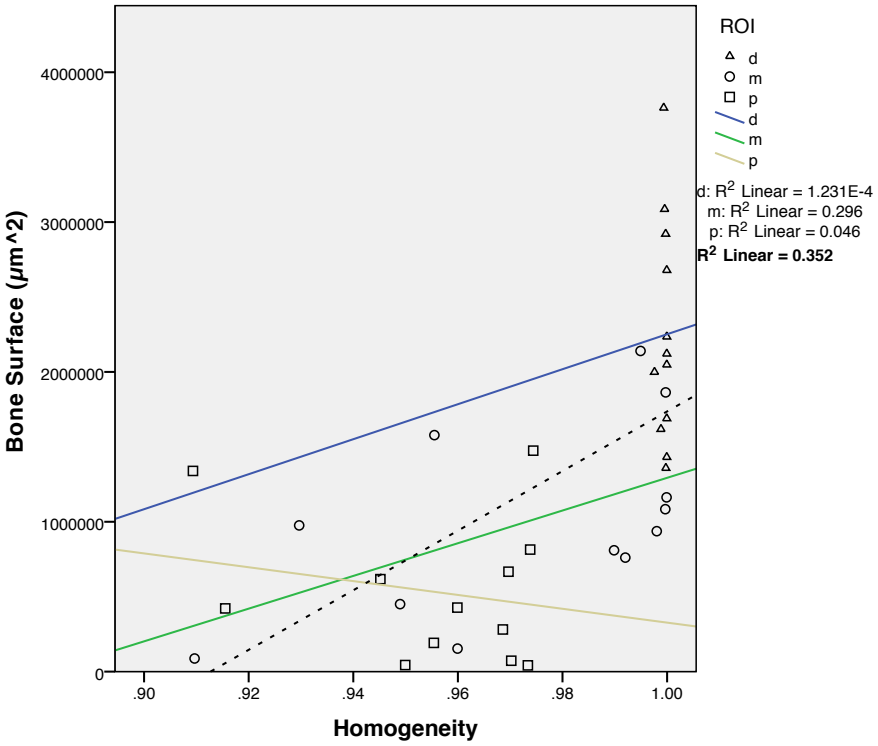

(a) Graph for DEI images

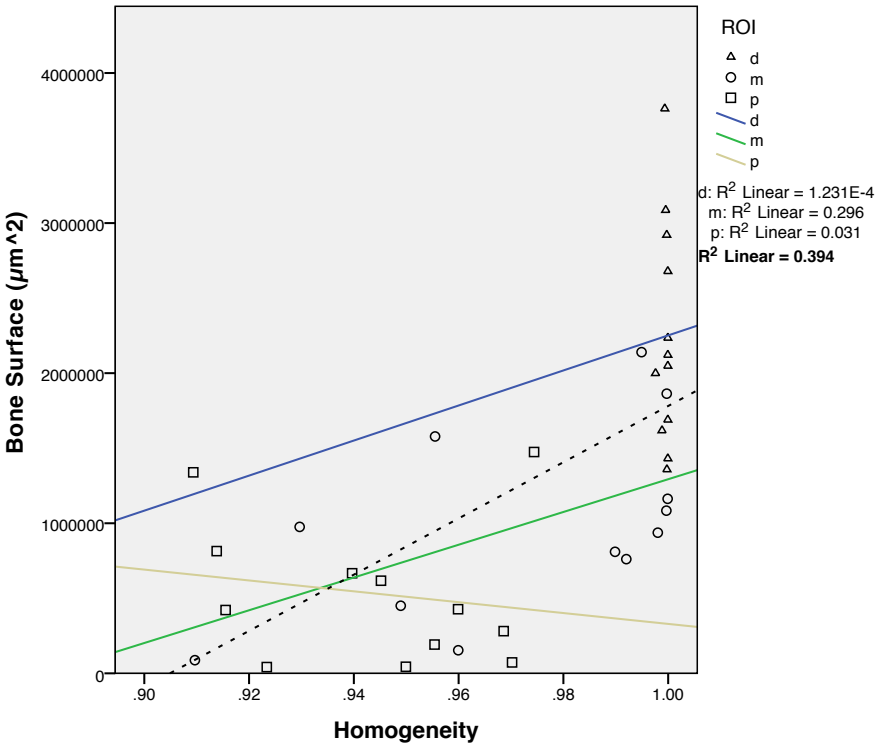

(b) Graph for high angle images

Figure 4.9: Linear relationships between homogeneity and bone surface for horizontal images. ROIs: distal (d), medial (m), and proximal (p). Bolded r^2 for pooled results.

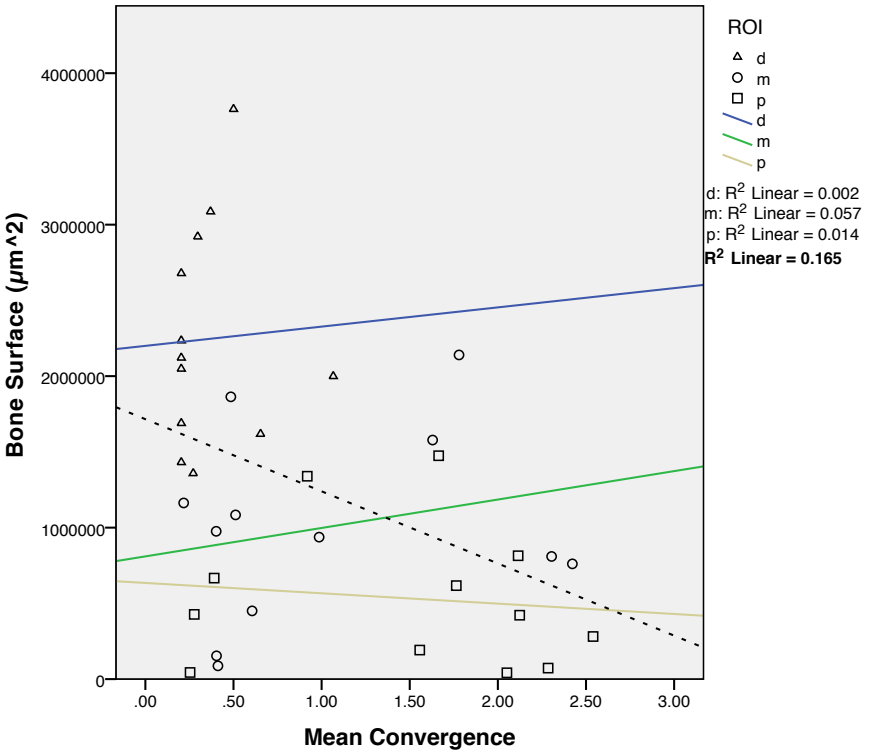

(a) Graph for high angle images

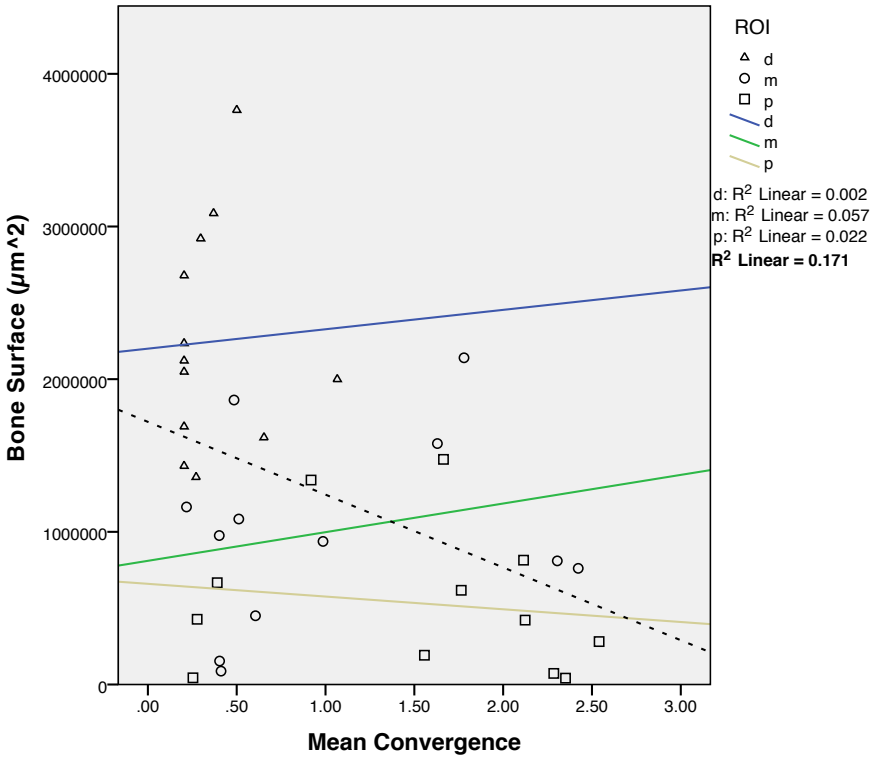

(b) Graph for DEI images

Figure 4.10: Linear relationships between mean convergence and bone surface for horizontal images. ROIs: distal (d), medial (m), and proximal (p). Bolded r^2 for pooled results.

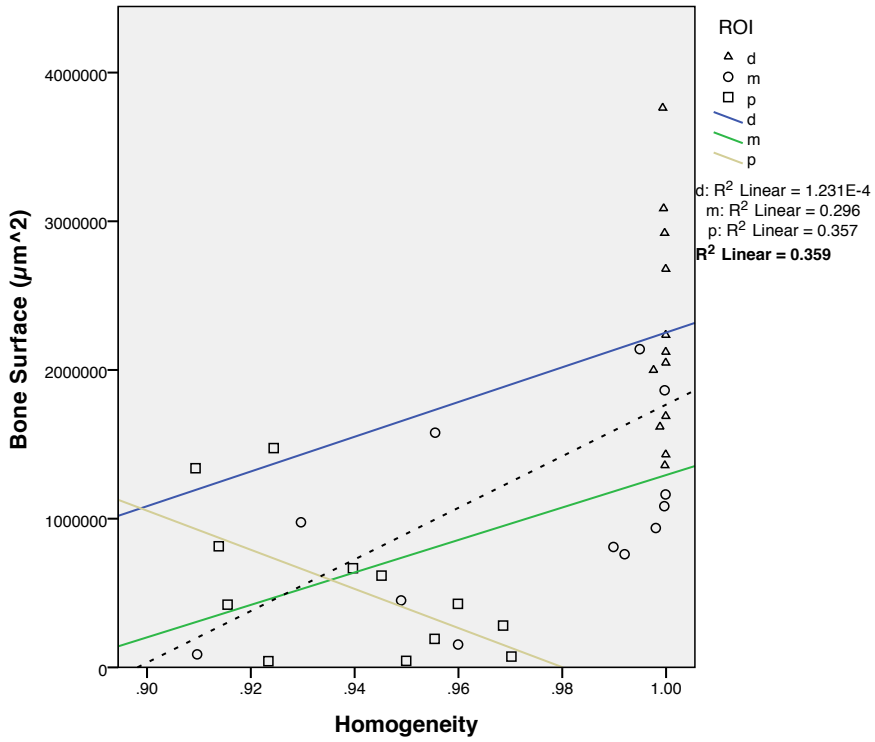

(a) Graph for high angle images

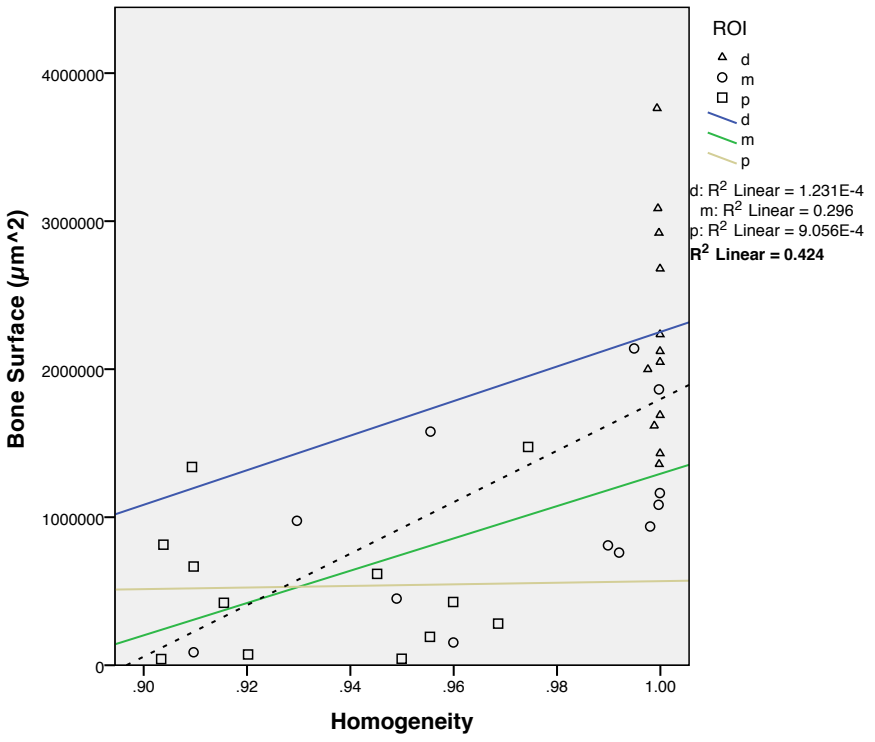

(b) Graph for DEI images

Figure 4.11: Linear relationships between homogeneity and bone surface for vertical images. ROIs: distal (d), medial (m), and proximal (p). Bolded r^2 for pooled results.

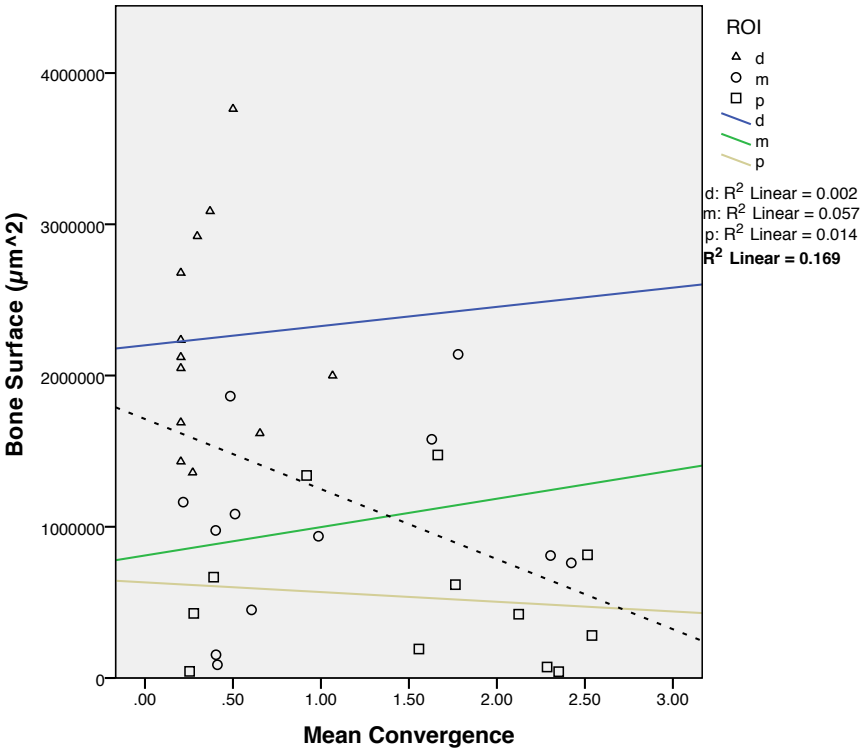

(a) Graph for high angle images

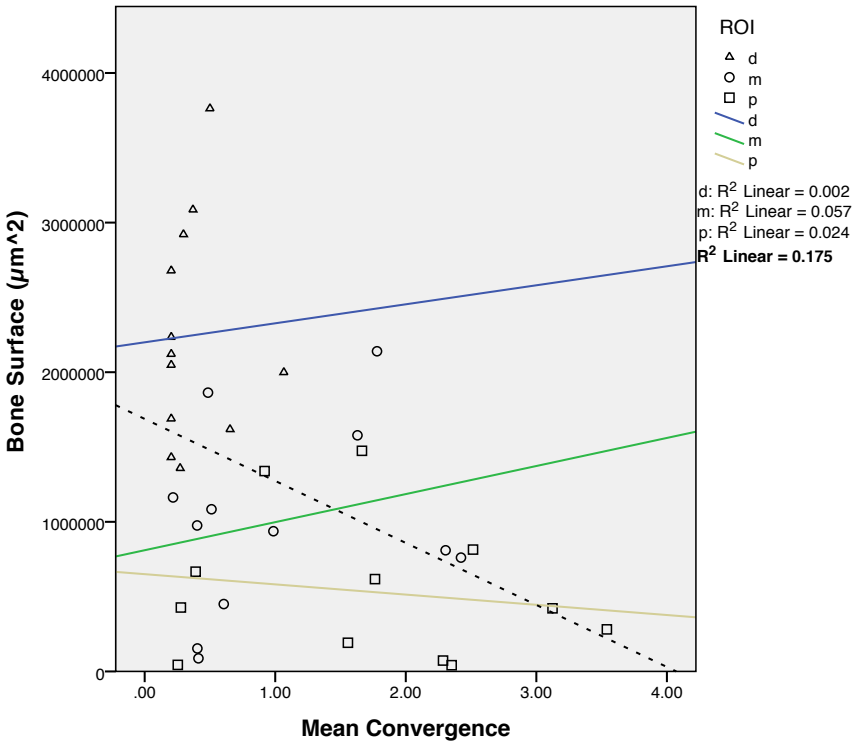

(b) Graph for DEI images

Figure 4.12: Linear relationships between mean convergence and bone surface for vertical images. ROIs: distal (d), medial (m), and proximal (p). Bolded r^2 for pooled results.

Table 4.10: Correlation between TFCM and architectural parameters for vertical images of high angle on the rocking curve. r^2 values are pooled values.

	r^2	Best Fit Model	Best Feature	p
Bone Volume (BV)	0.27	Linear	Homogeneity	< 0.01
Percent Bone Volume (BV/TV)	0.24	Linear	Mean convergence	< 0.01
Bone Surface (BS)	0.36	Linear	Homogeneity	< 0.01
Trabecular Number (Tb.N)	0.27	Linear	Homogeneity	< 0.01

Table 4.11: Correlation between TFCM and architectural parameters for vertical DEI images. r^2 values are pooled values.

	r^2	Best Fit Model	Best Feature	p
Bone Volume (BV)	0.25	Linear	Homogeneity	< 0.01
Percent Bone Volume (BV/TV)	0.26	Linear	Mean convergence	< 0.01
Bone Surface (BS)	0.42	Linear	Homogeneity	< 0.01
Trabecular Number (Tb.N)	0.28	Linear	Homogeneity	< 0.01

Table 4.11 shows the best fitting coefficients (pooled ROI results) of correlation between TFCM features and the morphological parameters for DEI images at point 0.5 of the rocking curve. Linear correlations were observed with several morphological parameters (Homogeneity /BS: $r^2 = 0.42, p < 0.01$, Mean convergence/BS: $r^2 = 0.18, p < 0.01$). The results for this set of images were stronger than the images at high angle. Figure 4.11(b) shows the linear relationships between homogeneity and BS. Figure 4.12(b) shows the linear relationships between mean convergence and BS. The coefficient of correlations of DEI images showed the best results.

TFCM features and architectural parameters have illustrated linear relationships between them. For all the sets of images, homogeneity has displayed stronger linear relationships with architectural parameters than other features. We can observe there is a linear change throughout the three regions of interests. Vertical DEI images illustrated the best set of images for TFCM experiment. TFCM homogeneity feature of DEI images explained more than 42% of variance in bone surface (BS) parameter.

4.4 LBP Results

4.4.1 Horizontal Orientation

Table 4.12 illustrates the best fitting coefficients (pooled ROI results) of correlation between LBP features and the morphological parameters for images of high angle side on the rocking curve. A linear correlation was found with several morphological parameters (LBP 11/BS: $r^2 = 0.27, p < 0.01$, LBP 11/ BS/TV: $r^2 = 0.24, p < 0.01$). Figure 4.13(a) shows the linear relationships between LBP 11 and BS. The coefficient of correlation was highest between LBP 11 and BS for this set of images. Figure 4.14(a) shows the linear relationships between LBP 11 and BS/TV.

Table 4.12: Correlation between LBP and architectural parameters for horizontal images of high angle on the rocking curve. r^2 values are pooled values.

	r^2	Best Fit Model	Best Feature	p
Bone Volume (BV)	0.22	Linear	LBP 11	< 0.01
Percent Bone Volume (BV/TV)	0.24	Linear	LBP 12	< 0.01
Bone Surface (BS)	0.27	Linear	LBP 11	< 0.01
Bone Surface Density (BS/TV)	0.24	Linear	LBP 11	< 0.01
Trabecular Number (Tb.N)	0.21	Linear	LBP 12	< 0.01

Table 4.13 shows the best fitting coefficients (pooled ROI results) of correlation between LBP features and the morphological parameters for DEI images at point 0.5 of the rocking curve. Linear correlations were observed with several morphological parameters (LBP 11/BS: $r^2 = 0.33, p < 0.01$, LBP 11/ BS/TV: $r^2 = 0.26, p < 0.01$). The results for this set of images were stronger than the images at high angle. Figure 4.13(b) shows the linear relationships between LBP 11 and BS. Figure 4.14(b) shows the linear relationships between LBP 11 and BS/TV. The coefficient of correlations of DEI images showed the best results.

4.4.2 Vertical Orientation

Table 4.14 illustrates the best fitting coefficients (pooled ROI results) of correlation between LBP features and the morphological parameters for images of high angle side on the rocking curve. A linear correlation was found with several morphological parameters (LBP 11/BS: $r^2 = 0.31, p < 0.01$, LBP 11/ BS/TV: $r^2 = 0.26, p < 0.01$). Figure 4.15(a) shows the linear relationships between LBP 11 and BS. The coefficient of correlation was highest between LBP 11 and BS for this set of images. Figure 4.16(a) shows the linear relationships between LBP 11 and BS/TV.

Table 4.15 shows the best fitting coefficients (pooled ROI results) of correlation between LBP features and the morphological parameters for DEI images at point 0.5 of the rocking curve. Linear correlations

Table 4.13: Correlation between LBP and architectural parameters for horizontal DEI images. r^2 values are pooled values.

	r^2	Best Fit Model	Best Feature	p
Bone Volume (BV)	0.23	Linear	LBP 11	< 0.01
Percent Bone Volume (BV/TV)	0.25	Linear	LBP 12	< 0.01
Bone Surface (BS)	0.33	Linear	LBP 11	< 0.01
Bone Surface Density (BS/TV)	0.26	Linear	LBP 11	< 0.01
Trabecular Number (Tb.N)	0.22	Linear	LBP 12	< 0.01

Table 4.14: Correlation between LBP and architectural parameters for vertical images of high angle on the rocking curve. r^2 values are pooled values.

	r^2	Best Fit Model	Best Feature	p
Bone Volume (BV)	0.22	Linear	LBP 11	< 0.01
Percent Bone Volume (BV/TV)	0.24	Linear	LBP 12	< 0.01
Bone Surface (BS)	0.31	Linear	LBP 11	< 0.01
Bone Surface Density (BS/TV)	0.26	Linear	LBP 11	< 0.01
Trabecular Number (Tb.N)	0.24	Linear	LBP 12	< 0.01

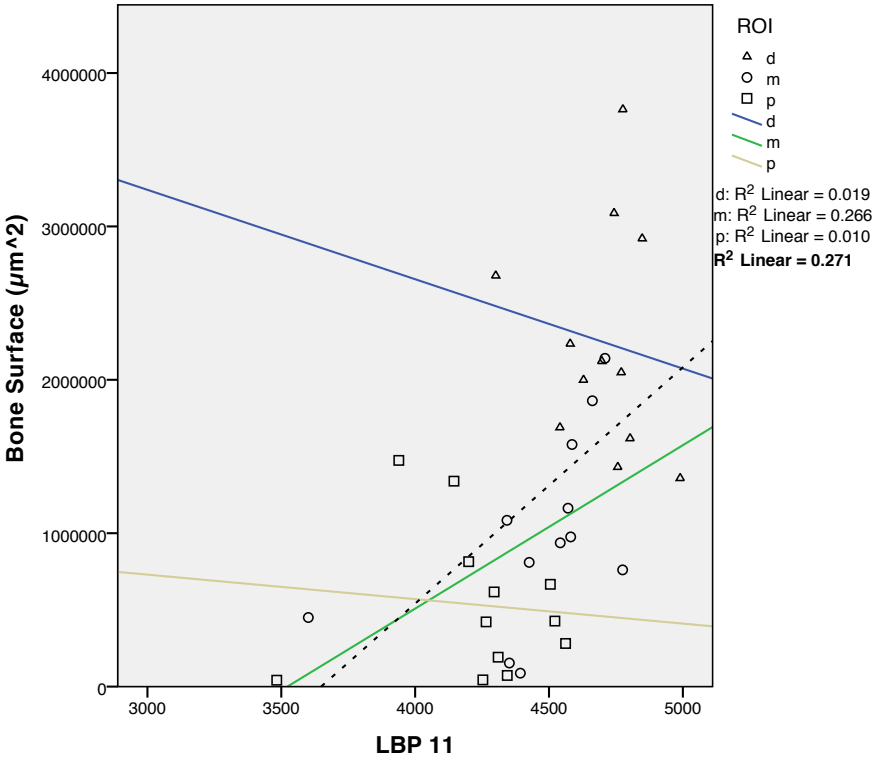

(a) Graph for high angle images

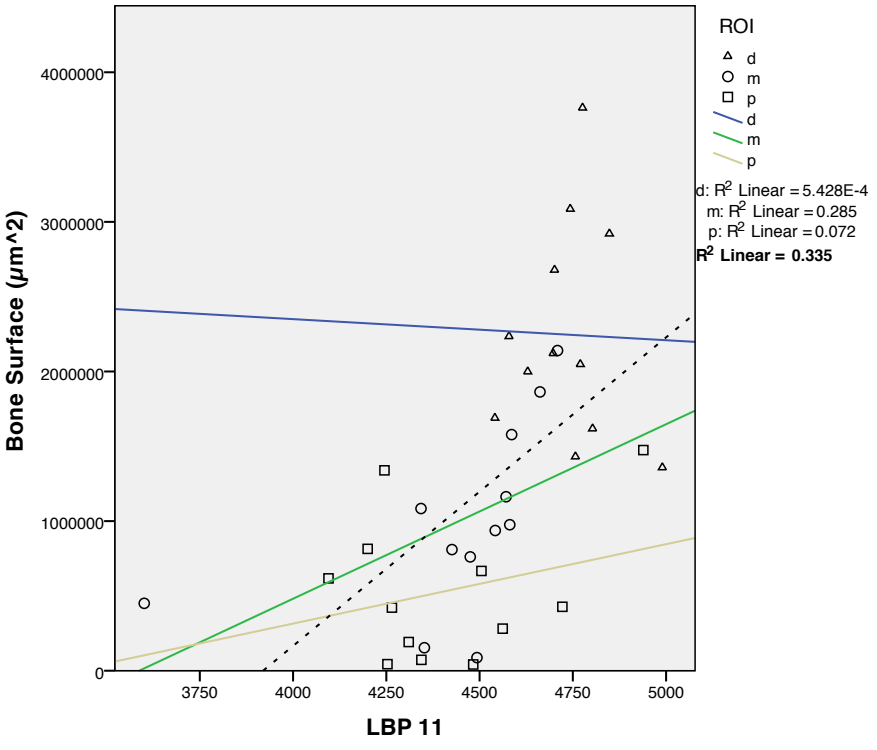

(b) Graph for DEI images

Figure 4.13: Linear relationships between LBP 11 and bone surface for horizontal images. ROIs: distal (d), medial (m), and proximal (p). Bolded r^2 for pooled results.

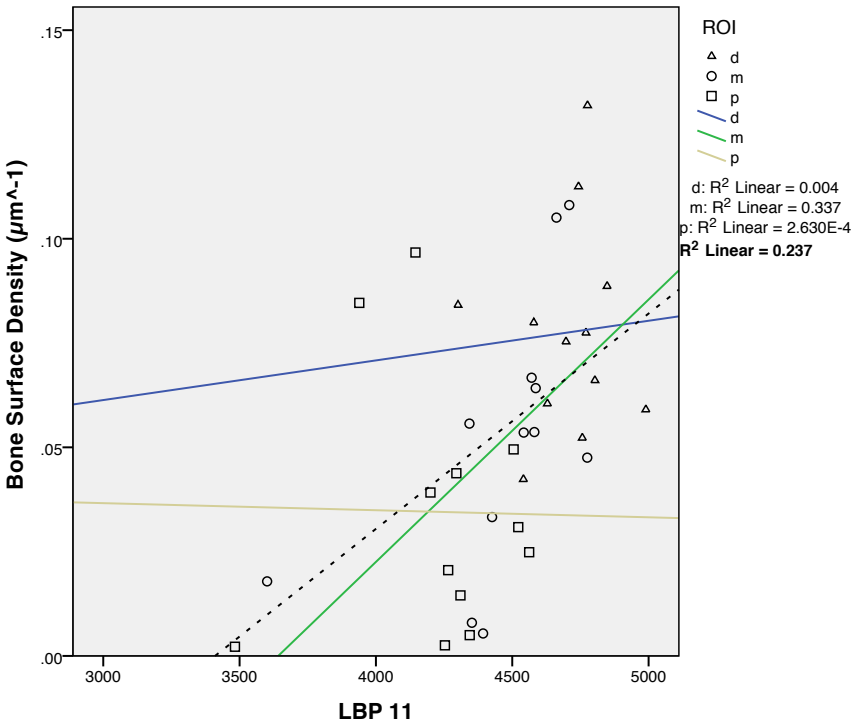

(a) Graph for high angle images

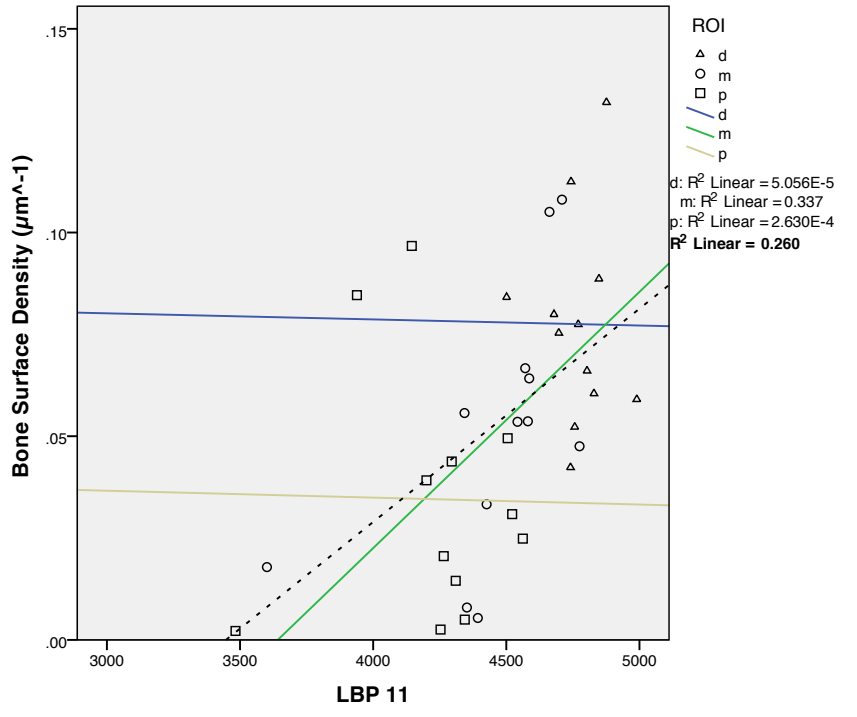

(b) Graph for DEI images

Figure 4.14: Linear relationships between LBP 11 and bone surface density for horizontal images. ROIs: distal (d), medial (m), and proximal (p). Bolded r^2 for pooled results.

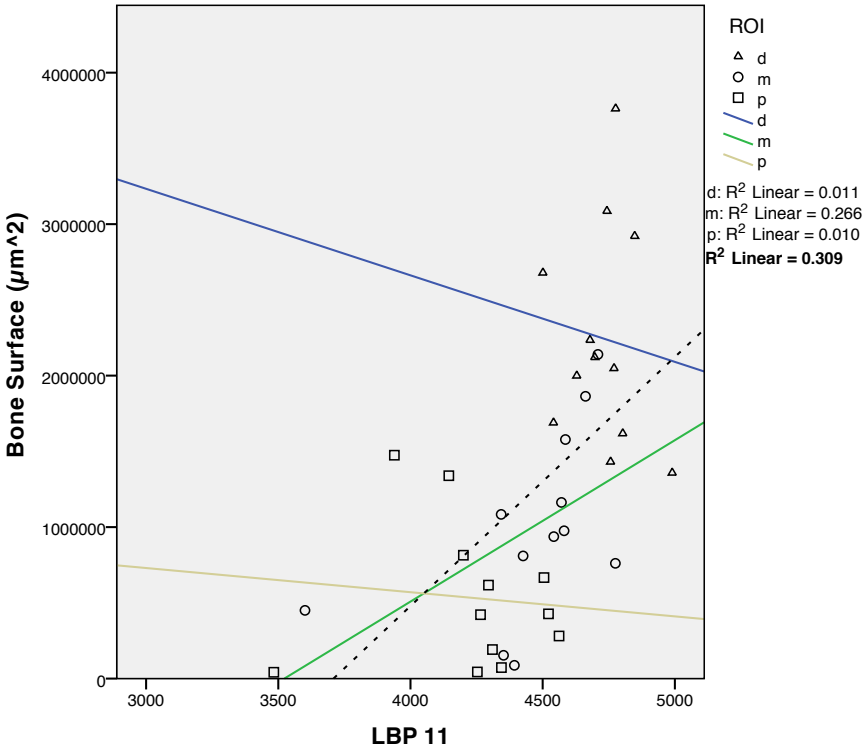

(a) Graph for high angle images

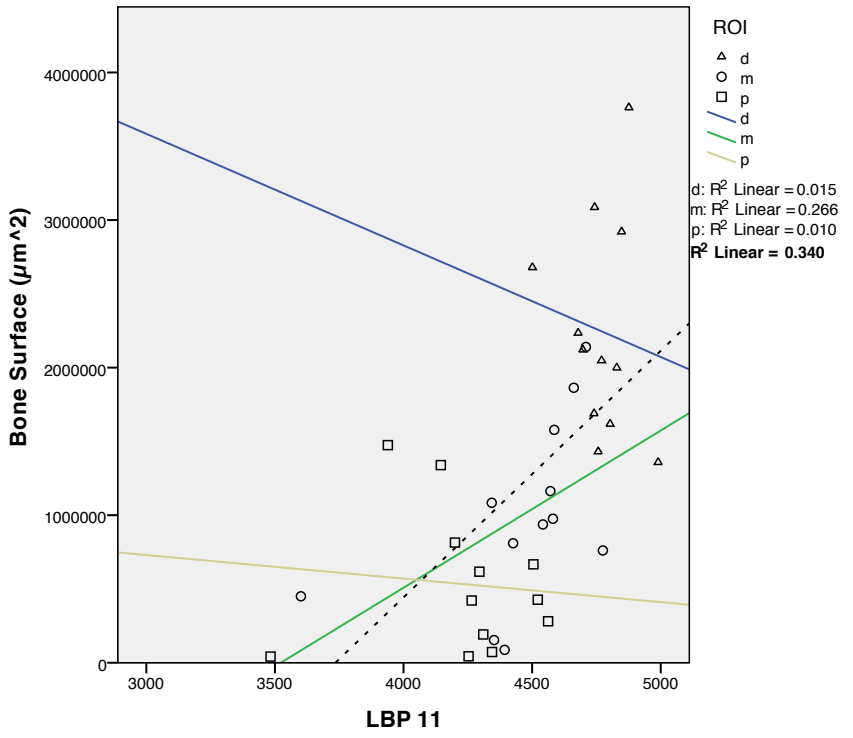

(b) Graph for DEI images

Figure 4.15: Linear relationships between LBP 11 and bone surface for vertical images. ROIs: distal (d), medial (m), and proximal (p). Bolded r^2 for pooled results.

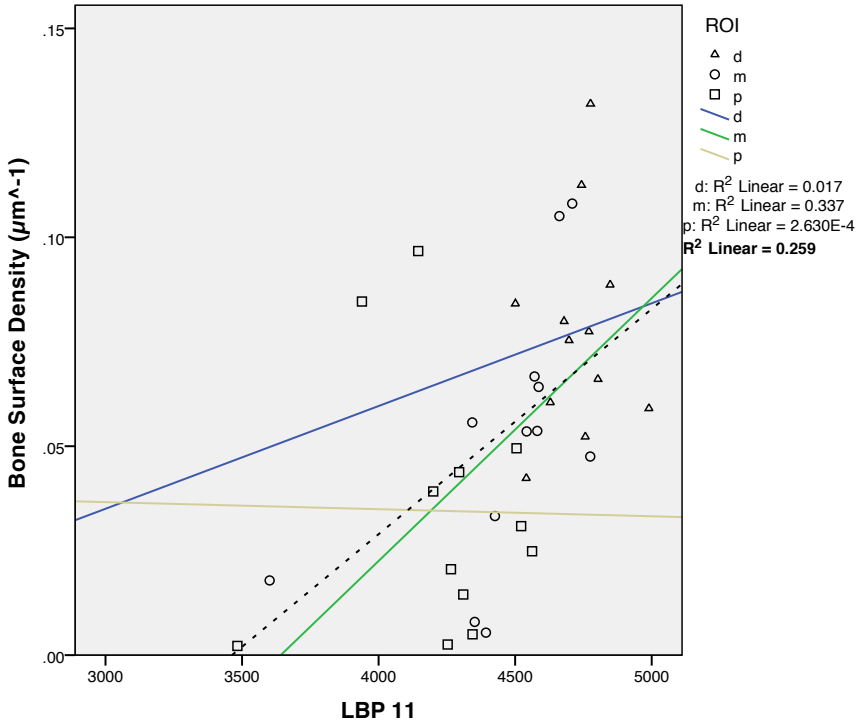

(a) Graph for high angle images

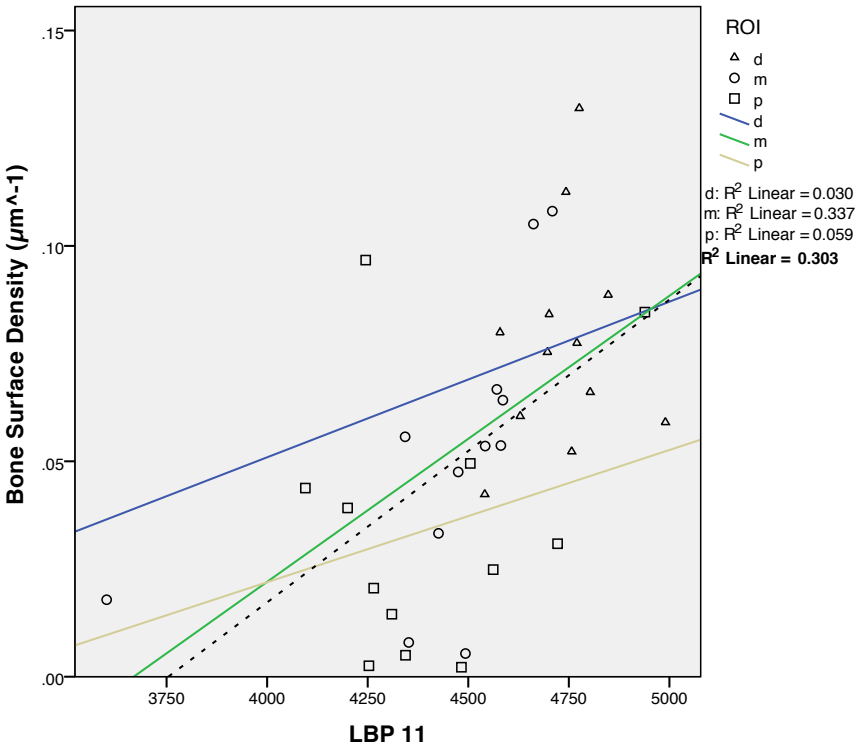

(b) Graph for DEI images

Figure 4.16: Linear relationships between mean LBP 11 and bone surface density for vertical images. ROIs: distal (d), medial (m), and proximal (p). Bolded r^2 for pooled results.

Table 4.15: Correlation between LBP and architectural parameters for vertical DEI images. r^2 values are pooled values.

	r^2	Best Fit Model	Best Feature	p
Bone Volume (BV)	0.23	Linear	LBP 11	< 0.01
Percent Bone Volume (BV/TV)	0.25	Linear	LBP 12	< 0.01
Bone Surface (BS)	0.34	Linear	LBP 11	< 0.01
Bone Surface Density (BS/TV)	0.30	Linear	LBP 11	< 0.01
Trabecular Number (Tb.N)	0.25	Linear	LBP 12	< 0.01

were observed with several morphological parameters (LBP 11/BS: $r^2 = 0.34, p < 0.01$, LBP 11/ BS/TV: $r^2 = 0.30, p < 0.01$). The results for this set of images were stronger than the images at high angle. Figure 4.15(b) shows the linear relationships between LBP 11 and BS. Figure 4.16(b) shows the linear relationships between LBP 11 and BS/TV. The coefficient of correlations of DEI images showed the best results.

Significant linear relationships were found between LBP operators and architectural parameters. For all the sets of images, LBP 11 has displayed some linear relationships with architectural parameters than other features. LBP 11 showed some correlation with BS and BS/TV. DEI images have shown stronger results than high angle images for both horizontal and vertical orientations. We observe significant linear change throughout the three regions of interests.

4.5 Fractal Dimension Results

4.5.1 Horizontal Orientation

Table 4.16 illustrates the best fitting coefficients (pooled ROI results) of correlation between fractal properties and the morphological parameters for images of high angle side on the rocking curve. A linear correlation was found with several morphological parameters (FD/BV: $r^2 = 0.21, p < 0.01$, FD/ BV/TV: $r^2 = 0.20, p < 0.01$, FD/BS: $r^2 = 0.32, p < 0.01$, FD/Tb.N: $r^2 = 0.26, p < 0.01$). Figure 4.17(a) shows the linear relationships between fractal dimension and BS. The coefficient of correlation was highest between fractal dimension and BS for all sets of images. Figure 4.18(a) shows the linear relationships between fractal dimension and BV.

Table 4.17 shows the best fitting coefficients (pooled ROI results) of correlation between fractal properties and the morphological parameters for DEI images at point 0.5 of the rocking curve. Linear correlations were observed with several morphological parameters (FD/BV: $r^2 = 0.27, p < 0.01$, FD/ BV/TV: $r^2 = 0.23, p < 0.01$, FD/BS: $r^2 = 0.40, p < 0.01$, FD/Tb.N: $r^2 = 0.27, p < 0.01$). The results for this set of images were stronger than the images at high angle. Figure 4.17(b) shows the linear relationships between fractal dimension and BS. Figure 4.18(b) shows the linear relationships between fractal dimension and BV. The

Table 4.16: Correlation between fractal and architectural parameters for horizontal images of high angle on the rocking curve. r^2 values are pooled values.

	r^2	Best Fit Model	Best Feature	p
Bone Volume (BV)	0.21	Linear	Kolmogorov FD	< 0.01
Percent Bone Volume (BV/TV)	0.20	Linear	Kolmogorov FD	< 0.01
Bone Surface (BS)	0.32	Linear	Kolmogorov FD	< 0.01
Bone Surface by Volume Ratio (BS/BV)	0.24	Linear	Lacunarity	< 0.01
Trabecular Number (Tb.N)	0.26	Linear	Kolmogorov FD	< 0.01

coefficient of correlations of DEI images showed the best results.

Table 4.17: Correlation between fractal properties and architectural parameters for horizontal DEI images. r^2 values are pooled values.

	r^2	Best Fit Model	Best Feature	p
Bone Volume (BV)	0.27	Linear	Kolmogorov FD	< 0.01
Percent Bone Volume (BV/TV)	0.23	Linear	Kolmogorov FD	< 0.01
Bone Surface (BS)	0.40	Linear	Kolmogorov FD	< 0.01
Bone Surface by Volume Ratio (BS/BV)	0.24	Linear	Lacunarity	< 0.01
Trabecular Number (Tb.N)	0.27	Linear	Kolmogorov FD	< 0.01

4.5.2 Vertical Orientation

Table 4.18 illustrates the best fitting coefficients (pooled ROI results) of correlation between fractal properties and the morphological parameters for images of high angle side on the rocking curve. A linear correlation was found with several morphological parameters (FD/BV: $r^2 = 0.28, p < 0.01$, FD/ BV/TV: $r^2 = 0.24, p < 0.01$, FD/BS: $r^2 = 0.42, p < 0.01$, FD/Tb.N: $r^2 = 0.26, p < 0.01$). Figure 4.19(a) shows the linear relationships between fractal dimension and BS. The coefficient of correlation was highest between fractal dimension and BS for all sets of images. Figure 4.20(a) shows the linear relationships between fractal dimension and BV.

Table 4.19 shows the best fitting coefficients (pooled ROI results) of correlation between fractal properties and the morphological parameters for DEI images at point 0.5 of the rocking curve. Linear correlations were observed with several morphological parameters (FD/BV: $r^2 = 0.31, p < 0.01$, FD/ BV/TV: $r^2 = 0.25, p < 0.01$, FD/BS: $r^2 = 0.47, p < 0.01$, FD/Tb.N: $r^2 = 0.27, p < 0.01$). The results for this set of images were stronger than the images at high angle. Figure 4.19(b) shows the linear relationships between fractal dimension and BS. Figure 4.20(b) shows the linear relationships between fractal dimension and BV. The

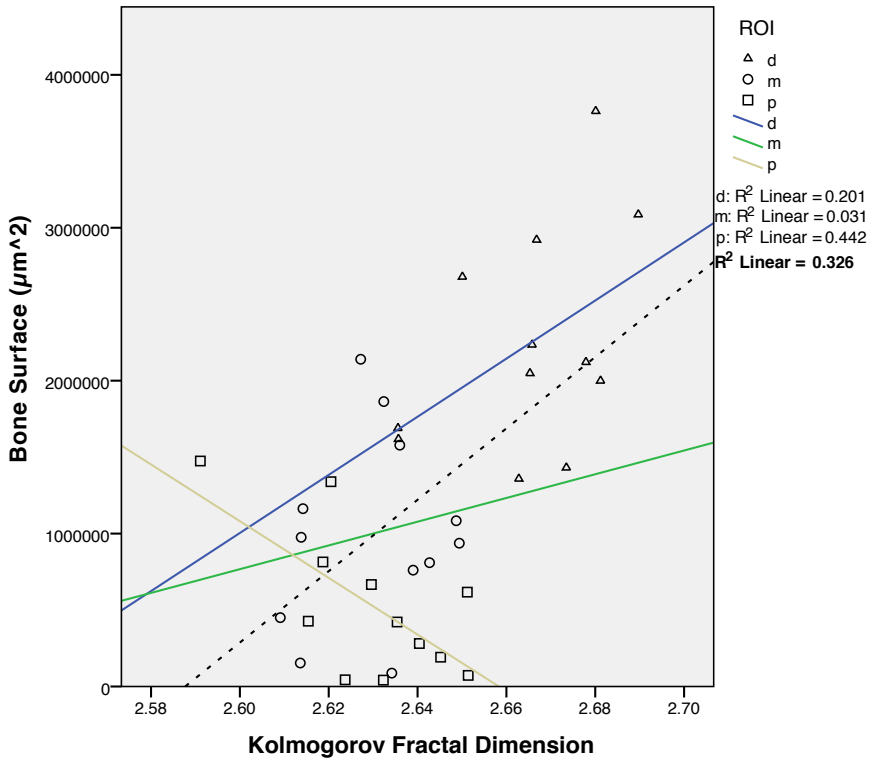

(a) Graph for high angle images

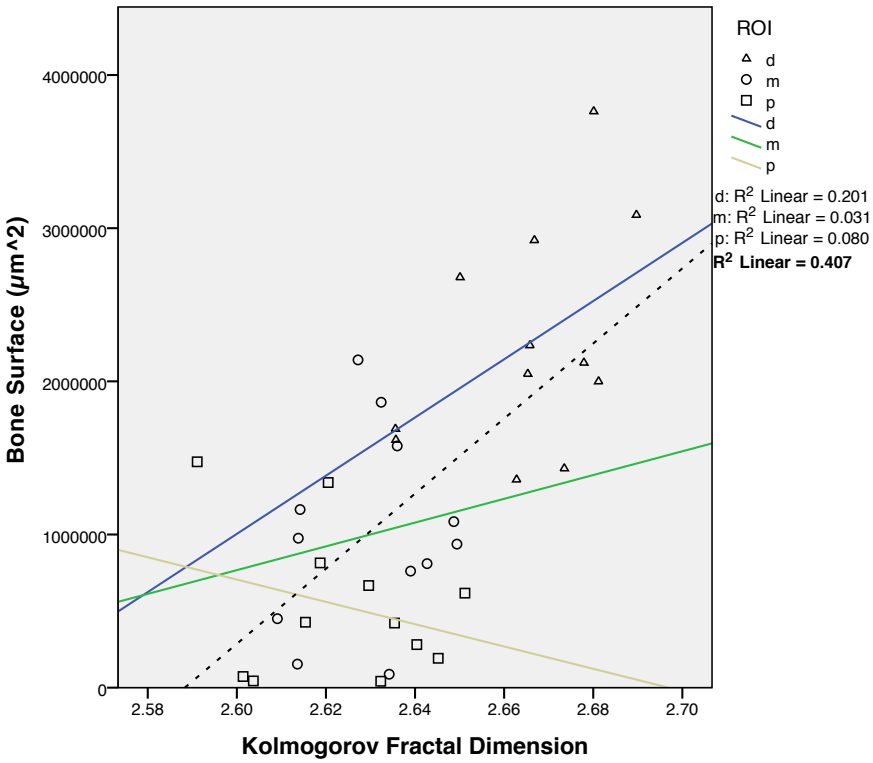

(b) Graph for DEI images

Figure 4.17: Linear relationships between Kolmogorov fractal dimension and bone surface for horizontal images. ROIs: distal (d), medial (m), and proximal (p). Bolded r^2 for pooled results.

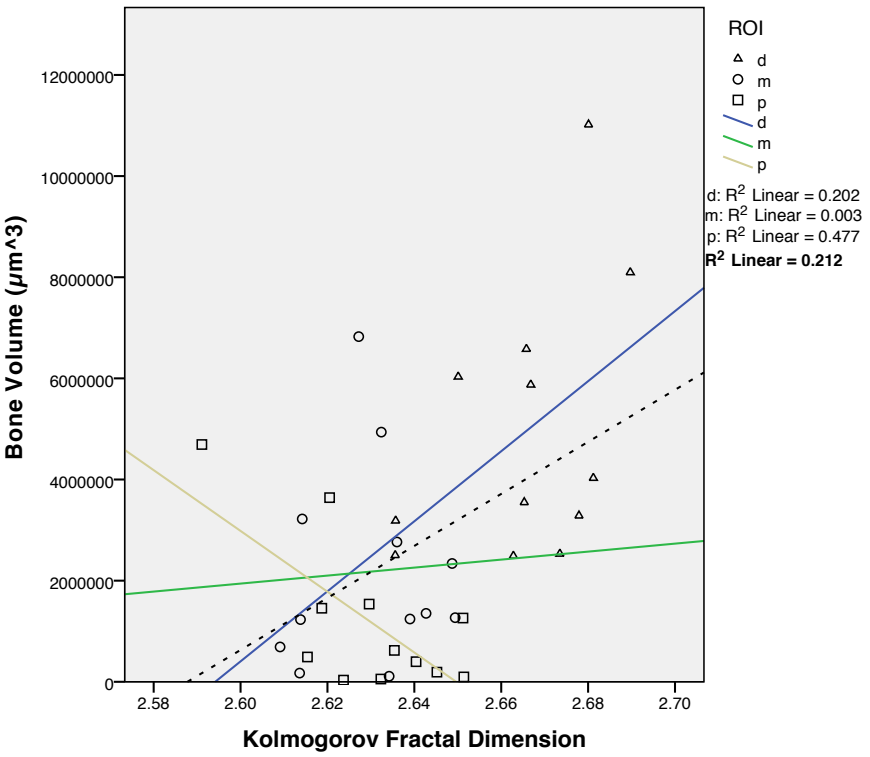

(a) Graph for high angle images

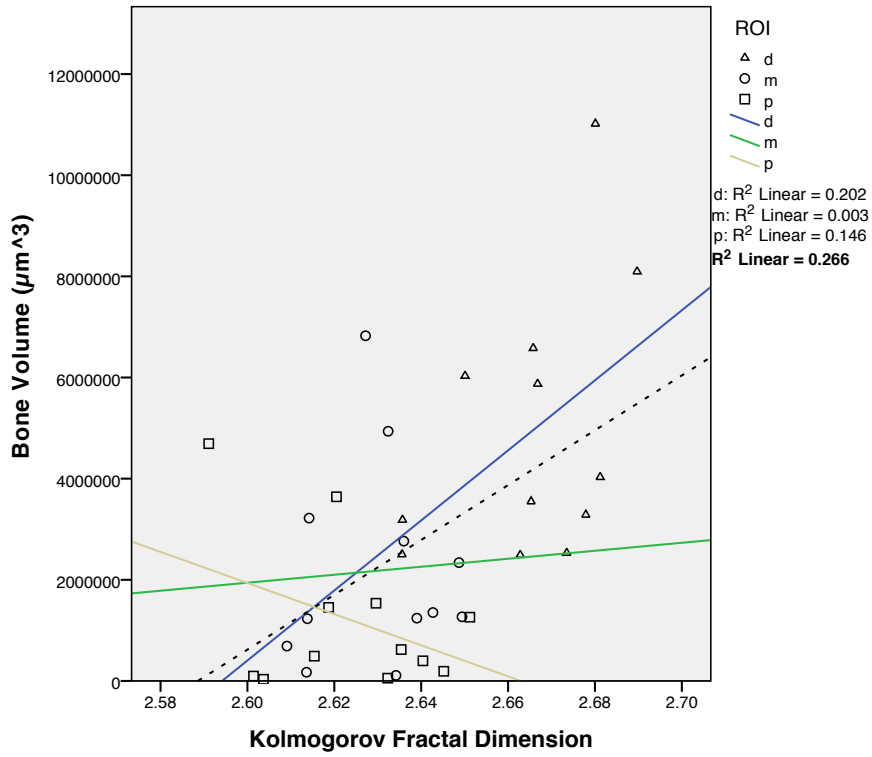

(b) Graph for DEI images

Figure 4.18: Linear relationships between Kolmogorov fractal dimension and bone volume for horizontal images. ROIs: distal (d), medial (m), and proximal (p). Bolded r^2 for pooled results.

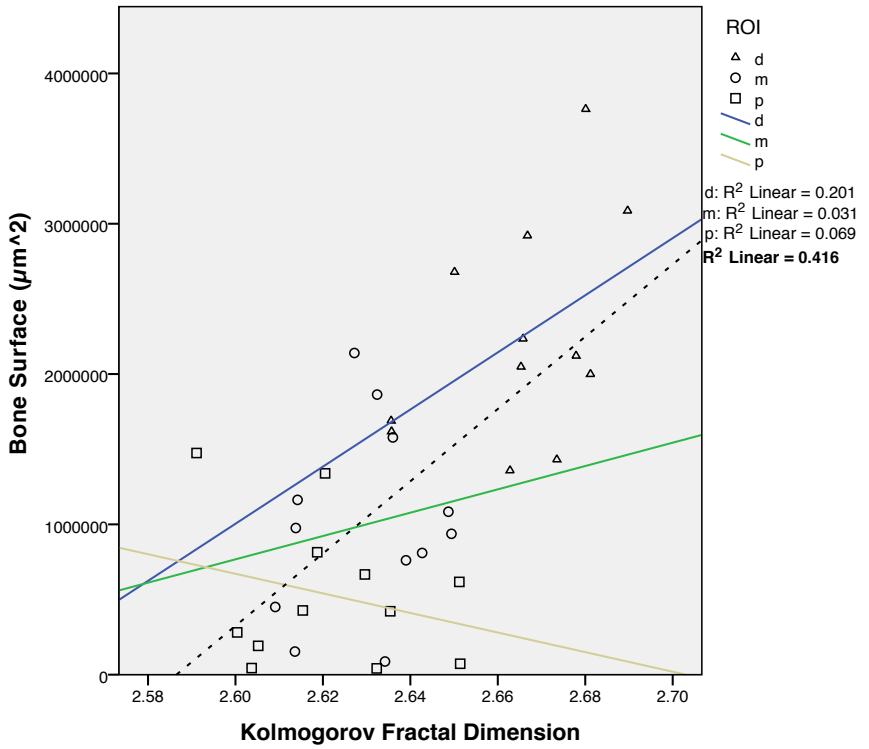

(a) Graph for high angle images

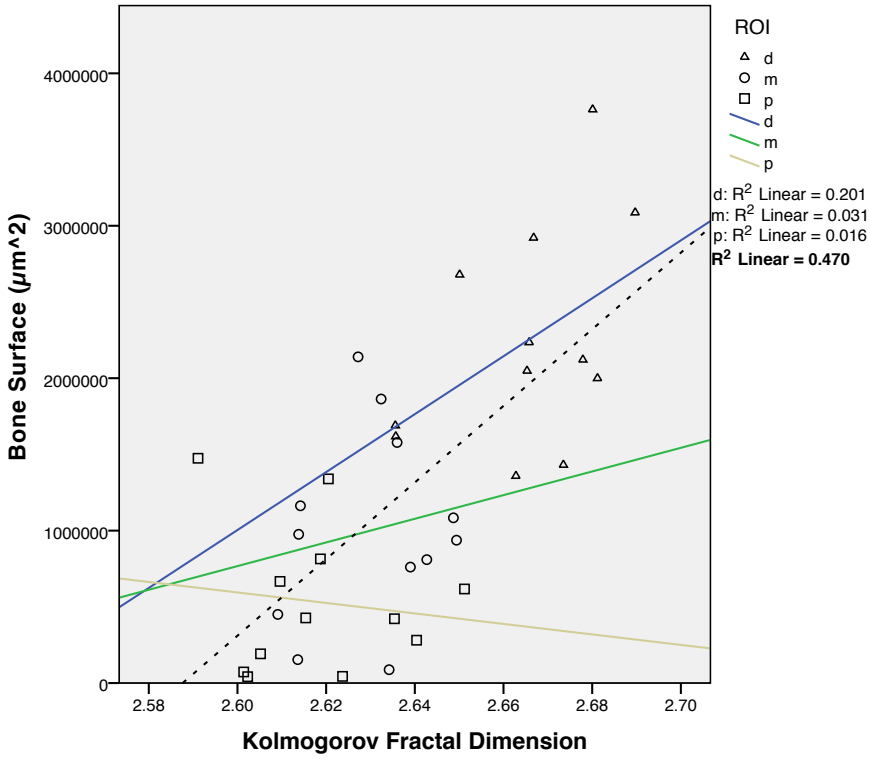

(b) Graph for DEI images

Figure 4.19: Linear relationships between Kolmogorov fractal dimension and bone surface for vertical images. ROIs: distal (d), medial (m), and proximal (p). Bolded r^2 for pooled results.

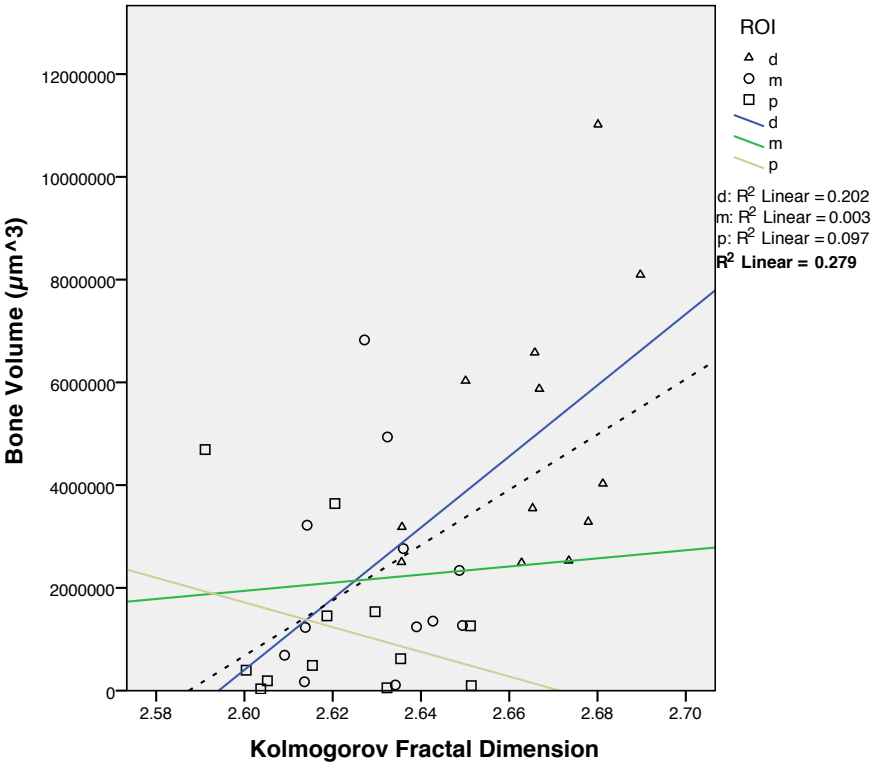

(a) Graph for high angle images

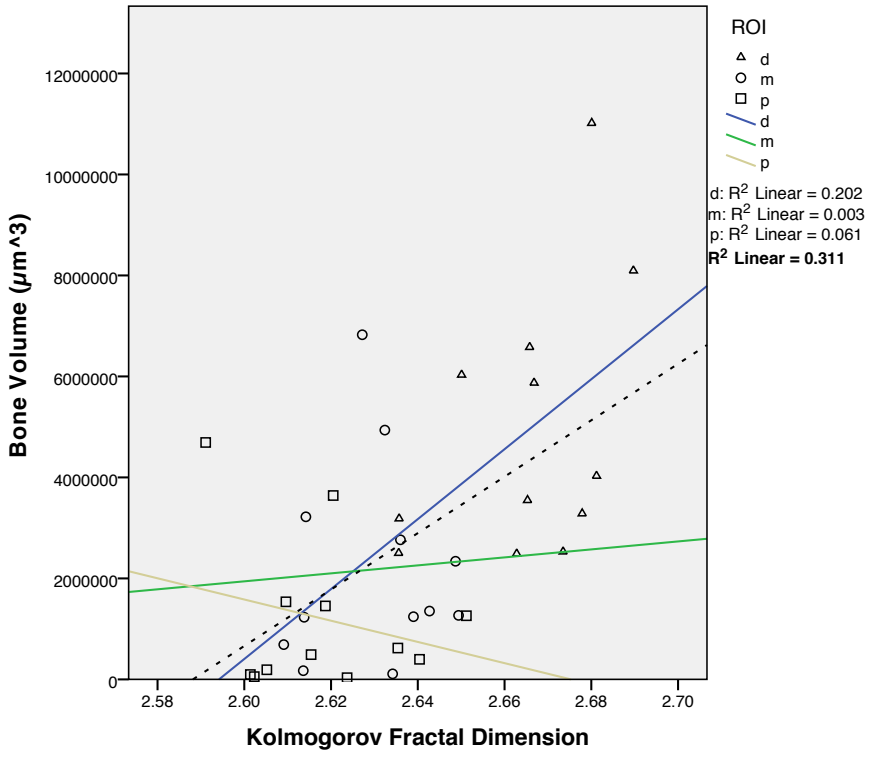

(b) Graph for DEI images

Figure 4.20: Linear relationships between Kolmogorov fractal dimension and bone volume for vertical images. ROIs: distal (d), medial (m), and proximal (p). Bolded r^2 for pooled results.

Table 4.18: Correlation between fractal and architectural parameters for vertical images of high angle on the rocking curve. r^2 values are pooled values.

	r^2	Best Fit Model	Best Feature	p
Bone Volume (BV)	0.28	Linear	Kolmogorov FD	< 0.01
Percent Bone Volume (BV/TV)	0.24	Linear	Kolmogorov FD	< 0.01
Bone Surface (BS)	0.42	Linear	Kolmogorov FD	< 0.01
Bone Surface by Volume Ratio (BS/BV)	0.25	Linear	Lacunarity	< 0.01
Trabecular Number (Tb.N)	0.26	Linear	Kolmogorov FD	< 0.01

coefficient of correlations of DEI images showed the best results.

Table 4.19: Correlation between fractal and architectural parameters for vertical DEI images. r^2 values are pooled values.

	r^2	Best Fit Model	Best Feature	p
Bone Volume (BV)	0.31	Linear	Kolmogorov FD	< 0.01
Percent Bone Volume (BV/TV)	0.25	Linear	Kolmogorov FD	< 0.01
Bone Surface (BS)	0.47	Linear	Kolmogorov FD	< 0.01
Bone Surface by Volume Ratio (BS/BV)	0.26	Linear	Lacunarity	< 0.01
Trabecular Number (Tb.N)	0.27	Linear	Kolmogorov FD	< 0.01

The box counting method is used to compute Kolmogorov fractal dimension (FD) and lacunarity. Linear relationships were found between Kolmogorov FD and architectural parameters. For all the sets of images, FD has displayed stronger linear relationships with architectural parameters than lacunarity. DEI images have shown stronger results than high angle images for both horizontal and vertical orientations. Between horizontal and vertical oriented images, vertical images illustrated stronger result for most cases. Among the results we have, vertical DEI images illustrated the strongest correlations. Fractal dimension parameter of DEI images explained more than 47% of variance in bone surface (BS) and 32% of variance in bone volume (BV).

Chapter 5

Discussion

5.1 Discussion

In this study different texture analysis methods were applied on synchrotron images obtained in different orientations (horizontal and vertical) at different points on the rocking curve and their DEI images of high and low angle images at a particular point on the rocking curve. The results of this study on 15 human cadaveric radii in an *ex vivo* set up demonstrated that most parameters for trabecular bone micro architecture are correlated with texture parameters extracted from diffraction enhanced images (DEI) using GLCM, TFCM, fractal dimension, and LBP operators. One of our aims in this study was to determine the texture features from different technologies and compare with our findings and provide a good relationship with bone parameters. Although this requires access to wide range of technologies, the best result in terms of time, availability, and cost analysis can be found.

Significant correlation between high and low angle images were observed. So, we chose high angle and the DEI images formed by the high and low angle images to be analyzed . The correlation coefficients for high and low angle images at 0.5 point on the rocking curve were very strong (Energy: $r^2 = 0.95$, Contrast: $r^2 = 0.94$, Kolmogorov Fractal Dimension: $r^2 = 0.93$, Lacunarity: $r^2 = 0.92$, Coarseness: $r^2 = 0.91$, Homogeneity: $r^2 = 0.92$, Variance: $r^2 = 0.89$). We only presented the results for high and DEI images at 0.5 point on the rocking curve because their results have outperformed the results from other set of images.

In our study, we found significant correlations between parameters (Energy/Tb.N: $r^2 = 0.37, p < 0.01$, Energy/ BS/BV: $r^2 = 0.39, p < 0.01$, Energy/ BV/TV: $r^2 = 0.38, p < 0.01$) for DEI images. The GLCM energy feature of DEI images explained more than 39% of variance in BS/BV, 38% of variance in BV/TV, and 37% of variance in Tb.N. These results were found for DEI images of vertical orientations at 0.5 point on the rocking curve. The results of DEI images at 0.25 on the rocking curve were not as good as the results of DEI images at 0.5 on the rocking curve (Energy/Tb.N: $r^2 = 0.35, p < 0.01$, Energy/ BS/BV: $r^2 = 0.36, p < 0.01$, Energy/ BV/TV: $r^2 = 0.34, p < 0.01$). Other results are provided in the Appendices [B,C,D]. From the results in Appendix D, we demonstrated that DEI images of vertical orientations at 0.5 on the rocking curve were the best dataset in our study. Table 5.1 summarizes the best results of our study for vertical DEI images. We will discuss our results in comparison with other studies that used different imaging techniques. We will also discuss our limitations in this study later in this Chapter.

Table 5.1: Coefficients of correlations (r^2) between texture features and bone parameters for vertical DEI images. ns = not significant. r^2 values are pooled values.

Texture parameters	Bone parameters					
	BV	BS	BV/TV	BS/BV	BS/TV	Tb.N
GLCM						
Contrast	0.29	0.28	ns	ns	ns	ns
Correlation	0.31	0.30	0.29	ns	0.31	0.27
Homogeneity	ns	ns	0.35	0.29	ns	ns
Energy	0.31	0.31	0.38	0.39	0.32	0.37
TFCM						
Coarseness	0.24	0.25	ns	0.25	0.22	ns
Homogeneity	0.25	0.42	0.26	ns	ns	0.28
Mean Convergence	ns	ns	0.26	ns	ns	ns
Variance	0.20	0.23	ns	ns	ns	0.24
Code Entropy	0.26	0.21	ns	ns	ns	0.19
Code Similarity	0.23	ns	0.24	ns	ns	0.20
Resolution Similarity	ns	ns	ns	ns	ns	ns
LBP						
LBP 11	0.23	0.34	0.25	ns	0.30	ns
LBP 12	ns	ns	0.25	ns	ns	0.25
Fractal Analysis						
Kolmogorov FD	0.31	0.47	0.25	0.26	ns	0.27
Lacunarity	ns	ns	ns	ns	0.26	ns

Bone is a 3D material, therefore, 3D bone micro architecture analysis could be a better means to examine the structure of bone than 2D analysis. However, 3D image data is hard to acquire, hence our study focused on 2D analysis. In addition to that texture analysis is a good technique to predict the bone strength [8]. Osteoporosis fractures occur due to low bone mass in the bone and the clinical practice, DXA can estimate the strength of the bone by 70% [6], therefore, there is a need for other measurements to be evaluated. Significant changes in the bone micro architecture can be observed whereas DXA parameter changes are minimal [14]. Several methods have been used to assess the bone quality and distinguish between osteoporotic and non-osteoporotic fracture. Among the many methods, fractal analysis have been widely used in many studies [33, 74, 31]. Fractal parameters such as Minkowsky fractal dimension, Kolmogorov fractal dimension, and H_{mean} have been widely used [19, 67, 25].

5.1.1 Comparison: DEI vs Conventional X-ray

Several studies [48, 8, 25, 32] showed that texture parameters from 2D radiographic images using a high-resolution digital X-ray device had good correlation with 3D bone parameters. Chappard et al. [20] reported that significant relationships were reported in the study (Tb.Sp/GLN: $r^2 = 0.60$, Tb.N/FD: $r^2 = 0.61$). Tb.Th had also showed good relationships with 2D texture parameters. Using a similar approach, it is reported by Bacchetta et al. [8] that fractal dimension showed moderate correlation with architectural parameters (FD/Tb.N: $r^2 = 0.26$, FD/Tb.Sp: $r^2 = 0.30$). Huber et al. [41] reported that texture analysis of radiographic images demonstrated significant relationships with bone parameters. BV/TV, Tb.Th, and Tb.N were highly correlated with texture parameters up to $r^2 = 0.61$(Minkowski FD, GLCM).

It was reported by Ranjanmennahary et al. [68] texture analysis of radiographic images of human femur bones showed significant correlations between parameters (Energy/ BV/TV: $r^2 = 0.59$, Correlation/ BV/TV: $r^2 = 0.35$) for femoral head and (Energy/ BV/TV: $r^2 = 0.54$, Correlation/ BV/TV: $r^2 = 0.25$) for greater trochanter. Steines et al. [76] studied radiographic images taken from cadaver femur bones. Moderate relationships were found between fractal and bone parameters (FD/Tb.N: $r^2 = 0.40$, FD/ BV/TV: $r^2 = 0.24$, FD/Tb.Sp: $r^2 = 0.42$). No significant relationship was observed between fractal dimension and Tb.Th parameters. These studies proved that fractal dimension and GLCM features can be associated with bone parameters to determine the bone architecture. In our study coefficients of correlations were similar to the studies mentioned above, thus, it can be considered that DEI images has the potential for bone architecture analysis.

5.1.2 Comparison: DEI vs CT

There is large number of studies present in the field of texture analysis of 2D projection images from micro-CT and 3D bone parameters [31, 29, 74, 33, 79]. In 2012 Winzenrieth et al. [79] reported the correlation between 3D trabecular bone architecture parameters and TBS. It was reported that TBS and 3D bone parameters were significantly correlated (Connectivity: $r^2 = 0.75$, Tb.N: $r^2 = 0.65$, Tb.Sp: $r^2 = 0.49$). It is also demonstrated in their study that low image resolution and noise can greatly affect the relationship. The study of Guggenbuhl et al. [33] stated that texture features from 2D projecttion images of human iliac crest biopsies using fractal analysis and gray level co-occurrence matrix showed moderate correlations (Tb.N/ FD: $r^2 = 0.34$, Tb.Th/ FD: r^2 =35, Tb.N/VGLN: $r^2 = 0.36$). The results of our study demonstrated significant relationships between texture features of DEI images and 3D bone parameters. This confirms that DEI has the capability to determine the association of 2D parameters with 3D bone parameters.

Accordingly, Sidorenko et al. [74] evaluated human vertebrae to correlate with texture parameters of 3D micro-CT gray-level images. Significant correlation were found between parameters (BV/TV / FD: $r^2 = 0.37$), Tb.N/FD: $r^2 = 0.50$). Similar to the study of Sidorenko et al., Parkinson et al [31] carried out a research study which reported that significant relationships were observed (Tb.N/ Fractal Dimension: r^2

= 0.39, BV/TV/ Fractal Dimension: $r^2 = 0.34$, Tb.Sp/ Fractal Dimension: $r^2 = 0.41$). In the study of Diederichs et al. [29], it was reported that significant correlations were found between bone parameters and texture parameters (BV/TV /Contrast: $r^2 = 0.35$, Tb.N/Contrast: $r^2 = 0.24$) at $p < 0.05$ significant level. They also demonstrated that the combination of BMD and texture features performed better with 3D bone parameters than each parameters alone.

5.1.3 Comparison: DEI vs DXA

Texture bone score (TBS) is a novel gray-level texture feature from DXA images. Large number of studies [35, 71, 75] showed that TBS can be a good predictor of the bone architecture, thus, it can be used to determine the strength of the bone. Although DXA has limited spatial resolution which hinders acquiring more details about bone micro-architecture, TBS of DXA images proved to have good correlations with 3D bone parameters [71, 35]. In 2011 Hans D. et al. [35] examined 30 dry human vertebrae to investigate the association of TBS and BMD with 3D HR-CT micro architecture parameters. DXA was used to measure the BMD and TBS from DXA images. HR-CT (isotropic 93 μm voxel size) measured the 3D parameters. Significant correlations were encountered between TBS and 3D parameters similar to our results that we got for fractal dimension (FD) with 3D parameters. It was reported that BMD was also highly correlated with 3D parameters. But the combination of BMD and TBS performed better than each parameter alone and explained 65% of the variance in BV/TV, 51% of the variance in Tb.Th, 63% of the variance in Tb.Sp, and 82% of the variance in Tb.N. Better results were observed when BMD and TBS were combined to run a multivariate regression analysis with bone parameters than each parameter alone. In our study further improvement of the results can be achieved if the combination of BMD and FD is considered. DXA is routinely used in clinical practices, therefore, DXA parameters (BMD and TBS) and DEI texture parameters can be combined to observe their association with bone parameters.

Two other articles focused on the assessment of structural parameters [71, 75]. Roux et al. [71] investigated an *ex vivo* study to observe the relationship between TBS and bone micro architecture and mechanical behaviour of human vertebrae. 16 donors (7 men and 9 women) were scanned for DXA images and micro-CT device ($SkyScan^{TM}1076, Belgium$) was used to collect trabecular bone properties. Significant correlations between TBS and other parameters (Tb.Th: $r^2 = 0.35$, SMI: $r^2 = 0.38$, stiffness: $r^2 = 0.40$) were reported. However, the combination of Tb.Th, TBS and SMI performed better than each parameter alone and explained 79% of the variance in stiffness. It is also reported by Silva et al. [75] in 2013 that texture bone scores (TBS) from DXA images of human radius and high-resolution peripheral quantitative computed tomography (HR-pQCT) bone parameters were highly correlated. At the radius, TBS was correlated with volumetric densities, trabecular bone volume, and whole bone stiffness. TBS was not correlated with trabecular thickness.

5.1.4 Comparison: DEI vs MRI

Magnetic resonance imaging has been a suitable imaging technique to observe the changes in trabecular bone architecture. Pothuaud et al. [66] in 2000 conducted a research work to determine the correlation between fractal properties and trabecular bone properties of the fracture site - the hip. Trabecular bone images were obtained by MRI. They extracted Minkowski fractal dimension using box counting method. They found statistically significant relationship between fractal dimension and porosity in the 3D architecture. Significant relation was observed between fractal dimension and trabecular number ($r^2 = 0.74$). There was also a significant relationship between porosity and trabecular number ($r^2 = 0.67$).

Mueller et al. [60] in 2005 investigated a study to obtain different 3D-based scaling index method (SIM) and 2D bone histomorphometric parameters. MRI images of forty postmenopausal women with and without osteoporotic spine fracture were obtained using 1.5 T MR scanner (ACS-NT, Philips, Netherlands). SIM method was applied on MRI images and histomorphometric parameters were collected from MRI images with pixel size $10\mu m$. Moderate relationships were found between 2D parameters and histomorphometric measurements. Similarly, Zhang et al. [80] examined sixty subjects to obtain MRI images using 3-T Signa systems (General Electric, USA). The study reported moderate correlations. In the study of Cortet et al. [26] examined 24 cadaveric specimen to determine the relationship between 2D MRI images and 3D micro-CT bone parameters. The study reported significant relationship between 2D and 3D parameters. Fractal dimension was significantly correlated with Tb.Th, Tb.N, BV/TV, and Tb.Sp (r^2 upto 0.6). Other studies [55, 9, 10] also reported moderate correlation ships between 2D and 3D parameters. The results of these studies demonstrated that their coefficients of correlations were slightly better than the results in out study. However, according to the results in this study, it can be stated that texture analysis of DEI images provide significant association with the 3D trabecular bone parameters.

5.1.5 ROI results

In Chapter 4, all the results mentioned were pooled results of the ROIs. We observed that pooling the ROIs provides an overall picture of relations between DEI measures and micro-CT parameters but this violates the assumption of independence. As such, the statistical values need to be viewed with some caution. Through the analysis of the within ROI results, it can be demonstrated that some texture features were significantly correlated with bone parameters. For example, in the GLCM results section in Chapter 4 within ROI results showed that medial (m) and proximal (p) results were better than the pooled results. Table 5.2 shows the within ROI results for GLCM texture features of DEI vertical images with bone parameters. From table 5.2, it can be observed that proximal ROI results of energy and bone parameters were 0.50, 0.44, and 0.37 whereas pooled results were 0.39, 0.38, and 0.37. These pooled results were greatly affected by the distal ROI results (0.23, 0.27, and 0.26). Therefore, the correlation pool of ROIs may be suspected to violate the assumption of independence.

Table 5.2: Coefficients of correlations (r^2) for within ROIs between GLCM energy and bone parameters for vertical DEI images.

ROI	Bone parameters		
	BS/TV	BV/TV	Tb.N
Medial (m)	0.42	0.36	0.37
Proximal (p)	0.50	0.44	0.37

Similarly for LBP, the medial ROI result was 0.33 for LBP 11 and BS/BV whereas the pooled result was 0.30. Similarly for fractal analysis, proximal ROI results were 0.44 and 0.47 for Kolmogorov fractal dimension with BS and BV whereas pooled results were 0.32 and 0.29 respectively. Among the texture methods GLCM showed better results in terms of within ROI results the the results of other methods. We can also demonstrate that distal ROI results were slightly poorer than the results of other ROIs. Although the pooled results were worse than the results of individual ROI, we focus on the pooled results because there were insufficient samples used in the experiment.

5.1.6 Performance of TFCM and LBP

To the best of our knowledge, this is the first study that used TFCM features and LBP operators to measure the relationship between bone parameters and texture parameters. TFCM features were used by Horng et al. [39] for classification of liver sonography of ultrasound images and also for target detection [50]. Significant correlation was observed using TFCM features (Homogeneity /BS: pooled $r^2 = 0.42, p < 0.01$) in DEI images at 0.5 point on the rocking curve. TFCM homogeneity feature of DEI images explained more than 42% of variance in bone surface (BS) parameter. The coefficient of correlation for DEI images at 0.125 on the rocking curve (Homogeneity /BS: pooled $r^2 = 0.38, p < 0.01$) was poorer than the result of images at 0.5. There was no significant relationships between other TFCM features (mean convergence, code entropy, code similarity, resolution similarity) and bone parameters. These results stated that TFCM texture features can be used in the analysis of trabecular bone micro architecture analysis.

As it is well established that LBP operators can detect texture features that can be used for classification, it was our interest to use LBP operators in our study to observe any correlations. Our study showed that there were correlations between LBP operators and bone parameters (LBP 11/BS: pooled $r^2 = 0.34, p < 0.01$, LBP 11/ BS/TV: pooled $r^2 = 0.30, p < 0.01$). LBP operators of DEI images explained more than 34% of variance in bone surface (BS) and 30% of variance in bone surface density (BS/TV). The coefficients of correlation for DEI images at 0.25 on the rocking curve (LBP 11/BS: pooled $r^2 = 0.30, p < 0.01$, LBP 11/ BS/TV: pooled $r^2 = 0.25, p < 0.01$) were poorer than the result of DEI images at 0.5. Other image sets were also tested (see results in Appendix D) but DEI images proved to be the best set of images showing strongest

correlations among other sets of images. Although the results from LBP operators used in our study demonstrated moderate relationship between 2D and 3D parameters of bone, it is possible to improve the results if other bone parameters (TBS, BMD) were combined with LBP operators in a multi-variate regression analysis.

In this study the performance of different imaging technologies were compared in the analysis of trabecular bone micro architecture and this study also reported the best 2D parameters that significantly correlated with 3D bone parameters. This study applied texture analysis method in 2D DEI images and compared the results with other technologies such as computed tomography (CT), magnetic resonance imaging (MRI), conventional X-ray, and DXA imaging. DEI is a novel imaging technology with the ability to produce high resolution images in the analysis of bone micro architecture described in Cooper at al. [24]. Another aim of this study was to examine the performance of TFCM and LBP operators and determine how well these parameters establish their relationship with 3D bone parameters. Our study gives a good support to using texture analysis methods in the study of bone imaging as we used four different methods (GLCM, TFCM, LBP, and FD). All our methods showed some potential but among them GLCM and FD were better than TFCM and LBP. The results indicate differences in DEI images with different orientations. Besides this contribution, we also tried to find limitations of our study. First, the number of samples evaluated in this study may be considered small compared to most other *ex vivo* studies [17, 44, 49]. In a larger sample the analysis may have performed better. Second, cortical micro archtecture may have contributed to the texture in the images in the high resolution synchrotron DEI measures moreso than in tradition radiographs. Finally, the correlation pool of ROIs may be suspected to violate the assumption of independence.

Chapter 6

Conclusions

6.1 Conclusion

This study has showed that the texture analysis of the human forearm (radii) bone can provide a measured characterization of bone architecture. This pilot work was based on the search for correlation in an unknown sample, without accounting for the status of the individuals. The correlation between texture features and 3D micro-CT parameters were evaluated on 8 different image datasets consisting of 15 synchrotron images of human wrist bone. We extracted three regions of interest in the bones. Four different texture analysis methods were used. We applied GLCM, TFCM, LBP, and Fractal analysis on the images to extract features. We collected the bone parameters which characterize bone architecture using SkyScan CTan software to determine the correlation with texture features.

The results showed that at any point on the rocking curve, the high and low angle images are highly correlated indicating that single-image analysis need only to be carried out on one side of the rocking curve. Among the image sets, DEI images in horizontal and vertical images performed better compared to images from just one side of the rocking curve. Vertical images showed stronger coefficients of correlation than horizontal images among all the image sets. GLCM energy feature of DEI images explained more than 39% of variance in bone surface by volume ratio (BS/BV), 38% of variance in percent bone volume (BV/TV), and 37% of variance in trabecular number (Tb.N). TFCM homogeneity feature of DEI images explained more than 42% of variance in bone surface (BS) parameter. LBP operator - LBP 11 of DEI images explained more than 34% of variance in bone surface (BS) and 30% of variance in bone surface density (BS/TV). Fractal dimension parameter of DEI images explained more than 47% of variance in bone surface (BS) and 32% of variance in bone volume (BV). All these results mentioned above are pooled ROI results. In conclusion, the contribution of this thesis is summarized as follows:

- High and low angle images are highly correlated so only one of the pair of images for a given angle need to be analyzed when considering single images.
- Vertically oriented DEI images were the best set among the image datasets to show significant correlation.
- Several features among the four methods have showed significant correlation with the bone parameters.

6.2 Potential Future Work

Some potential future extensions of this work are listed as follows:

- Statistical texture features can be experimented with the combination of DXA parameters to determine the correlation. TBS, collected from DXA, have been used in many studies (we added some of them in literature review) and they stated that combining TBS with other texture features have demonstrated better results. In future if we can have the opportunity to extract BMD score and TBS feature using DXA from bone, we would like to combine our other texture features (TFCM, GLCM, LBP, and fractal dimension), we might observe good results.

- The potential also exists to expand this work beyond the wrist and to look at the hip. Other fracture sites - hip and spine could be of great interest. The potential to expand into assessment of the hip and spine would represent an additional advantage over peripheral scanning modalities such as HR-pQCT. We can also compare the analysis of 2D projection image from HR-pQCT with the DEI image analysis.

- This work can be carried out in larger dataset. In our study, we had 15 samples which is not adequate. More samples could have proved better results because the outliers in the results in texture features would have less effect of our results.

- The potential *ex vivo* studies in animal model systems. There are lots of research work based on animal model systems can be used because of the good collection of samples. It is not always easy to collect large dataset of human samples.

References

[1] http://www.cgtextures.com/.

[2] http://www.osteoporosis.ca/.

[3] ImageJ software for fractal analysis.

[4] T. Ahonen, A. Hadid, and M. Pietikainen. Face description with local binary patterns: Application to face recognition. *IEEE Transactions on Pattern Analysis and Machine Intelligence*, 28(12):2037 –2041, December 2006.

[5] S. Aksoy and R.M. Haralick. Textural features for image database retrieval. In *IEEE Workshop on Content-Based Access of Image and Video Libraries, 1998. Proceedings.*, pages 45 –49, June 1998.

[6] P. Amman and R. Razzoli. Bone strength and its determinants. *Osteoporos Int*, 14(Suppl 3):S13–S18, 2003.

[7] L. Apostol, V. Boudousq, O. Basset, C. Odet, and S. Yot. Relevance of 2D radiographic texture analysis for the assessment of 3D bone micro architecture. *Medical Physics*, 33(9):3546–3556, 2006.

[8] J. Bacchetta, Stephanie Boutroy, E. Lespessailles, P. D. Delmas, and Anne Fouque-Aubert. Assessment of bone micro architecture in chronic kidney assessment of bone micro architecture in chronic kidney disease: A comparison of 2D bone texture analysis and high-resolution peripheral quantitative computed tomography at the radius and tibia disease: A comparison of 2D bone texture analysis and high-resolution peripheral quantitative computed tomography at the radius and tibia. *Calcified Tissue International*, 87:385–391, 2010.

[9] A. Barbier, C. Martel, M. Nys, and G Mocaer. The visualization and evaluation of bone architecture in the rat using three-dimensional x-ray microcomputed tomography. *Journal of Bone and Mineral Research*, 17:37–44, 1999.

[10] N. Boutry, B. Cortet, D. Chapard, and P. Dubois. Bone structure of the calcaneus: analysis with magnetic resonance imaging and correlation with histomorphometric study. *Osteoporos Int*, 15:827–833, 2004.

[11] J.G. Brankov, M.N. Wernick, D. Chapman, Z. Zhong, C. Muehleman, J Li, and M.A. Anastasio. Multiple-image computed tomography. In *IEEE International Symposium on Biomedical Imaging: Nano to Macro*, pages 948 – 951 Vol. 1, April 2004.

[12] H.M. Britz, J. Jokihara, and O.V. Cooper, D.M.L. Leppanen. 3D visualization and quantification of rat cortical bone porosity using a desktop micro-CT system: a case study in the tibia. *Journal of Microscopy*, Vol 240 Issue 1:32–37, 2010.

[13] A. Buades, B. Coll, and J. Morel. A non-local algorithm for image denoising. In *IEEE Computer Society Conference on Computer Vision and Pattern Recognition, 2005.*, volume 2, pages 60 – 65 vol. 2, June 2005.

[14] P. Caligiuri, ML. Giger, MJ. Favus, and H. Jia. Computerized radiographic analysis of osteoporosis: preliminary evaluation. *Radiology*, 186:471–474, 1993.

[15] L. Carlucci. A formal system for texture languages. *Pattern Recognition*, 4(1):53–72, 1972.

[16] G. Castellano, L. Bonilha, L.M. Li, and F. Cendes. Texture analysis of medical images. *Clinical Radiology*, 59(12):1061 – 1069, 2004.

[17] N. P. Castellanos, E. Martinez, and J. Gutierrez. Improving osteoporosis diagnosis in children using image texture analysis. *Conference of the IEEE engineering in medicine and biology society*, 2011:6184–6197, 2011.

[18] D. Chapman, W. Thomlinson, R.E. Johnston, D. Washburn, E. Pisano, N. Gmur, R. Menk, F. Arfelli, D. Sayers, and Z. Zhong. Diffraction enhaced x-ray imaging. *Physics in Medicine and Biology*, Vol. 42(Number 11), April 1997.

[19] C. Chappard, Valerie Bousson, D. Mitton, C. Bergot, and T. Moser. Prediction of femoral fracture load: Cross sectional study of texture analysis and geometric measurements on plain radiographs versus bone mineral density. *Radilogical Soceity of North America*, 255(2):536–542, 2010.

[20] D. Chappard, P. Guggenbuhl, and E. Legrand. Texture analysis of x-ray radiographs is correlated with bone histomorphometry. *Journal of Bone Mineral Metabolism*, 23(9):24–29, June 2005.

[21] D. Chappard, E. Legrand, B. Haettich, G. Chales, B. Auvinet, J. P. Eschard, J. P. Hamelin, M. F. Basle, and M. Audran. Fractal dimension of trabecular bone: comparison of three histomorphometric computed techniques for measuring the architectural two-dimensional complexity. *Journal of Pathology*, 195(4):515–21, Nov 2001.

[22] J Compston. Monitoring osteoporosis treatment. *Journal of Bone Mineral Metabolism*, 23(6):781–788, 2009.

[23] D.M.L. Cooper, B. Bewer, S. Wiebe, and D. Chapman. Abbreviated title: Diffraction enhances imaging of trabecular bone architecture. *Canadian Association of Radiologists Journal*.

[24] D.M.L. Cooper, B. Bewer, S. Wiebe, and D. Chapman. Diffraction enhanced x-ray imaging of the distal radius: A novel approach for visualization of trabecular bone architecture. *Canadian Association of Radiologists Journal*, 62:251–255, 2011.

[25] T. Le Corroller, J. Halgrin, M. Pithioux, D. Guenoun, and P. Chabrand. Combination of texture and bone mineral density improves the prediction of fracture load in human femurs. *Osteoporosis International*, 23:163–169, 2012.

[26] B. Cortet, D. Chapard, N. Boutry, and P. Dubois. Relationship between computed tomographic image analysis and histomorphometry for micro architectural characterization of human calcaneus. *Calcified Tissue International*, 75:23–31, 2004.

[27] A.F. Costa, G. Humpire-Mamani, and A.J.M. Traina. An efficient algorithm for fractal analysis of textures. In *25th SIBGRAPI Conference on Graphics, Patterns and Images (SIBGRAPI), 2012*, pages 39 –46, August 2012.

[28] P. Coupe, P. Yger, S. Prima, and P. Hellier. An optimized blockwise nonlocal means denoising filter for 3D magnetic resonance images. *IEEE Transactions on Medical Imaging*, Vol. 27(No. 4), April 2008.

[29] G. Diederichs, T. Link, K. Marie, M. Huber, and P. Rogalla. Feasibility of measuring trabecular bone structure of the proximal femur using 64-slice multidetector feasibility of measuring trabecular bone structure of the proximal femur using 64-slice multidetector computed tomography in a clinical setting. *Calcified Tissue International*, vol. 83:332–341, October 2008.

[30] A.A. Efros and T.K. Leung. Texture synthesis by non-parametric sampling. In *The Proceedings of the Seventh IEEE International Conference on Computer Vision*, volume 2, pages 1033 –1038 vol.2, 1999.

[31] N. L. Fazzalari and I. H. Parkinson. Fractal dimension and architecture of trabecular bone. In *The Journal of Pathology*, volume 178, Issue 1, pages 1005–105, 1996.

[32] Anne Fouque-Aubert, Stephanie Boutroy, and Hubert Marotte. Assessment of hand trabecular bone texture with high resolution direct digital radiograph in rheumatoid arthritis: A case control study. *Joint Bone Spine*, 79:379–383, 2012.

[33] P. Guggenbuhl, F. Bodic, L. Hamel, and D. Chappard. Texture analysis of x-ray radiographs of iliac bone is correlated with bone micro-CT. *Osteoporosis International*, 17(8):447–454, January 2006.

[34] Zhenhua Guo, Lei Zhang, and D. Zhang. A completed modeling of local binary pattern operator for texture classification. *IEEE Transactions on Image Processing*, 19(6):1657 –1663, June 2010.

[35] D. Hans, S. Boutroy, L. Pothuaud, and R. Winzenrieth. Correlations between trabecular bone score, measured using anteroposterior dual-energy x-ray absorptiometry acquisition, and 3-dimensional parameters of bone micro architecture: An experimental study on human cadaver vertebrae. *Journal of Clinical Densitometry*, 14(3):302–312, 2011.

[36] R. M. Haralick, K. Shanmugam, and I. Dinstein. Textural features for image classification. *IEEE Transactions on Systems, Man and Cybernetics*, SMC-3(6):610 – 621, November 1973.

[37] R.M. Haralick. Statistical and structural approaches to texture. *IEEE Computational Systems Bioinformatics Conference, 2005. Workshops and Poster Abstracts.*, 67(5):786 – 804, May 1979.

[38] L. D. Hordon, M. Raisi, J. E. Aaron, S. K. Paxton, M. Beneton, and J. A. Kanis. Trabecular architecture in women and men of similar bone mass with and without vertebral fracture: I. two-dimensional histology. *Elsevier*, 27(2):271–276, 2000.

[39] M. Horng, Y Sun, and X. Lin. Texture feature coding method for classification of liver sonography. *Computerized Medical Imaging and Graphics*, 26(1):33 – 42, 2002.

[40] http://www.skyscan.be. SkyScan CTAN software.

[41] M. B. Huber, M. Haenni, C. Hengg, S Majumder, and T. M. Link. Development and testing of texture discriminators for the analysis of trabecular bone in proximal femur radiographs. *American Association of Physicists in Medicine*, 36(11):5089–5098, 2009.

[42] D. Iakovidis, E. Keramidas, and D. Maroulis. Fuzzy local binary patterns for ultrasound texture characterization. In Aurélio Campilho and Mohamed Kamel, editors, *Image Analysis and Recognition*, volume 5112 of *Lecture Notes in Computer Science*, pages 750–759. Springer Berlin Heidelberg, 2008.

[43] A. Johnson and M. Hebert. Object recognition by matching oriented points. *Proceedings of the Conference on Computer Vision and Pattern Recognition, USA*, pages 684–689, 1997.

[44] V. B. Kraus, S. Feng, S. Wang, S. White, M. Ainslie, A. Brett, A. Holmes, and H. Charles. Trabecular morphometry by fractal signature analysis is a novel marker of osteoarthritis progression. *Arthritis Rheum*, 60(12):3711–22, December 2009.

[45] K. I. Laws. Rapid texture identification. *Procedure of SPIE 0238*, 238(376):376–381, 1980.

[46] T. Le Corroller, M. Pithioux, F. Chaari, B. Rosa, S. Parratte, B. Maurel, J. Argenson, P. Champsaur, and P. Chabrand. Bone texture analysis is correlated with three-dimensional micro architecture and mechanical properties of trabecular bone in osteoporotic femurs. *Journal of Bone Mineral Metabolism*, 31(1):82–88, January 2013.

[47] E. Lespessailles, C. Gadois, I. Kousignian, J. P. Neveu, P. Fardellone, S. Kolta, C. Roux, J. P. Do-Huu, and C. L. Benhamou. Clinical interest of bone texture analysis in osteoporosis: a case control multicenter study. *Osteoporos Int*, 19(7):1019–28, July 2008.

[48] E. Lespessailles, C. Gadois, G. Lemineur, and L. Benhamou. Bone texture analysis on direct radiographic images: Precision study and relationship with bone mineral density at the os calcis. *Calcified Tissue International*, 80:97–102, 2007.

[49] E. Lespessailles, J. P. Roux, C. L. Benhamou, M. E. Arlot, E. Eynard, R. Harba, C. Padonou, and P. J. Meunier. Fractal analysis of bone texture on os calcis radiographs compared with trabecular micro architecture analyzed by histomorphometry. *Calcified Tissue International*, 63:121–125, 1998.

[50] J. Liang, X. Zhao, R. Xu, C. Kwan, and C.-I. Chang. Target detection with texture feature coding method and support vector machines. In *IEEE International Conference on Acoustics, Speech, and Signal Processing, 2004. Proceedings. (ICASSP '04).*, volume 2, pages 713–716 vol.2, May 2004.

[51] J. C. Lin, S. Grampp, T. Link, and S. Majumder. Fractal analysis of proximal femur radiographs: Correlation with biomechanical properties and bone mineral density. *Osteoporosis International*, 9:516–524, 1999.

[52] T. M. Link, S. Majumdar, S. Grampp, G. Guglielmi, C. van Kuijk, H. Imhof, C. Glueer, and J. E. Adams. Imaging of trabecular bone structure in osteoporosis. *European Radiology*, 9:1781–1788, 1999.

[53] D. Lowe. Distinctive image features from scale-invariant keypoints. *International Journal of Computer Vision*, 60:91–110, 2004.

[54] Ito M. Parathyroid hormone and bone quality. *Clinical Calcium*, 15(12):31–37, 2005.

[55] S. Majumdar, H. K. Genant, S. Grampp, and D. C. Newitt. Correlation of trabecular bone structure with age, bone mineral density, and osteoporotic status: In vivo studies in the distal radius using high resolution magnetic resonance imaging. *Journal of Bone and Mineral Research*, 12(1):111–118, 1997.

[56] F. Mallard, B. Bouvard, P. Mercier, P. Bizot, P. Cronier, and D. Chappard. Trabecular micro architecture in established osteoporosis: Relationship between vertebrae, distal radius and calcaneus by x-ray imaging texture analysis. *Orthopedic Trauma Surgery*, 99(1):52–59, February 2013.

[57] A. Materka, P. Cichy, and J. Tuliszkiewicz. Texture analysis of x-ray images for detection of changes in bone mass and structure. In *IEEE transaction in Medical Imaging*, 1999.

[58] M .R. McClung, M. A. Bolognese, M. D. Miller, C. Zhang, and M. C. Peterson. Denosumab in postmenopausal women with low bone mineral density. *New England Journal of Medicine*, (354):821–831, February 2006.

[59] J. Mollenhauer, M.E. Aurich, Z. Zhong, C. Muehleman, A.A. Cole, M. Hasnah, O. Oltulu, K.E. Kuettner, A. Margulis, and L.D. Chapman. Diffraction-enhanced x-ray imaging of articular cartilage. *Osteoarthritis and Cartilage*, 10(3):163 – 171, 2002.

[60] D. Mueller, T. M. Link, R. Monetti, J. Bauer, and E. J. Rummeny. The 3D-based scaling index algorithm: a new structure measure to analyze trabecular bone architecture in high-resolution MR images in vivo. *Osteoporosis International*, 17:1483–1493, 2006.

[61] L. P. Nogueira, D. Braz, R. C. Barroso, and L. F. Oliviera. 3D histomorphometric quantification of trabecular bones by computed microtomography using synchrotron radiation. *Micron*, 41:990–996, 2010.

[62] Johnell O, Kanis JA, Oden A, Johansson H, and Delmas P. Predictive value of BMD for hip and other fractures. *Journal of Bone and Mineral Research*, 20(7):1185–1194, July 2005.

[63] T. Ojala, M. Pietikainen, and T. Maenpaa. A generalized local binary pattern operator for multiresolution gray scale and rotation invariant texture classification. In Sameer Singh, Nabeel Murshed, and Walter Kropatsch, editors, *Advances in Pattern Recognition — ICAPR 2001*, volume 2013 of *Lecture Notes in Computer Science*, pages 399–408. Springer Berlin Heidelberg, 2001.

[64] T. Ojala, M. Pietikainen, and T. Maenpaa. Multiresolution gray-scale and rotation invariant texture classification with local binary patterns. *IEEE Transactions on Pattern Analysis and Machine Intelligence*, 24(7):971–987, July 2002.

[65] X Ouyang, S. Majumder, T. Link, and J. Lin. Morphometric texture analysis of spinal trabecular bone structure assessed using orthogonal radiographic projections. *Medical Physics*, 25(10):2037–2045, 1998.

[66] L. Pothuaud, C. L. Benhamou, P. Porion, E. Lespessailles, R. Harba, and P. Levitz. Fractal dimension of trabecular bone projection texture is related to three-dimensional micro architecture. *Journal of Bone and Mineral Research*, 15(4):691–9, April 2000.

[67] Pasi Pulkkinen, Simo Saarakkala, Miika T. Nieminen, and Timo Jamsa. Standard radiography: Untapped potential in the assessment of osteoporosis fracture risk. *Europian Radiology*, 23:1375–1382, 2013.

[68] P. Ranjanomennahary, S. S. Ghalia, D. Malouche, and C. Chappard. Comparison of radiograph-based texture analysis and bone mineral density comparison of radiograph-based texture analysis and bone mineral density with three-dimensional micro architecture of trabecular bone. *American Association of Physicists in Medicine*, 38(1):420 – 428, January 2011.

[69] JC. Rice, SC. Cowin, and JA. Bowman. On the dependence of the elasticity and strength of cancellous bone on apparent density. *Journal of Biomechanics*, 21(2):155–168, 1988.

[70] A. E. Rodríguez-Soto, K. D. Fritscher, B. Schuler, A. S. Issever, T. Roth, F. Kamelger, C. Kammerlander, M. Blauth, R. Schubert, and T. M. Link. Texture analysis, bone mineral density, and cortical thickness of the proximal femur: fracture risk prediction. *Journal of Computer Assisted Tomography*, 34(6):949–57, 2010.

[71] J. P. Roux, J. Wegrzyn, S. Boutroy, and D. Hans. The predictive value of trabecular bone score (TBS) on whole lumbar vertebrae mechanics: an ex vivo study. *Osteoporosis International*, 23(4):178–189, 2012.

[72] P. Scovanner, S. Ali, and M. Shah. A 3-dimensional SIFT descriptor and its application to action recognition. *Proceeding of the 15th International Conference on Multimedia, ACM*, pages 357–360, 2007.

[73] E. Seeman, P. Chavassieux, and P. D. Delmas. Insights into material and structural basis of bone fragility from diseases associated with fractures: How determinants of the biomechanical properties of bone are compromised by disease. *Endocrine Reviews*, 28(2):151–164, 2007.

[74] I. Sidorenko, R. Monetti, J. Bauer, D. Mueller, and E. Rummeny. Assessing methods for charecterizing local and global structural and biomechanical properties of the trabecular bone network. *Current Medicinal Chemistry*, 18:3401–3409, 2011.

[75] BC. Silva, S. Boutroy, C. Zhang, and D. Hans. Trabecular bone score (TBS)–a novel method to evaluate bone micro architectural texture in patients with primary hyperparathyroidism. *Journal of Clinical Endocrinology*, 98(5):1963–1970, 2013.

[76] D. Steines, S. W. Liew, C. Arnaud, P. Lang, and P. Hess. Radiographic trabecular 2D and 3D parameters of proximal femoral bone cores correlate with each other and with yield stress. *Osteoporosis International*, 20:1929–1938, 2009.

[77] F. Tomita and S. Tsuji. Computer analysis of visual textures. *Kluwer Academic Publishers*, 1990.

[78] M.N. Wernick, O. Wirjadi, D. Chapman, O. Oltulu, Zhong Zhong, and Yongyi Yang. Preliminary investigation of a multiple-image radiography method. In *IEEE International Symposium on Biomedical Imaging, 2002. Proceedings. 2002*, pages 129 – 132, 2002.

[79] R. Winzenrieth, F. Michelet, and Hans. Three-dimensional (3D) micro architecture correlations with 2D projection image gray-level variations assessed by trabecular bone score using high-resolution computed tomographic acquisitions: Effects of resolution and noise. *Journal of Clinical Densitometry*, 34(2):434–443, 2012.

[80] Y. H. Zhang, L. Shen, and Y. Shen. Postmenopausal women with osteoporosis and osteoarthritis show different microstructural characteristics of trabecular bone in proximal tibia using high-resolution magnetic resonance imaging at 3 tesla. *BMC Musculoskeletal Disorders*, 14(1):136–143, 2013.

Appendix A

Data Tables of GLCM

Data tables of GLCM features for all sets of images are placed here.

Table A.1: Data table of GLCM features for horizontal images of high angle side on the RC. ROIs: distal (d), medial (m), and proximal (p).

samples	orientation	ROI		Correlation	Contrast	Homogeneity	Energy
15	Horizontal	p	μ	2.6e-05	0.4245	24.8181	31.68890
			σ	1.82e-05	0.0935	4.3982	13.3393
		m	μ	3.6456e-005	0.4058	26.0761	35.8217
			σ	2.4509e-005	0.0965	4.6634	14.6935
		d	μ	2.5952e-005	0.4302	25.0795	33.6286
			σ	3.0348e-005	0.1259	5.6943	16.2855

Table A.2: Data table of GLCM features for horizontal DEI images. ROIs: distal (d), medial (m), and proximal (p).

samples	orientation	ROI		Correlation	Contrast	Homogeneity	Energy
15	Horizontal	p	μ	2.6e-05	0.4045	23.56	30.79
			σ	1.81e-05	0.0935	4.3982	13.3393
		m	μ	3.5456e-005	0.4058	26.0761	35.8217
			σ	2.4509e-005	0.0965	4.6534	14.6935
		d	μ	2.5752e-005	0.4302	25.1795	32.5686
			σ	3.0048e-005	0.1459	5.5943	16.1855

Table A.3: Data table of GLCM features for vertical images of high angle side on the RC. ROIs: distal (d), medial (m), and proximal (p).

samples	orientation	ROI		Correlation	Contrast	Homogeneity	Energy
15	Horizontal	p	μ	2.5e-05	0.4132	23.78	30.23
			σ	1.82e-05	0.0935	4.3982	13.3393
		m	μ	3.6456e-005	0.4058	26.0761	35.8217
			σ	2.4509e-005	0.0965	4.6634	14.6935
		d	μ	2.5952e-005	0.4302	25.0795	33.6286
			σ	3.0348e-005	0.1259	5.6943	16.2855

Table A.4: Data table of GLCM features for vertical DEI images. ROIs: distal (d), medial (m), and proximal (p).

samples	orientation	ROI		Correlation	Contrast	Homogeneity	Energy
15	Horizontal	p	μ	2.6e-05	0.4045	23.56	30.79
			σ	1.81e-05	0.0935	4.3982	13.3393
		m	μ	3.5456e-005	0.4058	26.0761	35.8217
			σ	2.4509e-005	0.0965	4.6534	14.6935
		d	μ	2.5752e-005	0.4302	25.1795	32.5686
			σ	3.0048e-005	0.1459	5.5943	16.1855

Appendix B

Data Tables of TFCM

Data tables of TFCM features for all sets of images are placed here.

Table B.1: Data table of TFCM features for horizontal images of high angle side on the RC. ROIs: distal (d), medial (m), and proximal (p).

samples	orientation	ROI		Coarseness	Homogeniety	Convergence	Variance
15	Horizontal	p	μ	2.6e-05	0.4245	24.8181	31.68890
			σ	1.82e-05	0.0935	4.3982	13.3393
		m	μ	3.6456e-005	0.4058	26.0761	35.8217
			σ	2.4509e-005	0.0965	4.6634	14.6935
		d	μ	2.5952e-005	0.4302	25.0795	33.6286
			σ	3.0348e-005	0.1259	5.6943	16.2855

Table B.2: Data table of TFCM features for horizontal DEI images. ROIs: distal (d), medial (m), and proximal (p).

samples	orientation	ROI		Coarseness	Homogeniety	Convergence	Variance
15	Horizontal	p	μ	2.6e-05	0.4045	23.56	30.79
			σ	1.81e-05	0.0935	4.3982	13.3393
		m	μ	3.5456e-005	0.4058	26.0761	35.8217
			σ	2.4509e-005	0.0965	4.6534	14.6935
		d	μ	2.5752e-005	0.4302	25.1795	32.5686
			σ	3.0048e-005	0.1459	5.5943	16.1855

Table B.3: Data table of TFCM features for vertical images of high angle side on the RC. ROIs: distal (d), medial (m), and proximal (p).

samples	orientation	ROI		Coarseness	Homogeniety	Convergence	Variance
15	Horizontal	p	μ	2.5e-05	0.4132	23.78	30.23
			σ	1.82e-05	0.0935	4.3982	13.3393
		m	μ	3.6456e-005	0.4058	26.0761	35.8217
			σ	2.4509e-005	0.0965	4.6634	14.6935
		d	μ	2.5952e-005	0.4302	25.0795	33.6286
			σ	3.0348e-005	0.1259	5.6943	16.2855

Table B.4: Data table of TFCM features for vertical DEI images. ROIs: distal (d), medial (m), and proximal (p).

samples	orientation	ROI		Coarseness	Homogeniety	Convergence	Variance
15	Horizontal	p	μ	2.6e-05	0.4045	23.56	30.79
			σ	1.81e-05	0.0935	4.3982	13.3393
		m	μ	3.5456e-005	0.4058	26.0761	35.8217
			σ	2.4509e-005	0.0965	4.6534	14.6935
		d	μ	2.5752e-005	0.4302	25.1795	32.5686
			σ	3.0048e-005	0.1459	5.5943	16.1855

Appendix C

Data table of LBP

Data tables of LBP for high angle and DEI images at 0.5 on the rocking curve are placed here.

Table C.1: Data table of LBP operators for horizontal images of high angle side on the RC. ROIs: distal (d), medial (m), and proximal (p).

samples	orientation	ROI		LBP 11	LBP 12
15	Horizontal	p	μ	4235	3977
			σ	293	180
		m	μ	4462	3771
			σ	305	231
		d	μ	4770	3700
			σ	120	290

Table C.2: Data table of LBP operators for horizontal DEI images. ROIs: distal (d), medial (m), and proximal (p).

samples	orientation	ROI		LBP 11	LBP 12
15	Horizontal	p	μ	4230	3965
			σ	224	157
		m	μ	4323	3961
			σ	325	220
		d	μ	4501	3288
			σ	160	201

Table C.3: Data table of LBP operators for vertical images of high angle side on the RC. ROIs: distal (d), medial (m), and proximal (p).

samples	orientation	ROI		LBP 11	LBP 12
15	Horizontal	p	μ	4310	3986
			σ	283	161
		m	μ	4378	3861
			σ	325	220
		d	μ	4508	3480
			σ	129	224

Table C.4: Data table of LBP operators for vertical DEI images. ROIs: distal (d), medial (m), and proximal (p).

samples	orientation	ROI		LBP 11	LBP 12
15	Horizontal	p	μ	4235	3977
			σ	293	180
		m	μ	4462	3771
			σ	305	231
		d	μ	4770	3700
			σ	120	290

Appendix D

Data table of fractal analysis

Data tables of fractal analysis for high angle and DEI images at 0.5 on the rocking curve are placed here.

Table D.1: Data table of Fractal analysis features for horizontal images of high angle side on the RC. ROIs: distal (d), medial (m), and proximal (p).

samples	orientation	ROI		Fractal Dimension	Lacunarity
15	Horizontal	p	μ	2.60	0.05
			σ	0.20	0.01
		m	μ	2.64	0.07
			σ	0.20	0.02
		d	μ	2.68	0.09
			σ	0.15	0.01

Table D.2: Data table of Fractal analysis features for horizontal DEI images. ROIs: distal (d), medial (m), and proximal (p).

samples	orientation	ROI		Fractal Dimension	Lacunarity
15	Horizontal	p	μ	2.61	0.06
			σ	0.10	0.01
		m	μ	2.65	0.08
			σ	0.20	0.01
		d	μ	2.69	0.09
			σ	0.15	0.01

Table D.3: Data table of Fractal analysis features for vertical images of high angle side on the RC. ROIs: distal (d), medial (m), and proximal (p).

samples	orientation	ROI		Fractal Dimension	Lacunarity
15	Horizontal	p	μ	2.64	0.04
			σ	0.20	0.01
		m	μ	2.66	0.06
			σ	0.20	0.02
		d	μ	2.70	0.08
			σ	0.20	0.01

Table D.4: Data table of Fractal analysis features for vertical DEI images. ROIs: distal (d), medial (m), and proximal (p).

samples	orientation	ROI		Fractal Dimension	Lacunarity
15	Horizontal	p	μ	2.61	0.06
			σ	0.10	0.01
		m	μ	2.65	0.08
			σ	0.20	0.01
		d	μ	2.69	0.09
			σ	0.15	0.01

Appendix E

Correlation Tables

Correlation tables of GLCM features for all sets of images are placed here.

Table E.1: Correlation between GLCM and architectural parameters for horizontal images of high angle at 0.25 on the rocking curve.

	r^2	Best Fit Model	Best Feature	p
Bone Volume (BV)	0.26	Linear	Contrast	< 0.01
Percent Bone Volume (BV/TV)	0.34	Linear	Energy	< 0.01
Bone Surface by Volume Ratio (BS/BV)	0.33	Linear	Energy	< 0.01
Bone Surface (BS)	0.24	Linear	Energy	< 0.01
Trabecular Number (Tb.N)	0.35	Linear	Energy	< 0.01

Table E.2: Correlation between GLCM and architectural parameters for vertical images of high angle at 0.25 on the rocking curve.

	r^2	Best Fit Model	Best Feature	p
Bone Volume (BV)	0.27	Linear	Contrast	< 0.01
Percent Bone Volume (BV/TV)	0.35	Linear	Energy	< 0.01
Bone Surface by Volume Ratio (BS/BV)	0.34	Linear	Energy	< 0.01
Bone Surface (BS)	0.24	Linear	Energy	< 0.01
Trabecular Number (Tb.N)	0.35	Linear	Energy	< 0.01

Table E.3: Correlation between GLCM and architectural parameters for horizontal DEI images at 0.25 on the rocking curve.

	r^2	Best Fit Model	Best Feature	p
Bone Volume (BV)	0.30	Linear	Contrast	< 0.01
Percent Bone Volume (BV/TV)	0.34	Linear	Energy	< 0.01
Bone Surface by Volume Ratio (BS/BV)	0.36	Linear	Energy	< 0.01
Bone Surface (BS)	0.26	Linear	Energy	< 0.01
Trabecular Number (Tb.N)	0.35	Linear	Energy	< 0.01

Table E.4: Correlation between GLCM and architectural parameters for vertical DEI images at 0.25 on the rocking curve.

	r^2	Best Fit Model	Best Feature	p
Bone Volume (BV)	0.27	Linear	Contrast	< 0.01
Percent Bone Volume (BV/TV)	0.36	Linear	Energy	< 0.01
Bone Surface by Volume Ratio (BS/BV)	0.36	Linear	Energy	< 0.01
Bone Surface (BS)	0.28	Linear	Energy	< 0.01
Trabecular Number (Tb.N)	0.34	Linear	Energy	< 0.01

Table E.5: Correlation between TFCM and architectural parameters for horizontal images of high angle at 0.125 on the rocking curve.

	r^2	Best Fit Model	Best Feature	p
Bone Volume (BV)	0.23	Linear	Homogeneity	< 0.01
Percent Bone Volume (BV/TV)	0.22	Linear	Mean convergence	< 0.01
Bone Surface (BS)	0.32	Linear	Homogeneity	< 0.01
Trabecular Number (Tb.N)	0.24	Linear	Homogeneity	< 0.01

Table E.6: Correlation between TFCM and architectural parameters for vertical images of high angle at 0.125 on the rocking curve.

	r^2	Best Fit Model	Best Feature	p
Bone Volume (BV)	0.24	Linear	Homogeneity	< 0.01
Percent Bone Volume (BV/TV)	0.22	Linear	Mean convergence	< 0.01
Bone Surface (BS)	0.35	Linear	Homogeneity	< 0.01
Trabecular Number (Tb.N)	0.25	Linear	Homogeneity	< 0.01

Table E.7: Correlation between TFCM and architectural parameters for horizontal DEI images at 0.125 on the rocking curve.

	r^2	Best Fit Model	Best Feature	p
Bone Volume (BV)	0.25	Linear	Homogeneity	< 0.01
Percent Bone Volume (BV/TV)	0.22	Linear	Mean convergence	< 0.01
Bone Surface (BS)	0.34	Linear	Homogeneity	< 0.01
Trabecular Number (Tb.N)	0.24	Linear	Homogeneity	< 0.01

Table E.8: Correlation between TFCM and architectural parameters for vertical DEI images at 0.125 on the rocking curve.

	r^2	Best Fit Model	Best Feature	p
Bone Volume (BV)	0.22	Linear	Homogeneity	< 0.01
Percent Bone Volume (BV/TV)	0.23	Linear	Mean convergence	< 0.01
Bone Surface (BS)	0.39	Linear	Homogeneity	< 0.01
Trabecular Number (Tb.N)	0.23	Linear	Homogeneity	< 0.01

Table E.9: Correlation between LBP and architectural parameters for horizontal images of high angle at 0.25 on the rocking curve.

	r^2	Best Fit Model	Best Feature	p
Bone Volume (BV)	0.20	Linear	LBP 11	< 0.01
Percent Bone Volume (BV/TV)	0.22	Linear	LBP 12	< 0.01
Bone Surface (BS)	0.25	Linear	LBP 11	< 0.01
Bone Surface Density (BS/TV)	0.22	Linear	LBP 11	< 0.01
Trabecular Number (Tb.N)	0.20	Linear	LBP 12	< 0.01

Table E.10: Correlation between LBP and architectural parameters for vertical images of high angle at 0.25 on the rocking curve.

	r^2	Best Fit Model	Best Feature	p
Bone Volume (BV)	0.21	Linear	LBP 11	< 0.01
Percent Bone Volume (BV/TV)	0.24	Linear	LBP 12	< 0.01
Bone Surface (BS)	0.31	Linear	LBP 11	< 0.01
Bone Surface Density (BS/TV)	0.25	Linear	LBP 11	< 0.01
Trabecular Number (Tb.N)	0.21	Linear	LBP 12	< 0.01

Table E.11: Correlation between LBP and architectural parameters for horizontal DEI images at 0.25 on the rocking curve.

	r^2	Best Fit Model	Best Feature	p
Bone Volume (BV)	0.21	Linear	LBP 11	< 0.01
Percent Bone Volume (BV/TV)	0.23	Linear	LBP 12	< 0.01
Bone Surface (BS)	0.30	Linear	LBP 11	< 0.01
Bone Surface Density (BS/TV)	0.25	Linear	LBP 11	< 0.01
Trabecular Number (Tb.N)	0.23	Linear	LBP 12	< 0.01

Table E.12: Correlation between LBP and architectural parameters for vertical DEI images at 0.25 on the rocking curve.

	r^2	Best Fit Model	Best Feature	p
Bone Volume (BV)	0.22	Linear	LBP 11	< 0.01
Percent Bone Volume (BV/TV)	0.24	Linear	LBP 12	< 0.01
Bone Surface (BS)	0.32	Linear	LBP 11	< 0.01
Bone Surface Density (BS/TV)	0.29	Linear	LBP 11	< 0.01
Trabecular Number (Tb.N)	0.24	Linear	LBP 12	< 0.01

Table E.13: Correlation between FD and architectural parameters for horizontal images of high angle at 0.125 on the rocking curve.

	r^2	Best Fit Model	Best Feature	p
Bone Volume (BV)	0.20	Linear	Kormogorov FD	< 0.01
Percent Bone Volume (BV/TV)	0.20	Linear	Kormogorov FD	< 0.01
Bone Surface (BS)	0.34	Linear	Kormogorov FD	< 0.01
Bone Surface by Volume Ratio (BS/BV)	0.24	Linear	Lacunarity	< 0.01
Trabecular Number (Tb.N)	0.25	Linear	Kormogorov FD	< 0.01

Table E.14: Correlation between FD and architectural parameters for vertical images of high angle at 0.125 on the rocking curve.

	r^2	Best Fit Model	Best Feature	p
Bone Volume (BV)	0.27	Linear	Kormogorov FD	< 0.01
Percent Bone Volume (BV/TV)	0.23	Linear	Kormogorov FD	< 0.01
Bone Surface (BS)	0.40	Linear	Kormogorov FD	< 0.01
Bone Surface by Volume Ratio (BS/BV)	0.24	Linear	Lacunarity	< 0.01
Trabecular Number (Tb.N)	0.27	Linear	Kormogorov FD	< 0.01

Table E.15: Correlation between FD and architectural parameters for horizontal DEI images at 0.125 on the rocking curve.

	r^2	Best Fit Model	Best Feature	p
Bone Volume (BV)	0.28	Linear	Kormogorov FD	< 0.01
Percent Bone Volume (BV/TV)	0.24	Linear	Kormogorov FD	< 0.01
Bone Surface (BS)	0.42	Linear	Kormogorov FD	< 0.01
Bone Surface by Volume Ratio (BS/BV)	0.25	Linear	Lacunarity	< 0.01
Trabecular Number (Tb.N)	0.26	Linear	Kormogorov FD	< 0.01

Table E.16: Correlation between FD and architectural parameters for vertical DEI images at 0.125 on the rocking curve.

	r^2	Best Fit Model	Best Feature	p
Bone Volume (BV)	0.30	Linear	Kormogorov FD	< 0.01
Percent Bone Volume (BV/TV)	0.24	Linear	Kormogorov FD	< 0.01
Bone Surface (BS)	0.44	Linear	Kormogorov FD	< 0.01
Bone Surface by Volume Ratio (BS/BV)	0.25	Linear	Lacunarity	< 0.01
Trabecular Number (Tb.N)	0.26	Linear	Kormogorov FD	< 0.01